SOME STUDIES ON CORE-COLLAPSE SUPERNOVAE AND NEUTRON STARS

By

PRASANTA CHAR

PHYS05201104001

Saha Institute of Nuclear Physics, Kolkata

A thesis submitted to the

Board of Studies in Physical Sciences

In partial fulfillment of requirements

For the Degree of

DOCTOR OF PHILOSOPHY

of

HOMI BHABHA NATIONAL INSTITUTE

August, 2016

Homi Bhabha National Institute

Recommendations of the Viva Voce Committee

As members of the Viva Voce Committee, we certify that we have read the dissertation prepared by **Prasanta Char** entitled **"Some Studies on Core-Collapse Supernovae and Neutron Stars"** and recommend that it maybe accepted as fulfilling the thesis requirement for the award of Degree of Doctor of Philosophy.

P. Mitra Date: 16.12.16

Chairman - Professor Parthasarathi Mitra

Debades Bandyopadhyay Date: 16.12.2016

Guide / Convener - Professor Debades Bandyopadhyay

Date:

Co-guide - (if any)

SB Date: 16-12-2016

Examiner - Professor Sudip Bhattacharyya

Debasish Majumdar Date: 16/12/2016

Member 1 - Professor Debasish Majumdar

Date: 16-12-16

Member 2 - Professor Ambar Ghosal Ambar Ghosal

Final approval and acceptance of this thesis is contingent upon the candidate's submission of the final copies of the thesis to HBNI.

I/We hereby certify that I/we have read this thesis prepared under my/our direction and recommend that it may be accepted as fulfilling the thesis requirement.

Date: 16.12.2016

Place: KOLKATA

Guide: Debades Bandyopadhyay

STATEMENT BY AUTHOR

This dissertation has been submitted in partial fulfillment of requirements for an advanced degree at Homi Bhabha National Institute (HBNI) and is deposited in the Library to be made available to borrowers under rules of the HBNI.

Brief quotations from this dissertation are allowable without special permission, provided that accurate acknowledgement of source is made. Requests for permission for extended quotation from or reproduction of this manuscript in whole or in part may be granted by the Competent Authority of HBNI when in his or her judgment the proposed use of the material is in the interests of scholarship. In all other instances, however, permission must be obtained from the author.

Prasanta Char

DECLARATION

I, hereby declare that the investigation presented in the thesis has been carried out by me. The work is original and has not been submitted earlier as a whole or in part for a degree / diploma at this or any other Institution / University.

Prasanta Char

LIST OF PUBLICATIONS ARISING FROM THE THESIS

Journal:

1. Massive Neutron Stars with Antikaon Condensates in a Density Dependent Hadron Field Theory.

   Prasanta Char, Sarmistha Banik;

   Physical Review C, **2014**, *90*, *015801* [arXiv:1406.4961]

2. A Comparative Study of Hyperon Equations of State in Supernova Simulations.

   Prasanta Char, Sarmistha Banik, Debades Bandyopadhyay;

   Astrophysical Journal, **2015**, *809*, *116* [arXiv:1508.01854]

3. Role of Nuclear Physics in Oscillations of Magnetars .

   Rana Nandi, Prasanta Char, Debarati Chatterjee, Debades Bandyopadhyay;

   Physical Review C, **2016**, *94*, *025801* [arXiv:1608.01241]

Chapters in Books and Lecture Notes: None

Conferences:

1. Core Collapse Supernova Simulation using Λ-hyperon EoS with Density-Dependent Couplings
   Sarmistha Banik, Prasanta Char,
   Proceedings of 20th International Conference on Particles and Nuclei (PANIC 14), **2014**, 391-394, (doi:10.3204/DESY-PROC-2014-04/115).

2. Comparison of Hyperonic Equations of State for Core Collapse Supernovae Simulations
   Prasanta Char, Sarmistha Banik,
   Astronomical Society of India Conference Series, **2015**, *12*, 115-116

Others: None

Prasanta Char

To My Family and Friends.......

ACKNOWLEDGEMENTS

First and foremost, I express my profound gratitude to my advisor Prof. Debades Bandyopadhyay for his continuous support and help throughout the period of my research. I am thankful to him for countless number of discussions, his physics insights and enthusiasm for new ideas. He has always been a tremendous source of motivation and encouragement. His incredible patience and guidance have contributed immensely to my growth as a researcher. I could not have asked for a better advisor and mentor.

Next, I would like to thank Dr. Sarmistha Banik for her invaluable help and constant support to all the projects we have worked together. She has always been there to discuss different problems and helped me to acquire technical skills and knowledge. I am extremely grateful to Dr. Rana Nandi for his help, discussions and guidance for numerical programming. I also want to thank Dr. Debarati Chatterjee for various wonderful discussions on wide range of topics. Without their support, It would have been very hard.

My sincere thanks goes to the faculty members of Astroparticle Physics & Cosmology (APC) division and Theory division of SINP for their guidance and support. I am also thankful to the office staffs of APC and theory divisions for their help. I also acknowledge the financial supports from the Department of Atomic Energy (DAE, Govt. of India) during my Ph.D tenure.

I am extremely grateful to Prof. Stefan Schramm for his kind hospitality and allround support during my visit to Frankfurt Institute of Advanced Studies. Discussions with him have greatly enhanced my knowledge.

Now, I wish to thank my friends who has always stood by me in both good and bad times. Special thanks goes to Goutam, Apurba, Kamakshya, Chandrachur, Mithun, Sourav, Santanu in this regard. I also thank my batchmates Abhijit, Arijit, Asish, Rajendra, Abdul, Arka, Sabyasachi, Gourab for their youthful and enjoyable company. I am particularly thankful to all the fellows of APC and theory divisions who have always maintained a charming and enthusiastic work environment. I want to specially mention Rome, Biswajit, Anshu, Roopam, Amit da, Anirban da, Mainak da, Aminul da, Avirup da, Arindam da, Pritibhajan da, Chiranjib, Naosad, Kuntal, Kumar, Aritra, Mugdha, Sukannya, Rohit for all the stimulating exchange of ideas and fun we had in this entire time.

Finally, I express my deepest respect and gratitude to my family for all the supports they have provided and all the sacrifices they have made for me through my entire life. I am forever indebted to my parents for their unconditional love, affection, patience and support. They are the true driving force of my journey.

Prasanta Char

CONTENTS

Synopsis **iv**

List of Figures **ix**

List of Tables **xiii**

1 Introduction **1**

- 1.1 General Introduction . . . 1
- 1.2 Death of a Massive Star . . . 2
  - 1.2.1 Collapse of the Core . . . 3
  - 1.2.2 The Explosion and the role of neutrinos . . . 4
- 1.3 Equation of State in Stellar Collapse . . . 7
- 1.4 Evolution of the Remnant . . . 8
- 1.5 Structure and Properties of a Neutron Star . . . 9
- 1.6 Asteroseismology of Neutron Star . . . 10

2 Theory of Supernova and Neutron Star Matter **12**

- 2.1 Introduction . . . 12

2.2 Formalism 16

2.3 Model Parameters 23

2.4 Nuclear Statistical Equilibrium Model 25

3 Role of Hyperon Equations of State in Supernova Simulations 28

3.1 Introduction 28

3.2 Methodology 30

3.2.1 BHB$\Lambda\phi$ and HShen Λ EoS tables 30

3.2.2 General relativistic model for supernova simulations 33

3.3 Results and Discussion 36

3.4 Summary and Conclusions 49

4 Effects of Exotic Matter on Neutron Star Structure 51

4.1 Introduction 51

4.2 Formalism 53

4.3 Model Parameters 56

4.4 Results 57

4.5 Summary 65

5 Magnetoelastic Oscillations of Neutron Stars 67

5.1 Introduction 67

5.2 Formalism 70

5.3 Results and Discussions 76

5.3.1 CME modes 79

5.3.2 GME modes 86

5.4 Summary and Conclusions 90

Bibliography **92**

SYNOPSIS

The life cycle of a star having mass higher than 8-10 $M_\odot$ usually ends with a rapid collapse of its Fe-core followed by a violent explosion, called supernova. These core-collapse supernovae (CCSN) are some of the most energetic events in our galaxy. After the collapse, a proto-neutron star (PNS) of very hot and highly dense matter is born with trapped neutrinos. Its central density can reach a few times of the nuclear saturation density. Within a few seconds after the release of the neutrinos, the PNS generally evolves into a neutron star (NS) or a black hole (BH) depending on its mass. A stable NS has temperature far below than the relevant Fermi temperature making it effectively a zero temperature object. These NSs are the most dense objects found in the observable universe. They provide us a unique opportunity to test the theories of matter at densities which cannot be otherwise created at terrestrial laboratories.

A typical NS has mass, $M \sim 1.5M_\odot$, but very small radius, $R \sim 10-12$km. Its density ranges from $10^4 g/cm^3$ at the outer crust to about $10^{15} g/cm^3$ at the inner core . Properties of matter at sub-saturation densities are well constrained by experiments. Attempts have been made to extrapolate those results to predict the nature of matter at supra-nuclear densities and above. But, there are still major uncertainties for both at high densities and

asymmetric nuclear matter. Over the years, various theoretical models have been proposed to explain internal structure and characteristics of NS. It is still an open question whether exotic phases of matter such as hyperons, Bose-Einstein condensates of pions and kaons, and also quarks may exist in the NS interior or not. Astrophysical observations are very crucial in this respect, to put strong constraints on these models. Recent measurements of pulsar masses for PSR J1614-2230 ($1.97 \pm 0.04 M_{\odot}$) in 2010 and PSR J0348+0432 ($2.01 \pm 0.04 M_{\odot}$) in 2011 have tremendous implications for constraining the EoS as pointed out earlier.

Walecka model, a Lorentz covariant theory of dense matter involving baryons and mesons, is arguably the most popular scheme applied widely to calculate the the equation of state (EoS) of neutron star matter. In this model, the relativistic mean-field (RMF) calculations including non-linear scalar meson terms yields the saturation properties of nuclear matter and finite nuclei quite well. But, as the regime above saturation density is not well understood, there are two ways to use it to estimate the high density behavior, 1) to include nonlinear self-interaction terms for scalar and vector fields, 2) to incorporate density dependence through the meson-baryon couplings. The latter may be a suitable approach as higher order field dependence may appear leading to instabilities in the previous one.

Pauli exclusion principle dictates the appearance of strange hadrons in the high density baryonic matter. But, regardless of precise compositions, all possibilities introduce additional degrees of freedom resulting a softening of the EoS of matter, lowering the maximum mass predicted from those EoSs. It has been argued that to overcome this puzzle one may have to incorporate hyperonhyperon repulsive interaction with the exchange of a strange vector meson to make the EoS stiffer.

We were interested to investigate the possibility whether in spite of softening of EoS due to both anti-kaon condensations and hyperons, one can still manage to construct an

EoS with strange matter and achieve a maximum mass compatible with 2 $M_{\odot}$ within observable limit. For this we used a density dependent relativistic field theoretical framework with hyperons and anti-kaon condensates. We also used ϕ-meson for hyperonic and kaonic interaction in addition to σ, ω and ρ mesons of usual extended RMF model. In this framework, we studied the EoS and the compositions of NS matter in $\beta-$equilibrium. In our calculations, we used DD2 parametrization which is used to evaluate the density dependent nucleon-meson couplings , SU(6) relations to determine hyperon-vector meson couplings, hypernuclei data to determine hyperon-scalar meson couplings. We computed the meson-anti(kaon) couplings (for ω and ρ) from the quark model and isospin counting rule and for ϕ-meson we used SU(3) relations. Our results are qualitatively consistent with the results of other models. We also observed that the appearance of strange baryons softened the EoS. But, most of the existing EoSs conflict with the observation of such high pulsar masses. However, in all the cases we found the maximum mass within the constraint of observational limit. Therefore, we concluded that exotic EoSs can not be ruled out by the observation of $2M_{\odot}$ neutron star.

The success of the density dependent hadron field theory model has led to its use in CCSN simulations. Recently, Λ hyperons have been added to this supernova EoS making it one of the very few relativistic supernova EoS tables with Λ hyperons available in literature and the only one to satisfy the observational mass constraint. We conducted a thorough comparative study between this new EoS created by Banik, Hempel and Bandyopadhyay (denoted by BHB$\Lambda\phi$) and the widely used supernova EoS by Shen et. al (denoted by HShen Λ) . Both of these EoSs are applied into a one-dimensional spherically symmetric general relativistic (GR) code $GR1D$ to study the dynamical collapse of a non-rotating massive star into a black hole. It is based on Eulerian formulation of GR hydrodynamics with high resolution shock capturing scheme working with non-equidistant grid. It uses a simplified and computationally efficient treatment of neutrino heating and cooling. Different progenitor stellar models with solar metallicity are used as initial data for the simulations. We studied radial profiles of density, temperature and mass-fractions of the PNS at different instants of time, in great detail. We also examined the temporal evolution of density, temperature, mass-fractions, neutrino luminosity, shock radius etc. of the PNS to carefully distinguish the effects of Λ hyperons on the metastability of the PNS, onset of BH formation etc. It is observed that Λs start appearing in large fraction a few hundred milliseconds after the core bounce. Normally, when the core region reaches density above twice the nuclear saturation density, the onset of Λ hyperon is energetically favored. It also have a distinct effect on BH formation time. As hyperons soften the EoS, black holes form much earlier than the nucleon-only case. Also the neutrino luminosity ceases earlier for both the hyperonic EoSs.

Generally, it is argued that one dimensional simulations fails to produce a successful supernova explosion. Therefore, we used an artificially enhanced neutrino heating scheme and carried out long duration evolution to study the shock radius for a successful supernova explosion and gravitational mass of the remnant PNS. The supernova SN1987A, since its discovery, has become the most studied star remnant in history and has provided great insights into supernovae and their remnants. We studied with a $20M_\odot$ progenitor model similar to the progenitor star of SN1987A and induced an explosion with artificial heating and studied the long duration time evolution of the PNS. We found the shock radius continually expanding and the PNS remaining stable after considerable amount of time. As we did not find any delayed collapse, we concluded that there might be a possibility that stable cold neutron star may exist behind the debris of SN1987A remnant .

Another interesting phenomenon that we studied is the oscillations of highly magnetized neutron stars or the magnetars. Magnetars are one type of neutron stars with a very strong magnetic field $\geq 10^{15}$ G. The change of orientation of this field results in a huge release of energy ($\sim 10^{45}$ ergs/s) as a gamma ray burst. This type of bursts have been observed; thus substantiated the magnetar hypothesis. This flare activity consists of a hard pulse which lasts only for a fraction of a second, followed by a decaying softer part(x-ray/gamma ray tail of the spectrum) which lasts for hundreds of seconds. They are called soft gamma repeaters (SGRs). In this decaying part of the light curve several quasi periodic oscillations(QPOs) have been detected with frequencies in the range of 18 Hz to 1800 Hz . The analysis of the light curve of SGR 1806-20 gives the frequencies of 18, 26, 29, 56, 93, 150, 626, and 1837 Hz. The physical origin of QPOs are proposed as seismic vibrations of the star. This opens the possibility to perform asteroseismological analysis of neutron stars.

We studied the effect of strongly magnetized crust on various oscillatory modes of magnetar. We used the SLy4, SkM and Sk272 nucleon-nucleon interactions and the shear modulus calculated from these models in presence of strong magnetic fields $\geq 10^{17}$ G to study the frequencies of torsional shear modes as well as the global Alfvén modes. The shear modulus increases in strong magnetic fields. But, it is observed that this increase in shear modulus does not affect the frequencies of fundamental torsional shear modes. But, the frequencies of first overtones are markedly different in the strong field case from field-free case. The effect of crust is found to disappear above a critical magnetic field ($B > 4 \times 10^{15}$ G) and both the torsional shear and Alfvén oscillations become magnetic oscillations. Finally, we compared our calculated frequencies using different stellar models, magnetic fields and magnetized crusts with observed frequencies for SGR 1806-20 and SGR 1900+14. We found very good agreement for SGR 1900+14. But, for SGR 1806-20 we found that lower frequencies match well with those of the Alfvén modes, whereas the higher frequencies are better explained with the torsional shear modes.

LIST OF FIGURES

3.1 Mass fractions of different species in the PNS are shown as a function of radius for the HShen Λ EoS (left panel) and the BHB$\Lambda\phi$ EoS (right panel) at t_{pb} = 0.31 and 0.51 s. The results in both panels correspond to the s40WH07 model [108]. 38

3.2 Density profiles of the PNS are shown as a function of radius for the HShen Λ EoS (left panel) and the BHB$\Lambda\phi$ EoS (right panel) at the core bounce and t_{pb} = 0.31 and 0.51 s. The results in both panels correspond to the s40WH07 model [108]. 39

3.3 Temperature profiles of the PNS are shown as a function of radius for the HShen Λ EoS (left panel) and the BHB$\Lambda\phi$ EoS (right panel) at the core bounce and t_{pb} = 0.31 and 0.51 s. The results in both panels correspond to the s40WH07 model [108]. 40

3.4 Same as Figure 3.1 but for the s23WH07 model. The results correspond to the HShen Λ EoS (left panel) and the BHB$\Lambda\phi$ EoS (right panel) at t_{pb} = 0.31 and 0.51 s [108]. 41

3.5 Same as Figure 3.2 but for the s23WH07 model. The results correspond to the HShen Λ EoS (left panel) and the BHB$\Lambda\phi$ EoS (right panel) at the core bounce and $t_{pb} = 0.31$ and 0.51 s [108]. 42

3.6 Same as Figure 3.3 but for the s23WH07 model. The results correspond to the HShen Λ EoS (left panel) and the BHB$\Lambda\phi$ EoS (right panel) at the core bounce and $t_{pb} = 0.31$ and 0.51 s [108]. 43

3.7 Central baryon density is plotted with the postbounce time for the HShen nuclear EoS, the HShen Λ EoS, the HS(DD2) and the BHB$\Lambda\phi$ EoS . The results in the left and right panels correspond to the s40WH07 and s23WH07 models [108]. 44

3.8 Total neutrino luminosity as well as ν_e, $\bar{\nu}_e$ and ν_x luminosities are plotted with the postbounce time for the HS(DD2) (left panel) and the BHB$\Lambda\phi$ (right panel) EoS. The results correspond to the s40WH07 model [108]. 46

3.9 Total neutrino luminosity as well as ν_e, $\bar{\nu}_e$ and ν_x luminosities are plotted with the postbounce time for the HShen Λ (left panel) and the BHB$\Lambda\phi$ (right panel) EoS. The results correspond to the s40WH07 model [108]. 47

3.10 Shock radius (left panel) and gravitational mass of the PNS (right panel) are plotted with the postbounce time using the neutrino heating factor $f_{heat} = 1$ and 1.5 for the s20WH07 model and the BHB$\Lambda\phi$ EoS [108]. 49

4.1 Fraction of various particles in β-equilibrated n, p, Λ and lepton matter including K^- and $\bar{K}^0$ condensates for $U_{\bar{K}}(n_0) = -120$ MeV as a function of normalized baryon density [97]. 59

4.2 Fraction of various particles in β-equilibrated n, p, Λ, Ξ^-, Ξ^0 and lepton matter including K^- and $\bar{K}^0$ condensates for $U_{\bar{K}}(n_0) = -120$ MeV and -140 MeV as a function of normalized baryon density [97]. 60

4.3 The equation of state (EoS), pressure (P) vs energy density (ϵ). The full line is for n, p, and lepton matter whereas others are with additional K^- and $\bar{K}^0$ condensates calculated with $U_{\bar{K}}(n_0)$= -60,-80,-100,-120 and -140 MeV. Deeper $U_{\bar{K}}$ corresponds to softer EoS [97]. 61

4.4 The equation of state (EoS), pressure (P) vs energy density (ϵ) for various particle combination of n, p, Λ, Ξ^-, Ξ^0 and lepton in β-equilibrated matter including K^- and $\bar{K}^0$ condensates with $U_{\bar{K}}(n_0)$=-120 MeV [97]. 62

4.5 The neutron star mass sequences are plotted with radius for the equations of state of Fig. 4.3. The full line is for n, p, and lepton matter whereas others are with additional K^- and $\bar{K}^0$ condensates calculated with $U_{\bar{K}}(n_0)$= -60,-80,-100,-120 and -140 MeV. Deeper $U_{\bar{K}}$ corresponds to lower line. The gray band specifies the observational limits [97]. 63

4.6 The neutron star mass sequences are plotted with radius for the equations of state of Fig. 4.4. The gray band specifies the observational limits [97]. 64

5.1 Shear modulus as a function of mass density for a neutron star of 1.4 $M_\odot$ with magnetic fields $B_* = 0$ and $B_* = 10^4$ and Skyrme nucleon-nucleon interactions of Table 5.1 [191]. 78

5.2 Frequency of fundamental ($n = 0$, $\ell = 2$) CME mode for a neutron star of 1.4 $M_\odot$ is shown as a function of magnetic field $B_* = B/B_c$ where $B_c = 4.414 \times 10^{13}$ G. Results of our calculations using the SLy4, SkM and Sk272 nucleon-nucleon interactions are shown here. [191]. 80

5.3 Fundamental frequencies ($n = 0$) of CME modes are plotted as a function of ℓ values with and without magnetic crusts of a 1.4 $M_\odot$ neutron star based on the SLy4, SkM and Sk272 nucleon-nucleon interactions for $B_* = 10^4$. [191] 81

5.4 Frequencies of first overtones ($n = 1$) of CME modes are shown as a function of ℓ values with and without magnetic crusts of a 1.4 $M_\odot$ neutron star based on the SLy4, SkM and Sk272 nucleon-nucleon interactions for $B_* = 10^4$. [191] . . 82

5.5 Frequencies of CME modes corresponding to $n = 0$ and $\ell = 2, 3, 4$ are plotted as a function of neutron star mass for a magnetic field $B = 8 \times 10^{14}$ G using magnetized crusts based on the SLy4, SkM and Sk272 nucleon-nucleon interactions. [191] 83

5.6 Comparison of the GME frequencies with pure Alfvén frequencies as well as CME frequencies is shown as a function of magnetic field using the magnetized crusts based on the SLy4, SkM and Sk272 nucleon-nucleon interactions. [191] . 86

5.7 GME mode frequencies for $n = 0$ are shown as a function of ℓ values with and without magnetic crusts of a neutron star of mass $1.4M_\odot$ based on the SLy4, SkM and Sk272 nucleon-nucleon interactions for $B_* = 10^4$ [191]. 87

5.8 GME mode frequencies for $n = 1$ are plotted as a function of ℓ values with and without magnetic crusts of a neutron star of mass $1.4M_\odot$ based on the SLy4, SkM and Sk272 nucleon-nucleon interactions for $B_* = 10^4$ [191]. 88

LIST OF TABLES

2.1 Parameters of the meson-nucleon couplings in DD2 model [73] 24

3.1 The saturation properties of nuclear matter such as saturation density (n_0), binding energy (BE), incompressibility (K), symmetry energy (S), and slope coefficient of symmetry energy (L) are obtained using the DD2 and TM1 parameter are obtained using the DD2 and TM1 parameter sets. Maximum masses of cold neutron stars without Λ hyperons corresponding to the HS(DD2) and the HShen EoS are also mentioned here [74, 75, 108]. 32

3.2 Black hole formation time, baryonic and gravitational masses of PNSs for CCSN simulations with the progenitor models of [120] and the BHB$\Lambda\phi$ and HShen Λ EoS tables [108]. 37

4.1 Parameters of the scalar σ meson -(anti)kaon couplings in DD2 model [97]. . . . 57

4.2 Threshold density (in units of n_0) of the K^- ($\bar{K}^0$) condensates in the DD2 model. (-) denotes no-show of them [97]. 58

4.3 Maximum mass, central density and radius of nucleons only as well as hyperon compact stars in the DD2 model. Maximum mass is in $M_{\odot}$, central density with respect to the saturation density n_0, radius in km. [97] 62

4.4 Maximum mass, central density and radius of compact stars with nucleons, hyperons and (anti)kaons for different values of optical potential depth in the DD2 model. Maximum mass is in M_{solar}, central density in n_0, radius in km and $U_{\bar{K}}$ in MeV. [97] 65

5.1 Saturation nuclear matter properties of different Skyrme nucleon-nucleon interactions used in this work such as saturation density (ρ_0), binding energy (BE), incompressibility (K), symmetry energy (J) and its slope coefficient (L) [191] 77

5.2 Radius and crust thickness for all three interactions at $B* = 0$ and $B* = 10^4$ [191] 81

5.3 Frequencies of CME modes calculated using magnetized crusts based on the SLy4, SkM and Sk272 nucleon-nucleon interactions are compared with observed QPO frequencies of SGR 1806-20 [54–56, 153]. The magnetic field used in this calculation is $B = 8 \times 10^{14}$ G. Here f, n and ℓ represent frequency, radial node and angular node, respectively [191]. 84

5.4 Same as Table 5.3 but for SGR 1900+14 [151]. The magnetic field used in this calculation is $B = 4 \times 10^{14}$ G [191]. 85

5.5 GME mode frequencies obtained using the magnetized crusts based on the SLy4, SkM and Sk272 nucleon-nucleon interactions are compared with observed frequencies in SGR 1806-20. The magnetic field used in this calculation is $B = 3.1 \times 10^{15}$ G [191]. 89

5.6 Same as Table 5.5 but for the SGR 1900+14. The magnetic field adopted here is $B = 1.34 \times 10^{15}$ G [191]. 89

CHAPTER 1

INTRODUCTION

1.1 General Introduction

Supernova explosions are the most powerful phenomena observed in nature. A supernova emits energy of the order of 10^{53}erg/s in its first seconds. Most of the energy (99%) is emitted in neutrinos, a small fraction goes into the kinetic and internal energy of the supernova ejecta, a fraction of which is converted into electromagnetic radiation. These explosions make most of the elements in nature and give birth to compact objects such as neutron stars and black holes. Historically, supernovae were characterized by their observed spectra. Type I supernovae don't have hydrogen line, whereas Type II exhibits strong hydrogen lines. Type Ia has strong silicon absorption lines, but Type Ib, Ic don't. Depending on the shape of the light curve Type II supernovae are divided into subclasses Type II-P (plateau), Type II-L (linear), Type IIn (narrow) and Type IIb.

Based on their mechanism, supernovae can be broadly classified into two types :

- Type Ia, in which a white dwarf star accretes mass from its binary companion and once its core reaches the critical temperature to start carbon fusion, it undergoes a runaway thermonuclear reaction leading to the complete disintegration of the star.

- All others (Type II, Ib, Ic etc.) happen when at the end of its lifecycle, the iron core of a massive star exceeds the Chandrasekhar limit and undergoes gravitational collapse to form a neutron star or black hole.

Type Ia supernovae are found in all types of galaxies, but the supernovae powered by the collapse of the stellar core have been observed mainly in the star forming regions. We are interested mainly this kind of core collapse supernovae which occur most frequently in nature. After their prediction by Baade and Zwicky [1] in 1934, scientists have been trying hard to have a detail understanding of their workings. Next major contributions came in the 1960s, when Colgate and the collaborators [2, 3], Arnett [4], Wilson [5] gave solid foundation to the core collapse theory. However, after the supernova SN1987A and also the advancement of high performance computing, there has been rigorous studies and modeling done to shed light on various subtle aspects of a supernova process like hydrodynamics, radiative transfer, dense matter physics, neutrino physics among many more [6–13]. Still, the exact nature of the explosion is not well-understood.

In this chapter, different aspects of the core collapse theory will be discussed along with the currently accepted scenarios of explosion mechanism.

1.2 Death of a Massive Star

A main sequence star spends most of its life generating energy by hydrogen fusion to balance the inward gravitational pull. When the core is depleted of hydrogen, the star starts to collapse again until the ignition temperature of helium is reached and the next stage of fusion starts. For low mass stars ($\sim$8M$_\odot$), no further nuclear fusion occurs after helium because of the lack of sufficient gravity to reach the temperature for carbon fusion. Finally the collapse is halted by electron degeneracy pressure, and the star settles down as a white dwarf.

But for massive stars, the fusion process continues. It continues to go through successive cycles of carbon, neon, oxygen and silicon fusion producing heavier elements with periods of stall, contraction and reignition separating each cycle from the previous. Each of these burning phases is substantially shorter than the earlier one. Whereas the hydrogen and helium burning take millions of years, the silicon burning goes for about two weeks. Eventually, a core of heavy iron-group metal is formed surrounded by concentric shells of silicon, oxygen, neon, carbon, helium and hydrogen. This is famously known as onion shell structure. Further nuclear fusion in core is not possible because binding energy per nucleon is maximum for iron, so further fusion would absorb energy rather than releasing. But, the iron core continues to grow from the silicon burning shell. The final size of the iron core depends very strongly on the initial composition and evolutionary history of the progenitor. It varies roughly from $\sim 1.2M_\odot$ to $\sim 2M_\odot$. Detail reviews on the progenitor evolution can be found in Woosley and Weaver (1986,1995) [14, 15], Woosley, Heger and Weaver (2002) [16].

1.2.1 Collapse of the Core

When the iron core reaches the Chandrasekhar mass, the electron degeneracy pressure can no longer stabilize it and it begins to collapse. At the beginning of the collapse, the typical temperature of the core is about 1 MeV and entropy is about ~ 0.7 to $\sim 1k_B$ per nucleon. The iron core loses its energy by two processes: **i)** electron capture, **ii)** photodisintegration of iron group nuclei to alpha particles. Thus the collapse is accelerated and the core becomes more neutron rich. As the density of inner core reaches from $\sim 10^{10}$g/cm^3 at the start of the collapse to $\sim 10^{12}$g/cm^3, the neutrinos from electron capture are trapped because their diffusion time becomes larger than the collapse time($\sim 10^{-3}$sec). The collapse then proceeds homologously until density reaches $\sim 10^{14}$g/cm^3. At this stage, iron nuclei dissolve into their fundamental constituents forming a uniform nuclear matter. As nuclear matter is compressed further, the repulsive component of the short range nuclear force stops the collapse abruptly. This whole collapse process takes place only in a matter of one second. This is known as core bounce. This drives a shock wave into the outer core and the mantle leading to a supernova explosion. This whole process takes place only in a matter of one second.

After the explosion, the compact remnant left behind is a proto-neutron star (PNS). It is initially very hot and lepton-riched. Its temperature can reach upto 30 MeV. It has a high degree of differential rotation. The core of the PNS has very low entropy whereas it is surrounded by a high entropy mantle which grows steadily by the accretion of infalling material. After a fraction of a second (0.5s) of its birth, the PNS generally cools down significantly by releasing the trapped neutrinos. Also when the trapped neutrinos are released, they carry away most of the gravitational binding energy ($E_b \sim GM_{NS}/{R_{NS}}^2 \sim 10^{53}$ ergs) of the star.

1.2.2 The Explosion and the role of neutrinos

Earlier, it was thought that this shock wave from the bounce would rip apart the outer layer of the star. But, it is now known that the shock wave loses its energy mainly by dissociating heavy nuclei into nucleons and release of neutrinos from the electron capture process in the shock region. After ~ 100 ms the shock stalls completely, and turns into an accretion shock around 100-200 km of radius. The revival of the stalled shock is necessary for a successful supernova explosion. If a fraction of the energy carried away by the neutrinos is deposited into the region between the neutrinosphere and the stalled shock front, it is sufficient to power up the explosion. Although many theories have been proposed how to transfer this energy, like delayed neutrino heating mechanism as proposed by Bethe and Wilson [17] in 1985, magnetohydrodynamic jet production [18, 19], acoustic mechanism [20, 21]; but the exact mechanism is still not known.

In general, neutrino heating and cooling outside neutrinosphere are done by charged current processes of neutrino and anti-neutrino capture onto free neutron and proton respectively and vice versa.

$$\nu_e + n \longleftrightarrow e^- + p \tag{1.1}$$

$$\bar{\nu}_e + p \longleftrightarrow e^+ + n \tag{1.2}$$

However, the cooling rate depends on radius as $\sim r^{-6}$ whereas the heating rate varies as $\sim r^{-2}$. So, after certain distance termed as "gain radius" heating becomes a dominant process [9, 17]. If the energy deposition is sufficiently strong and faster than the advection timescale of the gain region, it can lead to a shock revival and ultimately an explosion.

But, it was soon realized that the matter-neutrino interactions is more than just the two processes indicated above. It includes nucleon-nucleon bremsstrahlung ($N + N \leftrightarrow N + N + \nu_i + \bar{\nu}_i$), pair creation of all flavours ($e^- + e^+ \leftrightarrow \nu_i + \bar{\nu}_i$), plasmon decay ($\gamma^* \leftrightarrow \nu_i + \bar{\nu}_i$) and also scattering reactions between neutrino, antineutrino, electrons, positrons and nuclei [22–25]. But, except for very light progenitor models ($\sim 8 - 9 M_\odot$) in very special cases (with steep density gradient in pre-supernova structure), in almost all of the 1D spherically symmetric simulation with detailed general relativistic neutrino transport, delayed neutrino heating scheme fails to revive the shock [26]. Also, the canonical explosion energy from the successful explosions is much lower than the observation [27]. The reason of this behavior can be explained as the neutrino transport in the gain region creates convective processes, certain types of hydrodynamical instabilities that can not be properly implemented in 1D simulations. Therefore, it has been a theoretical challenge to update properly the delayed neutrino heating mechanism in 2D and in 3D.

There are many sources that break the spherical symmetry of the supernova environment e.g. nonradial oscillations, neutrino-driven buoyancy [28], violent turbulence created due to negative entropy gradient behind the shock [8]. One of the most prominent source is standing accretion shock instability (SASI) [29]. It is mainly associated with the oscillatory motion of the shock surface. The time period is comparable to the advection timescale from neutron star surface to shock. The instability arises when the global mode perturbation $(l = 1)$ grows significantly with time [30]. These multidimensional effects when included in the neutrino scheme enhances the neutrino-matter interaction and neutrino heating efficiency. First successful explosion from first principle was obtained by Marek and Janka [31] for 11.2 and $12 M_\odot$ progenitors using ray-by-ray neutrino transport including general relativistic effects. There are also 2D results from other groups [32, 33]. The effect of SASI was found in all of them. But, in the most general scenario, we have to consider the 3D nature of the collapse phenomena. Presently, due to the lack of computational infrastructure and robust mechanism to include the turbulence flow due to advection and other energy exchanges, very few simulation results in 3D exists [34, 35]. There are some qualitative differences between 2D and 3D simulations of Core Collapse Supernova (CCSN) in the postbounce evolution of shock radius, post shock flow etc. Also it was found difficult to explode in 3D than in 2D. The net neutrino-heating requirement in 3D was found 30% higher than in 2D. But, in case of an successful explosion, it was also seen that the 3D models explode earlier than the 2D models [36].

1.3 Equation of State in Stellar Collapse

The equation of state (EoS) of matter plays a very important role on the collapse, bounce and the formation of neutron star and black holes. It can also substantially effect the neutrino luminosity, shock formation and evolution of shock radius [10]. Extremely high densities and temperatures can occur at the onset of black hole formation. In a typical core collapse event, the density varies from 10^4 g/cm^3 to 10^{15} g/cm^3, the temperature varies from 0 MeV to 100 MeV and the lepton fraction varies from 0 to 0.6. It is very difficult to construct an EoS in a self consistent way to cover these wide range of parameters which is beyond the scope of the laboratory experiments. So, the basic framework is to extrapolate based on the theoretical models which are consistent with the nuclear experimental data. The very first nuclear EoS was provided by Hillebrandt and Wolff in 1985 [37]. But, the most widely used supernova EoSs are from Lattimer and Swesty in 1991 (LS) [38] and Shen et al. in 1998 (HShen) [39]. The LS EoS is based on the non relativistic Skyrme-type interaction with two and many body terms for uniform high density matter and compressible liquid drop model is used to describe low density non uniform matter. On the other hand, HShen EoS is based on a relativistic field theoretical model for high density and Thomas Fermi approximation is used for non uniform matter at low temperature and low density. In both these EoSs, constituents are free nucleons, light nuclei, ideal gas of nuclei and uniform nuclear matter, single nucleus approximation was employed, shell effects were neglected. In recent years, with updated nuclear data and better understanding, several new EoSs were developed. Among them, most notable one is by Hempel and Schaffner-Bielich in 2010 (HS) [40]. It treats an entire distribution of nuclei and nucleons within the nuclear statistical equilibrium (NSE) model in a thermodynamically consistent way. Also, several EoSs were recently updated to include exotic form of matter i.e. hyperons by Ishizuka et al. in 2008 [41], Shen et al. in 2011 [42], Oertel et al. in 2012 [43], Banik et al. in 2014 [44] and quarks by Sagert et al. in 2009 [45]. A second neutrino burst corresponding to the quark-hadron phase transition was found by Sagert et al. in the simulations using their quark EoS model. But, only one of these EoSs [44] satisfies the recent observational maximum mass limit of $2M_{\odot}$. The effects of this constraint on the depiction of matter and the supernova explosion are discussed in great details in the following chapters and constitute the core of this thesis.

1.4 Evolution of the Remnant

The evolution of the PNS may occur in several different directions. Just after its birth, if the core is massive enough, the thermal pressure and the rotation cannot sustain it, and it promptly collapse into a black hole after accreting sufficient material. In another scenario, after deleptonization the chemical potential inside the core of PNS changes. This changes the threshold density of strange hyperons, anti-kaon condensates etc. which will soften the equation of state of the matter consequently reducing the maximum sustainable mass. Now, if enough accretion occurs, there is a possibility of black hole formation afterwards. This delayed collapse scenario is called the metastability. It was studied extensively by Brown and Bethe [46] in search for a distribution of low-mass black holes in the galaxy. The last scenario is the evolution of the PNS into a cold neutron star (NS). Generally, in this case, the progenitor is smaller. So, the initial PNS mass is not very high for prompt collapse. Also, the rate of accretion is not very high. After the release of trapped neutrinos, the entropy of the PNS gets higher. There are still a large number of thermally generated neutrinos of all flavours inside the star. The thermal neutrinos diffuse in the timescale ~ 50 seconds, as the cooling of the hot NS takes place. At this stage, the NS is virtually transparent for neutrinos. It attains beta equilibrium. Its temperature drops down to 1-2 MeV. The mass accretion is now over. The crust and the core have different neutrino emissivity and thermal conductivity. So, their cooling rates are also different. It takes almost 100 years to achieve thermal equilibrium depending on NS radius and thermal conductivity of the crust.

1.5 Structure and Properties of a Neutron Star

Neutron stars are the densest known objects in the observable universe. Its density varies from 2-5 times the nuclear saturation density ($\rho_0 = 2.7 \times 10^{14}$ g/cm^3) at the core to ($\sim 10^4$ g/cm^3) at the outer crust. Its compositions also change drastically from crust to core. The outer crust consists of Fe-group nuclei in BCC lattice immersed in degenerate electron gas. After this layer, we have the inner crust where the neutrons start coming out of the nuclei when the density reaches the neutron drip point. As the density goes higher, the matter undergoes a series of transitions of different shapes which is now called the ’pasta’ phase. At the crust core interface, nuclei completely dissolve to form neutron-rich nuclear matter. From outer core to inner core, the density rises even higher and may finally rich many times ρ_0 at the center and become uniform nuclear matter. Generally, the structure of both hot and cold NS, depends on the equation of state of compositions of matter at very high densities. So, the accurate measurements of mass and radius of a cold NS can impose very strong constraints on the properties of matter.

Measurements of isolated neutron star are still not possible. But, precise measurements are done for a NS in a binary system using pulsar timing. In this systems, the five Keplerian parameters measured are period (P), projection of semi-major axis along the line of sight ($a \sin i$), eccentricity (e), periastron time (T_0) and longitude (ω). Properly constraining these parameters, the mass of the NS is estimated. Also, in some compact binaries, relativistic effects on the orbit can also be measured. These are called post-Keplerian parameters, namely periastron advance of the orbit ($\dot{\omega}$), gravitational redshift (γ), orbital period decay due to gravitational radiation ($\dot{P}$) and the Shapiro time delay.

The discovery of binary pulsar PSR 1913+16 in 1974 by Hulse and Taylor lead to first precise measurement of neutron star mass ($1.4408 \pm 0.0003 M_\odot$) [47]. The millisecond pulsar PSR 1903+0327 of $1.67 \pm 0.02 M_\odot$ [48], measured in 2008, PSR J1614-2230 of $1.97 \pm 0.04 M_\odot$ [49] in 2010 and PSR J0348+0432 of $2.01 \pm 0.04 M_\odot$ [50] subsequently in 2011 have raised the bar. The knowledge of the precisely measured mass of neutron stars has important consequences for constraining the equation of state of dense matter. It can throw light on otherwise poorly known composition of the compact star core.

There is no direct measurement of radius available for neutron stars with accurate mass measurements till now. But, many indirect observation techniques have been proposed. Thermal emission spectrum from the surface can be analyzed to probe the radius. Also, the measurements of moment of inertia and pulsar glitches can put constraint on the radius. In future, the Square Kilometer Array will be able to precisely measure the moment of inertia from spin-orbit coupling, upto second order post-Newtonian corrections to periastron advance [51].

1.6 Asteroseismology of Neutron Star

Magnetars are one type of neutron stars with a very strong surface magnetic field $\sim 10^{14} - 10^{15}$ G. The existence of this kind of objects was first proposed by Duncan and Thompson in 1992 [52]. There are two groups of objects that satisfy the criteria - $a)$ Soft Gamma Repeaters (SGR) and $b)$ Anomalous X-Ray Pulsars (AXP). The main characteristics of these objects are: a) they are isolated objects, b) their spin period is relatively longer than the pulsars ($\sim 1 - 10$s), c) they also have very large spin down rates ($\dot{P} \sim 10^{-13} - 10^{-11}$ s s^{-1}) There are three kind of bursts observed from these objects: 1) short bursts with duration of $\sim 0.1 - 10$s and peak luminosity $\sim 10^{39} - 10^{41}$ ergs/s, associated with both SGRs and AXPs, 2) intermediate bursts with duration of $\sim 1 - 40$s and peak luminosity $\sim 10^{41} - 10^{43}$ ergs/s, associated with both SGRs and AXPs and 3) giant flares which consists of a hard pulse which lasts only for a fraction of a second, followed by a decaying softer part(x-ray/gamma ray tail of the spectrum) which lasts for hundreds of seconds. The peak luminosity of giant flares can rise upto $\sim 10^{44} - 10^{46}$ ergs/s. These are observed only in SGRs [53]. Generally, the dissipation and decay of very strong magnetic field on the surface causes a change of orientation of the field which is considered to be the main cause of this huge release of energy in SGRs. Most recent giant flare event (SGR 1806-20) was observed in December, 2004 [54–56]. In the decaying part of the light curve of SGR 1806-20 as several quasi periodic oscillations(QPOs) have been detected with frequencies in the range of 18 Hz to 1800 Hz. The analysis of the light curve of SGR 1806-20 gives the frequencies of 18, 26, 30, 92.5, 150, 626, and 1838 Hz. The physical origin of the QPOs are proposed as seismic vibration of the star. This opens the possibility to perform asteroseismological analysis of neutron star.

This thesis is organized the following way. In chapter 2, the theory of dense matter is discussed. Then, the results from core collapse supernova simulations using hyperon EoSs are described in chapter 3. Following that, the possibility of exotic matter in cold NS is discussed in chapter 4, and finally in chapter 5, the role of nuclear physics in the oscillations of highly magnetized neutron stars is discussed.

CHAPTER 2

THEORY OF SUPERNOVA AND NEUTRON STAR MATTER

2.1 Introduction

Since the early ages of nuclear physics, there have been numerous attempts to provide the theoretical description of infinite nuclear matter and properties of finite nuclei and also neutron rich matter. Most of them rely on the phenomenological modeling. Quantum Chromodynamics is the ideal theory to describe matter at the most fundamental level. But, for low temperature and moderately high density i.e. in the case of cold nuclear matter, no useful solution of QCD exists. So, we have to rely on effective theories which are relevant to the hadronic scale. Many theoretical models have been proposed over the past century to explain the characteristics of nuclear matter, from the semi-empirical mass formula of Bethe-Weizsäcker [57] in 1935, non-relativistic Skyrme models [58, 59] in the 1950s to the quantum hadrodynamics models [60] developed by Walecka in 1974 etc. The studies in nuclear physics have progressed in mainly two directions: microscopic many-body calculations using realistic nucleon-nucleon potentials and phenomenological relativistic and nonrelativistic mean-field theories [61]. All of these models are written in terms of parameters which are fitted to reproduce the properties at the saturation densities. So, at that point they all behave approximately in the same way, but differ significantly both at subsaturation densities and also suprasaturation densities [62].

Historically, the theory of nucleus was developed following the atomic theory as a collection of non-relativistic nucleons interacting through instantaneous two-body nucleon-nucleon potential, so that it could be solved by the Schrödinger equation. This potential was fitted with the low energy nuclear scattering data and properties of deuteron. How ever, this potential is strong and short range which makes it very difficult to solve. Over the years, several sophisticated methods such as variational chain summation, quantum Monte Carlo method etc. were developed to solve for the wave function and find correlations in many body systems [63, 64]. These methods are computationally intensive.

Another significant approach to realistic nucleon potential is Bethe-Bruekner-Goldstone (BBG) method which starts from bare nucleon-nucleon interaction as determined from scattering data [65]. It is a many body theory where in-medium effects on the nucleon-nucleon interaction are incorporated within the Brueckner reaction matrix G which is calculated using perturbative expansion. Recent studies have shown that the nuclear EoS can be estimated with good accuracy in the Brueckner two-hole line approximation with the continuous choice for the single-particle potential [66]. But non-relativistic pure two-body potential fails to reproduce the correct nuclear saturation point. There have been several attempts to improve the theory including three-body forces in Urbana Model and Bonn B potentials. But, symmetry energy, incompressibility are very important properties which can not be determined and the speed of sound may also become superluminal at higher density.

The relativistic version of BBG method is known as Dirac-Brueckner-Hartree-Fock (DBHF) theory. Here, the nucleon-nucleon interactions are one-boson-exchange type [67]. In this scheme, the free particle energy eigenstates satisfy the Dirac equation and the G matrix and the self energy Σ are solved self consistently. This theory reproduces the nuclear saturation properties much better than the original BBG theory.

There are also several mean field theories both the non-relativistic Skyrme type and the relativistic Walecka type. In these models, the nucleon-nucleon scattering is abandoned in favour of phenomenological interactions. The parameters of the model are fitted to empirical properties of bulk nuclear matter at nuclear saturation density.

However, it should be emphasized that physical phenomena of interest are relativistic and involves creation and annihilation of particles. So, a consistent framework to describe such processes should be based on relativistic quantum field theory based on a Lorentz covariant Lagrangian density. These theories are commonly referred as quantum hadrodynamics (QHD) [60, 68, 69]. Walecka first proposed such kind of a model involving baryons and mesons to provide a simplified understanding of nuclei and nuclear matter. This is a relativistic field theoretical model in which nuclear interaction in matter is mediated by the scalar meson σ and the vector meson ω. This is traditionally known as the meson exchange model. Later, the vector-isovector ρ meson was also included in this scheme to incorporate the isospin degree of freedom and extensively studied in the mean field approximation. The model including non-linear scalar meson terms yields the saturation properties of nuclear matter and finite nuclei quite well. However, regime above saturation density is not well understood. Extrapolating the nuclear matter properties to high density leads to uncertainties. In most of the relativistic mean field (RMF) calculations, non-linear self interaction terms for scalar and vector fields are introduced to account for the high density behaviour [70]. But this may not be a reliable approach due to instabilities caused by divergence in self-interaction terms and higher order field dependence that may appear at high densities. Another more suitable approach is to incorporate the density-dependence through the meson-baryon couplings [71–73]. In the density dependent model the appearance of a rearrangement term in baryon chemical potential significantly changes the pressure, consequently the equation of state (EoS) at higher densities. It is a thermodynamically consistent model and can be applied to systems beyond normal nuclear matter.

We must also consider the role of nuclear symmetry energy, the energy associated with the isospin asymmetry, on the behaviour of the EoS at high densities. The nuclear symmetry energy alters the stiffness of the EoS. It is of great importance, along with its density dependence, in studying many crucial problems in astrophysics, such as neutronization in core collapse supernova explosion, neutrino emission from protoneutron star (PNS), neutron star radii, crust thickness, cooling among various others [74]. The symmetry energy and its density dependence near the saturation density n_0 are denoted by $S_\nu = E_{sym}(n_0)$ and slope parameter $L = 3n_0 dE_{sym}/dn|_{n=n_0,T=0}$ respectively. These parameters can be constrained by the findings of precise nuclear physics experiments (heavy ion collision analysis, dipole polarizability analysis etc.) as well as astrophysical observations. The bounds on the parameters are found to be 29 MeV $< S_\nu <$ 32.7 MeV and 40.5 MeV $< L <$ 61.9 MeV respectively [74, 75]. Now if we look into the most popular and widely used parametrizations to model neutron star structure, such as GM1, TM1, NL3 etc., we find that the values of both symmetry energy and its slope parameters in all these cases (For GM1, $S_\nu = 32.47$ MeV and $L = 93.8$ MeV; TM1, $S_\nu = 36.95$ MeV and $L = 110.99$ MeV; NL3, $S_\nu = 37.39$ MeV and $L = 118.49$ MeV [75]) do not quite fall into the experimental range. Whereas the density dependent (DD2) RMF model, we are going to use in the studies described in this thesis, with $S_\nu = 31.67$ MeV and $L = 55.04$ MeV, are fully consistent with the above experimental and observational constraints [73]. In fact, it is the only relativistic EoS model with linear couplings. Also the DD2 EoS model agrees well with the predictions by Chiral EFT [75]. However it should be noted that the density dependent parametrization (DD) was in use [71, 76, 77] even before this symmetry energy experimental data was available. The current DD2 model differs from the previous DD model only by the use of experimental nuclear masses [73].

2.2 Formalism

We study the hadrons within the framework of a density dependent hadron field (DDRH) theory. It is a QHD model where nucleon-meson couplings are determined from the self energies calculated in DBHF scheme using nucleon-nucleon potentials. So, many body effects of nucleon interactions are incorporate in the model by construction [76]. In the present approach, the model Lagrangian density ($\mathcal{L} = \mathcal{L}_B + \mathcal{L}_l$) is of the form

$$\begin{aligned}
\mathcal{L}_B &= \sum_{B=N} \bar{\psi}_B \left(i\gamma_\mu \partial^\mu - m_B + g_{\sigma B}\sigma - g_{\omega B}\gamma_\mu \omega^\mu - g_{\rho B}\gamma_\mu \boldsymbol{\tau}_B \cdot \boldsymbol{\rho}^\mu\right) \psi_B \\
&\quad + \frac{1}{2}\left(\partial_\mu \sigma \partial^\mu \sigma - m_\sigma^2 \sigma^2\right) - \frac{1}{4}\omega_{\mu\nu}\omega^{\mu\nu} \\
&\quad + \frac{1}{2}m_\omega^2 \omega_\mu \omega^\mu - \frac{1}{4}\boldsymbol{\rho}_{\mu\nu} \cdot \boldsymbol{\rho}^{\mu\nu} + \frac{1}{2}m_\rho^2 \boldsymbol{\rho}_\mu \cdot \boldsymbol{\rho}^\mu . \qquad (2.1)
\end{aligned}$$

Leptons are treated as non-interacting particles and described by the Lagrangian density

$$\mathcal{L}_l = \sum_l \bar{\psi}_l \left(i\gamma_\mu \partial^\mu - m_l\right) \psi_l \, . \qquad (2.2)$$

Here ψ_l ($l \equiv e, \mu$) is lepton spinor whereas ψ_B denotes the nucleons ($N \equiv n, p$). The nucleons interact via the exchange of scalar σ, vector ω, ρ mesons; $\boldsymbol{\tau_B}$ is the isospin operator.

The $g_{\alpha B}(\hat{n})$'s, where $\alpha = \sigma,\ \omega$ and ρ specify the coupling strength of the mesons with baryons. However, we can choose the density dependence of the meson-baryon couplings in two ways - scalar density dependence (SDD) and vector density dependence (VDD). Here we consider the couplings as vector density-dependent. The density operator $\hat{n}$ has the form, $\hat{n}$=$\sqrt{\hat{j}_\mu \hat{j}^\mu}$, where $\hat{j}_\mu = \bar{\psi}\gamma_\mu\psi$. Also, the meson-baryon couplings become function of total baryon density n [71, 73] i.e.

$$\langle g_{\alpha B}(\hat{n})\rangle = g_{\alpha B}(\langle \hat{n}\rangle) = g_{\alpha B}(n). \tag{2.3}$$

The field strength tensors for the vector mesons are given by

$$\omega^{\mu\nu} = \partial^\mu \omega^\nu - \partial^\nu \omega^\mu \tag{2.4}$$

$$\boldsymbol{\rho}^{\mu\nu} = \partial^\mu \boldsymbol{\rho}^\nu - \partial^\nu \boldsymbol{\rho}^\mu. \tag{2.5}$$

This Lagrangian structure closely follows the formalism of Typel et al. [72, 73].

The recent discovery of a 2 $M_\odot$ neutron star puts stringent conditions on the composition and equation of state (EoS) of dense matter in neutron star interiors [50]. Pauli exclusion principle dictates the appearance of strangeness degrees of freedom such as hyperons in the high density baryonic matter. But, it has been shown in many studies that the presence of hyperons makes the EoS softer, which lowers maximum attainable mass of the neutron star. So, it is incompatible with the measured neutron star masses. This is known as the hyperon puzzle [78, 79]. Therefore, describing hyperon matter in neutron stars is a challenge in many-body theories. It has been argued that the hyperon-hyperon repulsive interaction due to the exchange of strange vector meson makes the EoS stiffer and might overcome the puzzle.

Therefore, the above model has been extended to accommodate the whole baryon octet. The interaction of hyperons with the nucleons is considered through meson exchange just like the nucleon-nucleon interaction. However, an additional strange vector meson ϕ is also included, which is important for the the hyperon-hyperon interaction only [70, 80]. Interaction among hyperons can be represented by the Lagrangian density

$$\begin{aligned}\mathcal{L}_{YY} &= \sum_{B=\Lambda,\Sigma,\Xi} \bar{\psi}_B \left(g_{\sigma^* B}\sigma^* - g_{\phi B}\gamma_\mu \phi^\mu\right)\psi_B + \frac{1}{2}\left(\partial_\mu \sigma^* \partial^\mu \sigma^* - m_{\sigma^*}^2 \sigma^{*2}\right) \\ & -\frac{1}{4}\phi_{\mu\nu}\phi^{\mu\nu} + \frac{1}{2} m_\phi^2 \phi_\mu \phi^\mu \ , \end{aligned} \tag{2.6}$$

where, the field strength tensor for ϕ is given by,

$$\phi^{\mu\nu} = \partial^\mu \phi^\nu - \partial^\nu \phi^\mu . \tag{2.7}$$

It has been reported that the attractive hyperon-hyperon interaction mediated by σ^* meson is very weak [70]. We neglect the contribution of σ^* meson in this calculation.

Using Euler-Lagrange relation the equations of motion for the meson and baryons fields are easily derived from the total Lagrangian density ($\mathcal{L} = \mathcal{L}_B + \mathcal{L}_l + \mathcal{L}_{YY}$). The density dependence of the couplings while computing variation of $\mathcal{L}$ with respect to ψ_B gives rise to an additional term.

$$\frac{\delta \mathcal{L}}{\delta \bar{\psi}_B} = \frac{\partial \mathcal{L}}{\partial \bar{\psi}_B} + \frac{\partial \mathcal{L}}{\partial \hat{\rho}_B}\frac{\delta \hat{\rho}_B}{\delta \bar{\psi}_B} \ . \tag{2.8}$$

This is denoted as the rearrangement term $\Sigma^{(r)\mu}$ [71, 73], where

$$\Sigma^{(r)\mu} = \sum_B \frac{\partial \mathcal{L}}{\partial \hat{\rho}_B}\frac{\delta \hat{\rho}_B}{\delta \bar{\psi}_B} \ . \tag{2.9}$$

This term adds to the vector self energy which is a major difference between usual RMF models with self-interaction and DDRH theory.

The meson field equations are solved self-consistently keeping into consideration the conditions for charge neutrality and baryon number conservation. We consider a static and isotropic matter in the ground state. For such a static system, all space and time derivatives of the fields vanish. Also, in the rest frame of the matter the space components of ω_μ, ρ_μ and ϕ_μ vanish. Furthermore, the third component of the isovector ρ meson couples to baryons because the expectation values of the sources for charged ρ mesons in the equation of motion also vanish in the ground state. It is to be noted ϕ mesons do not couple with nucleons i.e. $g_{\phi N} = 0$. The meson field equations are solved in the mean-field approximation where the meson fields are replaced by their expectation values. The meson field equations are given by

$$\begin{aligned} m_\sigma^2 \sigma &= \sum_B g_{\sigma B} n_B^s \ , && (2.10) \\ m_\omega^2 \omega_0 &= \sum_B g_{\omega B} n_B \ , && (2.11) \\ m_\rho^2 \rho_{03} &= \sum_B g_{\rho B} \tau_{3B} n_B \ , && (2.12) \\ m_\phi^2 \phi_0 &= \sum_B g_{\phi B} n_B \ , && (2.13) \end{aligned}$$

We are considering a degenerate ground state. The number density and scalar number density for the baryon B are given by,

$$\begin{aligned} n_B &= \langle\bar{\psi}_B\gamma_0\psi_B\rangle = \frac{k^3_{F_B}}{3\pi^2} \ , \qquad (2.14)\\ n^s_B &= \langle\bar{\psi}_B\psi_B\rangle = \frac{2J_B+1}{2\pi^2}\int_0^{k_{F_B}} \frac{m^*_B}{(k^2+m^{*2}_B)^{1/2}}k^2\, dk \\ &= \frac{m^*_B}{2\pi^2}\left[k_{F_B}\sqrt{{k_{F_B}}^2+m^{*2}_B} - m^{*2}_B ln\frac{k_{F_B}+\sqrt{{k_{F_B}}^2+m^{*2}_B}}{m^*_B}\right] \ . \qquad (2.15)\end{aligned}$$

Here, J_B is spin projection of baryon B.

The Dirac equation for the spin $\frac{1}{2}$ particles is modified with the inclusion of the rearrangement self-energy and given by

$$\left[\gamma_\mu\left(i\partial^\mu - \Sigma^\mu_B\right) - m^*_B\right]\psi_B = 0. \qquad (2.16)$$

The effective baryon mass is defined as $m^*_B = m_B - g_{\sigma B}\sigma$, with m_B as the vacuum rest mass of baryon B whereas $\Sigma^0_B = \Sigma^{(0)0}_B + \Sigma^{(r)0}_B$ is the vector self-energy. The first term in the vector self-energy consists of the usual non-vanishing components of the vector mesons i.e.

$$\Sigma^{(0)0}_B = g_{\omega B}\omega_0 + g_{\rho B}\tau_{3B}\rho_{03} + g_{\phi B}\phi_0 \ , \qquad (2.17)$$

while the second term is rearrangement term, which arises due to density-dependence of the meson-baryon coupling constants [71], assumes the form

$$\Sigma^{(r)0}_B = \sum_B[-g'_{\sigma B}\sigma n^s_B + g'_{\omega B}\omega_0 n_B + g'_{\rho B}\tau_{3B}\rho_{03}n_B + g'_{\phi B}\phi_0 n_B] \ , \qquad (2.18)$$

where $g'_{\alpha B} = \frac{\partial g_{\alpha B}}{\partial \rho_B}$, $\alpha = \sigma,\ \omega,\ \rho,\ \phi$ and τ_{3B} is the isospin projection of $B = n, p, \Lambda, \Sigma^-, \Sigma^0$, Σ^+, Ξ^-, Ξ^0. Charge neutrality and β-equilibrium conditions are imposed on neutron star matter. Baryons and leptons are in chemical equilibrium governed by the general equilibrium condition,

$$\mu_i = b_i \mu_n - q_i \mu_e \;, \tag{2.19}$$

where, b_i is the baryon number, q_i is the charge of ith baryon, μ_n is the chemical potential of neutrons and μ_e is that of electrons. This condition determines the threshold of a particular hyperon. As the chemical potential of the neutron and electron become sufficiently large at high density and eventually the threshold of hyperons are reached, they are populated. The chemical potential for the baryon B is

$$\mu_B = \sqrt{k_B^2 + m_B^{*2}} + g_{\omega B}\omega_0 + g_{\rho B}\tau_{3B}\rho_{03} + g_{\phi B}\phi_0 + \Sigma_B^{(r)0}, \tag{2.20}$$

where the term $g_{\phi B}\phi_0$ in μ_B is applicable for hyperons only. The energy density due to baryons can be explicitly expressed as

$$\begin{aligned}\varepsilon_B &= \frac{1}{2}m_\sigma^2\sigma^2 + \frac{1}{2}m_\omega^2\omega_0^2 + \frac{1}{2}m_\rho^2\rho_{03}^2\frac{1}{2}m_\phi^2\phi_0^2 \\ &\quad + \sum_B \frac{2J_B+1}{2\pi^2}\int_0^{k_{F_B}} (k^2 + m_B^{*2})^{1/2} k^2\, dk. \end{aligned}\tag{2.21}$$

The expression for pressure due to baryons [81, 82] is given by,

$$\begin{aligned}P_B &= -\frac{1}{2}m_\sigma^2\sigma^2 + \frac{1}{2}m_\omega^2\omega_0^2 + \frac{1}{2}m_\phi^2\phi_0^2 + \frac{1}{2}m_\rho^2\rho_{03}^2 + \Sigma_B^{(r)0}\sum_B n_B \\ &\quad + \frac{1}{3}\sum_B \frac{2J_B+1}{2\pi^2}\int_0^{k_{F_B}} \frac{k^4\, dk}{(k^2 + m_B^{*2})^{1/2}}. \end{aligned}\tag{2.22}$$

It also contains the additional rearrangement term ($\Sigma_B^{(r)0}$). The pressure (P_B) is also related to the energy density (ε_B) in this phase through the Gibbs-Duhem relation

$$P_B = \sum_i \mu_i n_i - \varepsilon_B \,. \tag{2.23}$$

The rearrangement term does not contribute to the energy density explicitly, whereas it occurs in the pressure through baryon chemical potentials. It is the rearrangement term that accounts for the energy-momentum conservation and thermodynamic consistency of the system [71]. Similarly, we calculate number densities, energy densities and pressures of electrons, muons and those are given by,

$$\begin{aligned} n_l &= \langle \bar{\psi}_l \gamma_0 \psi_l \rangle = \frac{k_{F_l}^3}{3\pi^2} \,, & (2.24)\\ \varepsilon_l &= \sum_l \frac{1}{\pi^2} \int_0^{K_{F_l}} (k^2 + m_l^2)^{1/2} k^2 \, dk \,, & (2.25)\\ P_l &= \frac{1}{3} \sum_l \frac{1}{\pi^2} \int_0^{K_{F_l}} \frac{k^4 \, dk}{(k^2 + m_l^2)^{1/2}} \,, & (2.26) \end{aligned}$$

To construct an EoS suitable for supernova simulation, we have to go beyond zero temperature and β-equilibrium. At finite temperature T, the number density and scalar number density for the baryon B are calculated by integrating over all available momenta states k [81, 82] and given by,

$$\begin{aligned} n_B &= 2 \int \frac{d^3k}{(2\pi)^3} \left(\frac{1}{e^{\beta(E^* - \nu_B)} + 1} - \frac{1}{e^{\beta(E^* + \nu_B)} + 1} \right) \,, & (2.27)\\ n_B^S &= 2 \int \frac{d^3k}{(2\pi)^3} \frac{m_B^*}{E^*} \left(\frac{1}{e^{\beta(E^* - \nu_B)} + 1} + \frac{1}{e^{\beta(E^* + \nu_B)} + 1} \right) \,, & (2.28) \end{aligned}$$

with the energy $E^* = \sqrt{k^2 + m_B^{*2}}$ and $\beta = 1/T$, including contributions from both particles and antiparticles. The thermodynamic potential per unit volume for baryons is given by,

$$
\begin{aligned}
\frac{\Omega}{V} &= \frac{1}{2}m_\sigma^2\sigma^2 - \frac{1}{2}m_\omega^2\omega_0^2 - \frac{1}{2}m_\phi^2\phi_0^2 - \frac{1}{2}m_\rho^2\rho_{03}^2 - \Sigma^{r(0)} \sum_{B=N,\Lambda,\Sigma,\Xi} n_B \\
&-2T \sum_{B=N,\Lambda,\Sigma,\Xi} \int \frac{d^3k}{(2\pi)^3} \left[ln(1+e^{-\beta(E^*-\nu_B)}) + ln(1+e^{-\beta(E^*+\nu_B)})\right] . \qquad (2.29)
\end{aligned}
$$

Now, we can evaluate the thermodynamic quantities at finite temperature T such as pressure $P = -\Omega/V$ and energy density

$$
\begin{aligned}
\varepsilon_B &= \frac{1}{2}m_\sigma^2\sigma^2 + \frac{1}{2}m_\omega^2\omega_0^2 + \frac{1}{2}m_\phi^2\phi_0^2 + \frac{1}{2}m_\rho^2\rho_{03}^2 \\
&+2\sum_B \int \frac{d^3k}{(2\pi)^3} E^* \left(\frac{1}{e^{\beta(E^*-\nu_B)}+1} + \frac{1}{e^{\beta(E^*+\nu_B)}+1}\right) . \qquad (2.30)
\end{aligned}
$$

Similarly, the entropy density is given by,

$$
s = \beta(\varepsilon_B + P_B - \sum_{i=N,\Lambda,\Sigma,\Xi} \mu_i n_i) . \qquad (2.31)
$$

Entropy per baryon is given by, $S = s/n$, where n is the total baryon density ($n = \sum_B n_B$).

2.3 Model Parameters

The nucleon-meson density-dependent couplings are determined following the prescription of Typel et. al [72, 73]. The functional dependence of the couplings on density was first introduced in [83] and is described as

$$
g_{\alpha B}(n_b) = g_{\alpha B}(n_0) f_\alpha(x), \qquad (2.32)
$$

Table 2.1: Parameters of the meson-nucleon couplings in DD2 model [73]

meson α	$g_{\alpha B}$	a_α	b_α	c_α	d_α
ω	13.342362	1.369718	0.496475	0.817753	0.638452
σ	10.686681	1.357630	0.634442	1.005358	0.575810
ρ	3.626940	0.518903			

where n_b is the total baryon density defined as, $n_b = \sum_B n_B$, $x = n_b/n_0$, and

$$f_\alpha(x) = a_\alpha \frac{1 + b_\alpha(x + d_\alpha)^2}{1 + c_\alpha(x + d_\alpha)^2} , \tag{2.33}$$

is taken for $\alpha = \omega, \sigma$. the number of parameters are reduced by constraining the functions as $f_\sigma(1) = f_\omega(1) = 1$, $f'_\sigma(0) = f'_\omega(0) = 0$ and $f_\sigma(1) = f_\omega(1) = 1$, $f''_\sigma(1) = f''_\omega(1)$ [72]. The $\boldsymbol{\rho}_\mu$ coupling decreases at higher densities, therefore, an exponential density-dependence is assumed for the isovector meson ρ [83] i.e.

$$f_\alpha(x) = \exp[-a_\alpha(x - 1). \tag{2.34}$$

These functional dependence is now widely used [84–86]. The saturation density, the mass of σ meson, the couplings $g_{\alpha B}(n_0)$ and the coefficients a_α, b_α, c_α, d_α are found by fitting the finite nuclei properties [72, 73] and are tabulated in Table 2.1. The fit gives the saturation density $n_0 = 0.149065 fm^{-3}$, binding energy per nucleon as -16.02 MeV and incompressibility $K = 242.7$ MeV. The masses of neutron, proton, ω and ρ mesons are 939.56536, 938.27203, 783 and 763 MeV respectively (See Table II of Ref [73]).

Next we determine the hyperon-meson couplings. In the absence of density-dependent Dirac-Brueckner calculation for hyperon couplings, we use scaling factors [70] and nucleon-meson couplings of Table 2.1 to determine the hyperon-meson couplings. The vector coupling constants for hyperons are determined from the SU(6) symmetry [70] as,

$$\begin{aligned} \frac{1}{2}g_{\omega\Sigma} = g_{\omega\Xi} &= \frac{1}{3}g_{\omega N}, \\ \frac{1}{2}g_{\rho\Sigma} = g_{\rho\Xi} = g_{\rho N}; \quad g_{\rho\Lambda} &= 0, \\ 2g_{\phi\Lambda} = g_{\phi\Xi} &= -\frac{2\sqrt{2}}{3}g_{\omega N} \;. \end{aligned} \tag{2.35}$$

The scalar meson (σ) coupling to hyperons is obtained from the potential depth of a hyperon (Y) in the saturated nuclear matter

$$U_Y^N(n_0) = -g_{\sigma Y}\sigma + g_{\omega Y}\omega_0 + \Sigma_N^{(r)}, \tag{2.36}$$

where $\Sigma_N^{(r)}$ involves only the contributions of nucleons. The analysis of energy levels in Λ-hypernuclei suggests a potential well depth of Λ in symmetric matter $U_\Lambda^N(n_0) = -30$ MeV [87, 88]. On the other hand, recent analysis of a few Ξ-hypernuclei events predict a Ξ well depth of $U_\Xi^N(n_0) = -18$ MeV [89, 90]. However, Σ hyperons are ruled out because of the repulsive $\Sigma-$potential depth in nuclear matter. The particular choice of hyperon-nucleon potential does not change the maximum mass of neutron stars [91]. We use these values and find the scaling factor as $R_{\sigma\Lambda} = \frac{g_{\sigma\Lambda}}{g_{\sigma N}} = 0.62008$ and $R_{\sigma\Xi} = \frac{g_{\sigma\Xi}}{g_{\sigma N}} = 0.32097$. We have used this parameters to write the EoS including hyperons that were used to study the core-collapse supernovae and also the structure of the cold neutron stars.

2.4 Nuclear Statistical Equilibrium Model

At low temperature ($< 10MeV$) and sub-saturation density, matter is mainly composed of light and heavy nuclei coexisting with unbound nucleons. Single nucleus approximation (SNA) is used in the most used supernova EoSs of Shen et. al [39] and Lattimer & Swesty [38]. In SNA, whole distribution of different nuclei formed during the core collapse is represented by a single nucleus which is found by minimizing the thermodynamic potential. But, supernova dynamics is sensitive to the treatment of distribution of different nuclei and nuclear clusters. Electron capture rate, neutrino opacities etc. can change, therefore altering the course of evolution. Recent studies on statistical models by Hempel and Schaffner-Bielich [40] take into consideration all these points and propose a multi-component distribution where chemical equilibrium is governed by the extended Saha equation. This is known the Nuclear Statistical Equilibrium model.

The grand canonical partition function is given by,

$$Z(T,V,\{N_i\}) = Z_{nuc} \prod_{A,Z} Z_{A,Z}\, Z_{Coul}\ . \tag{2.37}$$

The Helmholtz free energy which includes the free energies of nucleons, nuclei and Coulomb contribution, can be written [40] as,

$$F(T,V,\{N_i\}) = -T\ln Z = F_{nuc} + \sum_{A,Z} F_{A,Z} + F_{Coul}\ . \tag{2.38}$$

The number density of each species of nuclei is calculated from Maxwell-Boltzmann distribution as [40],

$$n_{A,Z} = \kappa g_{A,Z}(T) \left(\frac{M_{A,Z}T}{2\pi}\right)^{3/2} \exp\left(\frac{(A-Z)\mu_n^0 + Z\mu_p^0 - M_{A,Z} - E^{\mathrm{Coul}}_{A,Z} - P^0_{\mathrm{nuc}}V_{A,Z}}{T}\right), \tag{2.39}$$

where, κ is the volume fraction. Now, the free energy density can be defined as [40],

$$f = \sum_{A,Z} f^0_{A,Z}(T, n_{A,Z}) + f_{Coul}(n_e, n_{A,Z}) + \xi f^0_{nuc}(T, n'_n, n'_p) - T \sum_{A,Z} n_{A,Z} \mathrm{ln}(\kappa) \ . \quad (2.40)$$

This again includes the free energy densities of nucleons, nuclei and Coulomb interactions.

To construct a suitable EoS for supernova simulations, both the EoS tables for high density part and low density part should be combined together with a smooth and continuous transition from one table to the other which is achieved through minimizing the free energy per baryon at fixed temperature, density, electron fraction and minimal hyperon fraction.

CHAPTER 3

ROLE OF HYPERON EQUATIONS OF STATE IN SUPERNOVA SIMULATIONS

3.1 Introduction

The β-equilibrated equations of state that include hyperons were constructed after the discovery of the massive neutron star by several groups. Those hyperon equations of state are found to result in 2 $M_{\odot}$ or heavier neutron stars [86, 91–97]. Besides hyperons, the antikaon condensate was also included in some calculations, which led to massive neutron stars [97]. In all of these calculations, the repulsive hyperon-hyperon interaction that is mediated by ϕ mesons was considered.

Many EoS tables involving hyperons were developed for supernova simulations. The first hyperon EoS table was prepared by [41]. In this case, the full baryon octet was added to the Shen nucleon EoS table [39,41]. The Shen nucleon EoS table was based on a relativistic mean field (RMF) model that had the Thomas-Fermi approximation for the description of inhomogeneous matter below the saturation density [39]. Later, the Shen nucleon EoS was extended to include only Λ hyperons in the HShen Λ EoS table [42]. Another extensively used supernova EoS is the Lattimer and Swesty (LS) nucleon EoS table, which was based on the non-relativistic Skyrme interaction [38]. Recently Λ hyperons were included in the LS nucleon EoS [43]. All these hyperon EoS tables were used in core collapse supernova (CCSN) simulations by several authors [41, 98–101]. However, none of these hyperon EoS tables were consistent with the 2 $M_\odot$ neutron star constraint.

Recently, some new EoS tables have been computed that included Λ hyperons within the framework of the density dependent relativistic hadron (DDRH) field theory by Banik, Hempel and Bandyopadhyay (BHB) [44]. In those EoS tables, light and heavy nuclei, as well as interacting nucleons are described in the nuclear statistical equilibrium model which takes into account the excluded volume effects [40, 44]. Two variants of the hyperon EoS tables were generated - in one case (BHB$\Lambda\phi$), the repulsive Λ hyperon - Λ hyperon interaction mediated by ϕ mesons was considered, and in the other case (BHBΛ), this interaction was neglected. It should be noted that the DDRH model with the DD2 parameter set for nucleons is in very good agreement with the symmetry energy properties at the saturation density [73, 74, 102]. The charge neutrality and β-equilibrium conditions were imposed on the BHB hyperon EoS tables to calculate the mass-radius relationship of the static neutron star sequence. It was observed that the maximum mass corresponding to the BHB$\Lambda\phi$ EoS was 2.1 $M_\odot$ which is well above the recently observed massive neutron star [44]. Other hyperon EoSs for β-equilibrated neutron star matter gave rise to the maximum mass neutron stars of 1.75 $M_\odot$ for the HShen Λ EoS [42], 1.6 $M_\odot$ for Ishizuka EoS [41], 1.91 $M_\odot$ for the LS+Λ EoS [43].

In this work, for the first time, we perform supernova simulations with the BHB$\Lambda\phi$ EoS table, which is compatible with a 2 $M_\odot$ neutron star, in the general relativistic one dimensional (GR1D) hydrodynamics code [103]. Our main goal is to investigate the appearance of Λ hyperons in the postbounce phase and the role of Λ hyperons in CCSNs. Furthermore, we compare our simulation results with those of previous calculations with other hyperon EoS tables, particularly the HShen Λ EoS table [101]. We are looking for important effects of hyperons in CCSN with the BHB$\Lambda\phi$ EoS compared with those of other hyperon EoS.

3.2 Methodology

First we shall discuss the salient feature of the BHB$\Lambda\phi$ and HShen Λ EoS tables for CCSN simulations [42, 44]. The EoS tables are functions of three parameters i.e. baryon number density, temperature, and proton fraction. In both cases, the compositions of matter that vary from one region to the other depending on those parameters are nuclei, (anti)neutrons, (anti)protons, (anti)Λ hyperons, photons plus electrons and positrons that form a uniform background. The contribution of (anti)neutrinos is not added to the EoS tables and is dealt with separately. We describe the baryonic contribution below. After that, we describe briefly about the supernova code GR1D used to study the dynamical evolution of stellar structure.

3.2.1 BHB$\Lambda\phi$ and HShen Λ EoS tables

In the BHB$\Lambda\phi$ EoS table, the nuclear statistical equilibrium (NSE) model of Hempel & Schaffner-Bielich [40] is applied for the description of the matter made of light and heavy nuclei, and unbound nucleons at low temperatures and below the saturation density. In the NSE model, nuclei are treated as a gas of classical particles using Maxwell-Boltzmann statistics. Excluded volume effects as well as medium corrections such as internal excitations or Coulomb screening are taken into account. The dissolution of heavy nuclei at the saturation density is ensured by the excluded volume effects. Unbound nucleons are treated by the DDRH model. The high density matter is described within the framework of the DDRH model adopting the RMF approximation [44, 71, 73]. The repulsive interaction between Λ hyperons mediated by ϕ mesons is included in the RMF model. Nucleon-meson couplings in the DDRH model are density dependent. The DD2 parameter set of nucleon-meson couplings is used to describe the nuclear matter properties [73, 75, 83, 102]. Two BHB Λ hyperon EoS tables with and without ϕ meson were generated using above models [44]. It should be noted that the nuclear EoS in the DDRH model using DD2 parameter set was computed by Hempel and Schaffner (HS) is known as HS(DD2) [75]. Ranges of parameters in this table are baryon density $n_B = 10^{-12}$ to 1.2 fm^{-3}, proton fraction Y_p = 0.01 to 0.6 and temperature T = 0.1 to 158.49 MeV.

On the other hand, the uniform matter at high density and temperature in the HShen Λ EoS table was described within the framework of the RMF model including nonlinear terms in σ and ω mesons [42]; non-uniform matter at low temperatures and below the saturation density was considered as a mixture of alpha particles, heavy nuclei, and unbound nucleons. Heavy nuclei were calculated using the Thomas-Fermi approach. The Shen EoS exploited the single nucleus approximation for heavy nuclei [39, 42]. The interaction among Λ hyperons due to ϕ mesons was neglected in this case. Furthermore, in this case baryon-meson couplings of the RMF model are density-independent. We denote the EoSs with and without Λ hyperons as HShen Λ and HShen, respectively. The parameter set from [104] that is known as the TM1 set was adopted for the nucleon-meson coupling constants of the RMF model.

The nuclear matter saturation properties of two RMF models discussed above are recorded in Table 3.1. It should be noted that though the incompressibility of nuclear matter, symmetry energy, and its slope coefficient of the DD2 set at the saturation density are in very good agreement with experimental values [74,75], the corresponding quantities of the TM1 set are not. This would have serious bearing on the description of high density matter in the RMF model of HShen [42]. For both EoS tables, Λ hyperon-vector meson couplings are estimated from the SU(6) symmetry relations [70, 88] and Λ hyperon - scalar meson coupling is obtained from the hypernuclei data. The Λ hyperon potential depth is -30 MeV in normal nuclear matter [105–107].

The EoSs of β-equilibrated and charge neutral cold neutron star matter with and without Λ hyperons are calculated from the supernova EoS Tables. The maximum masses of cold neutron stars without Λ hyperons for HS(DD2) and HShen EoS are given by Table 3.1. Furthermore, the maximum masses of cold neutron stars corresponding to the BHB$\Lambda\phi$ and HShen Λ are 2.1 $M_\odot$ and 1.75 $M_\odot$ [42, 44], respectively.

For CCSN simulations, we make use of the HS(DD2), BHB$\Lambda\phi$, HShen and HShen Λ EoS tables which are available from the stellarcollapse.org website [1].

Table 3.1: The saturation properties of nuclear matter such as saturation density (n_0), binding energy (BE), incompressibility (K), symmetry energy (S), and slope coefficient of symmetry energy (L) are obtained using the DD2 and TM1 parameter are obtained using the DD2 and TM1 parameter sets. Maximum masses of cold neutron stars without Λ hyperons corresponding to the HS(DD2) and the HShen EoS are also mentioned here [74, 75, 108].

Parameter Set	n_0 (fm^{-3})	BE (MeV)	K (MeV)	S (MeV)	L (MeV)	M_{max} ($M_\odot$)
DD2	0.1491	16.02	243	31.67	55.04	2.42
TM1	0.1455	16.31	281	36.95	110.99	2.18

---

[1] See `http://stellarcollapse.org/equationofstate`

3.2.2 General relativistic model for supernova simulations

We perform the CCSN simulations using the spherically symmetric general relativistic (GR) Eulerian hydrodynamics code GR1D which was developed by O'Connor and Ott in 2010 [103]. In this section, we describe briefly the GR formalism, neutrino schemes and initial progenitor data used in the code. In this code, the hydrodynamical and 3+1 spacetime evolution equations are solved in radial gauge polar slicing coordinate system [109]. The line element is given by,

$$ds^2 = -\alpha(r,t)^2 dt^2 + X(r,t)^2 dr^2 + r^2 d\Omega^2 \ , \tag{3.1}$$

where, $\alpha(r,t)$ and $X(r,t)$ can be expressed in terms of metric potential $\Phi(r,t)$ and enclosed gravitational mass $m(r,t)$,

$$\begin{aligned} \alpha(r,t) &= exp(\Phi(r,t)) \ , && (3.2) \\ X(r,t) &= [1 - 2m(r)/r]^{-1/2} \ . && (3.3) \end{aligned}$$

Ideal hydrodynamics is assumed, and the fluid stress-energy tensor and matter current density are

$$\begin{aligned} T^{\mu\nu} &= \rho h u^\mu u^\nu + g^{\mu\nu} P \ , && (3.4) \\ J^\mu &= \rho u^\mu \ , && (3.5) \end{aligned}$$

where ρ is the matter density, P is the Fluid pressure, $h = 1 + \epsilon + P/\rho$ is the specific enthalpy, ϵ the internal energy, u^μ is the 4-velocity of the Fluid. In 1D, u^μ is equal to $(\Gamma/\alpha, \Gamma v^r, 0, 0)$, where $\Gamma = (1 - v^2)^{-1/2}$ is the Lorentz boost factor and $v = X v^r$.

For the Hamiltonian constraint and the momentum constraint equations [109, 110], we get the expressions for $m(r,t)$ and $\Phi(r,t)$,

$$\begin{aligned} m(r,t) &= 4\pi \int_0^r (\rho h \Gamma^2 - P + \tau_m^\nu) r'^2 dr' && (3.6) \\ \Phi(r,t) &= \int_0^r X^2 \left[\frac{m(r',t)}{r'^2} + 4\pi r' (\rho h \Gamma^2 v^2 + P + \tau_\Phi^\nu) \right] dr' + \Phi_0 \, . && (3.7) \end{aligned}$$

Here, the effects of trapped neutrinos are included in τ_m^ν, τ_Φ^ν terms.

Fluid evolution equations are derived from local conservation laws

$$\nabla_\mu T^{\mu\nu} = 0, \qquad \nabla_\mu J^\mu = 0 \tag{3.8}$$

In this code, the flux-conservative Valencia formulation modified for spherically symmetric flows is used [111, 112]. The evolution equations becomes,

$$\partial_t \vec{U} + \frac{1}{r^2} \partial_r \left[\frac{\alpha r^2}{X} \vec{F} \right] = \vec{\mathcal{S}} \, . \tag{3.9}$$

Here, $\vec{U} = [D, DY_e, S^r, \tau]$ are conserved variables which are functions of primitive variables ρ, Y_e, ϵ, v, and P.

$$\vec{U} = \begin{pmatrix} D \\ DY_e \\ S^r \\ \tau \end{pmatrix} = \begin{pmatrix} X\rho\Gamma \\ X\rho\Gamma Y_e \\ \rho h \Gamma^2 v \\ \rho h \Gamma^2 - P - D \end{pmatrix} . \tag{3.10}$$

$\vec{F}$ is the flux vector.

$$\vec{F} = (Dv,\ DY_e v,\ S^r v + P,\ S^r - Dv) \, , \tag{3.11}$$

$\vec{\mathcal{S}}$ is the source terms containing all the gravitational and matter interaction sources.

$$\begin{aligned}\vec{\mathcal{S}} = \ & \Big[0,\ R^{\nu}_{Y_e},\ (S^r v - \tau - D)\alpha X \left(8\pi r P + \tfrac{m}{r^2}\right) + \alpha P X \tfrac{m}{r^2} \\ & + \tfrac{2\alpha P}{Xr} + Q^{\nu,\mathrm{E}}_{S^r} + Q^{\nu,\mathrm{M}}_{S^r},\ Q^{\nu,\mathrm{E}}_{\tau} + Q^{\nu,\mathrm{M}}_{\tau}\Big], \end{aligned} \tag{3.12}$$

Here, the neutrino source and sink term are denoted by the Rs and Qs [103]. This system of equations is solved by finite volume method and integrations are done by method of lines using standard Runge-Kutta integrator.

Microphysical EoS for supernova matter is required to close the GR hydrodynamic system of equations. We use the BHB$\Lambda\phi$ and HShen Λ EoS tables, as explained in the previous section, in CCSN simulations with the GR1D code.

In chapter 1, we discussed how crucial the neutrino treatment is for a successful supernova explosion. In principle, it should be included in the simulation framework via GR Boltzmann transport which is computationally expensive. Since, the aim of the GR1D code to study the parameter spaces with huge number of simulations, an approximate treatment of neutrinos in the pre- and postbounce phases are implemented for faster simulations.

In the pre-bounce phase, GR1D uses the fact that electron fraction Y_e can be effectively parametrized as a function of density [113]. However, in the post bounce phase this simple parametrization leads to inaccurate results due to multiple effects of deleptonization, neutrino cooling and heating. So, a three-flavour, energy averaged neutrino leakage scheme is used to capture those effects [114,115]. In this model, three neutrino species are considered which are denoted by ν_e, $\bar{\nu}_e$, $\nu_x (= \nu_\mu, \bar{\nu}_\mu, \nu_\tau, \bar{\nu}_\tau)$ [103,116]. The leakage scheme exploited in the GR1D code gives approximate number and energy emission rates. To mimic a explosion in the 1D spherically symmetric model, an artificial neutrino heating in the post shock region is considered here. It involves a parametrized charge current scheme [117].

The local neutrino heating rate is given by,

$$Q^{heat}_{\nu_i}(r) = f_{heat}\frac{L_{\nu_i}(r)}{4\pi r^2}\sigma_{heat,\nu_i}\frac{\rho}{m_u}X_i\left\langle\frac{1}{F_{\nu_i}}\right\rangle e^{-2\tau_{\nu_i}} \ . \tag{3.13}$$

Here, the scale factor f_{heat} could be enhanced beyond the normal value of 1 to achieve additional neutrino heating for ”successful” CCSN explosions [116]. We take $f_{heat} = 1$ in CCSN simulations, if not stated otherwise. It has been noted that the results obtained in CCSN simulations using the simplified treatment of neutrino leakage and heating in the GR1D were quantitatively similar to the results obtained from one dimensional (1D) simulations with the Boltzmann neutrino transport by other groups [118, 119]. It was argued that progenitor structures played more important roles in the collapse of a protoneutron star (PNS) to a black hole than the details of neutrino treatment [116].

In our studies, nonrotating progenitors of Woosley and Heger (WH07) [120] are used. In their stellar evolution studies [120] evolved zero age main-sequence (ZAMS) stars with solar metallicity denoted by the prefix s before presupernova models, followed by ZAMS mass. Significant mass loss was reported in sWH07 presupernova models [116].

3.3 Results and Discussion

Now, we present our investigations on CCSNs within the GR1D code using the HShen Λ hyperon and BHB$\Lambda\phi$ EoS tables.

We perform the CCSN simulations with presupernova models as recorded in Table 3.2. In all numerical calculations, we fix the neutrino heating factor $f_{heat} = 1$. In the next paragraphs, we discuss the results of simulations starting from the gravitational collapse of the iron core followed by the core bounce to the postbounce evolution of the PNS for

$s40$WH07 and $s23$WH07 models with the HShen Λ and BHB$\Lambda\phi$ EoS tables in details. In all of these simulations, a shock wave is launched at the core bounce, it stalls after traversing a few 100 km, then recedes and becomes an accretion shock. Because neutrinos in the 1D CCSN model could not revive the shock, the PNS shrinks due to mass accretion and its density and temperature increase during the postbounce evolution. This leads to the appearance of Λ hyperons in the PNS.

Table 3.2: Black hole formation time, baryonic and gravitational masses of PNSs for CCSN simulations with the progenitor models of [120] and the BHB$\Lambda\phi$ and HShen Λ EoS tables [108].

Model	BHB$\Lambda\phi$			HShen Λ		
	t_{BH} (s)	$M_{b,max}$ $(M_\odot)$	$M_{g,max}$ $(M_\odot)$	t_{BH} (s)	$M_{b,max}$ $(M_\odot)$	$M_{g,max}$ $(M_\odot)$
$s20$WH07	1.938	2.251	2.138	1.652	1.999	1.964
$s23$WH07	0.879	2.276	2.203	0.847	2.095	2.073
$s25$WH07	1.548	2.234	2.141	1.376	2.035	2.001
$s30$WH07	2.942	2.243	2.113	2.258	1.967	1.929
$s35$WH07	1.175	2.243	2.161	1.084	2.071	2.041
$s40$WH07	0.555	2.250	2.210	0.565	2.129	2.118

For $s40$WH07, the core bounce occurs at 0.273 and 0.321 s, corresponding to the HShen Λ hyperon and BHB$\Lambda\phi$ EoS, respectively. Similarly, in the $s23$WH07 model the core bounce times for the HShen Λ and the BHB$\Lambda\phi$ EoS are 0.266 and 0.315 s, respectively. The appearance of strangeness or Λ hyperons in the postbounce phase and its role in the evolution of the PNS are the main focuses of this investigation. For $s40$WH07 and $s23$WH07 models and both hyperon EoS tables, Λ hyperons do not populate the PNS at the core bounce. In simulations with both presupernova models, strangeness in the form of Λ hyperons sets in a few hundred milliseconds (ms) after the core bounce and increases with time thereafter.

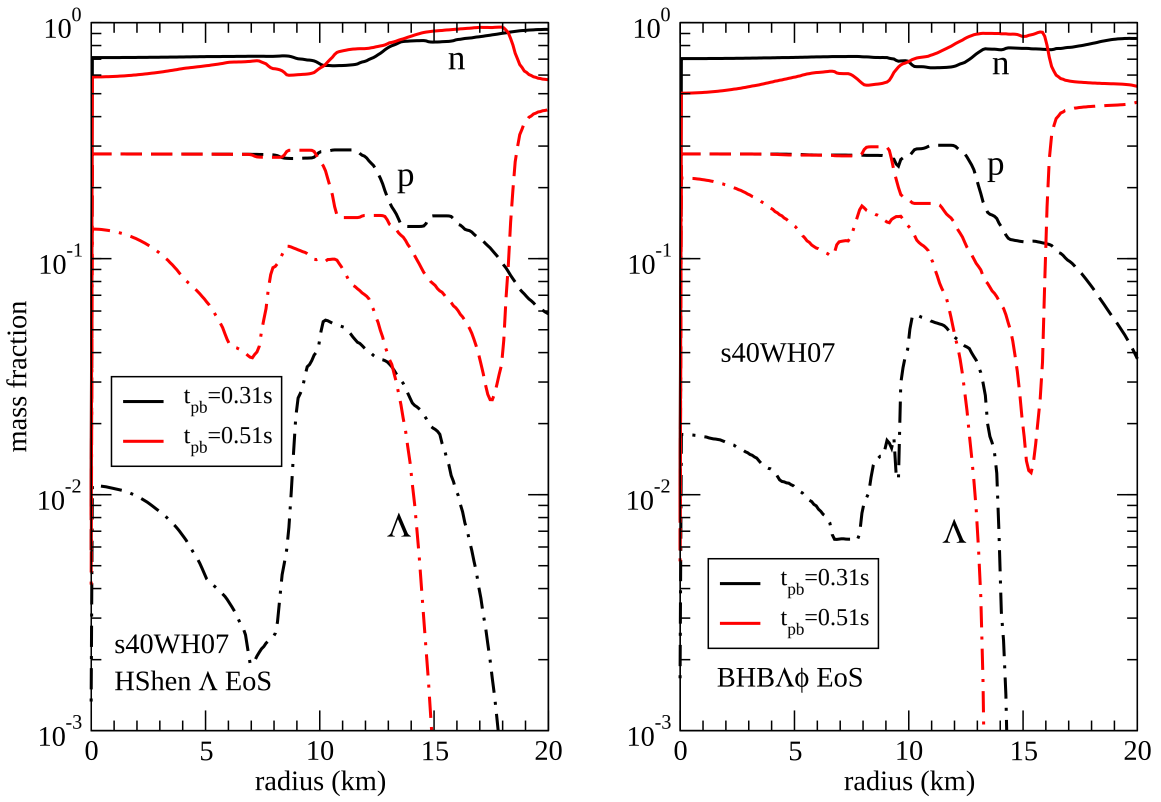

Figure 3.1: Mass fractions of different species in the PNS are shown as a function of radius for the HShen Λ EoS (left panel) and the BHBΛϕ EoS (right panel) at $t_{pb} = 0.31$ and 0.51 s. The results in both panels correspond to the $s40$WH07 model [108].

Figure 3.1 depicts the PNS compositions as a function of radius at two different post-bounce times for $s40$WH07 with the HShen Λ (left panel) and BHB$\Lambda\phi$ (right panel) EoS tables. For postbounce time (t_{pb}) 0.31 s, the central value of Λ fraction is higher for the BHB$\Lambda\phi$ EoS than that of the HShen Λ hyperon EoS. The profile of Λ hyperons is wider in the latter case. We find similar trends for Λ hyperons at a later time $t_{pb} = 0.51$ s. For both EoS tables, the population of Λs increases with time. It is to be noted that the central value of the Λ fraction is a high density effect, whereas the off-center Λs are populated thermally. We study the density and temperature profiles to understand this behaviour.

The density profiles as a function of radius are plotted for $s40$HW07 at the bounce as

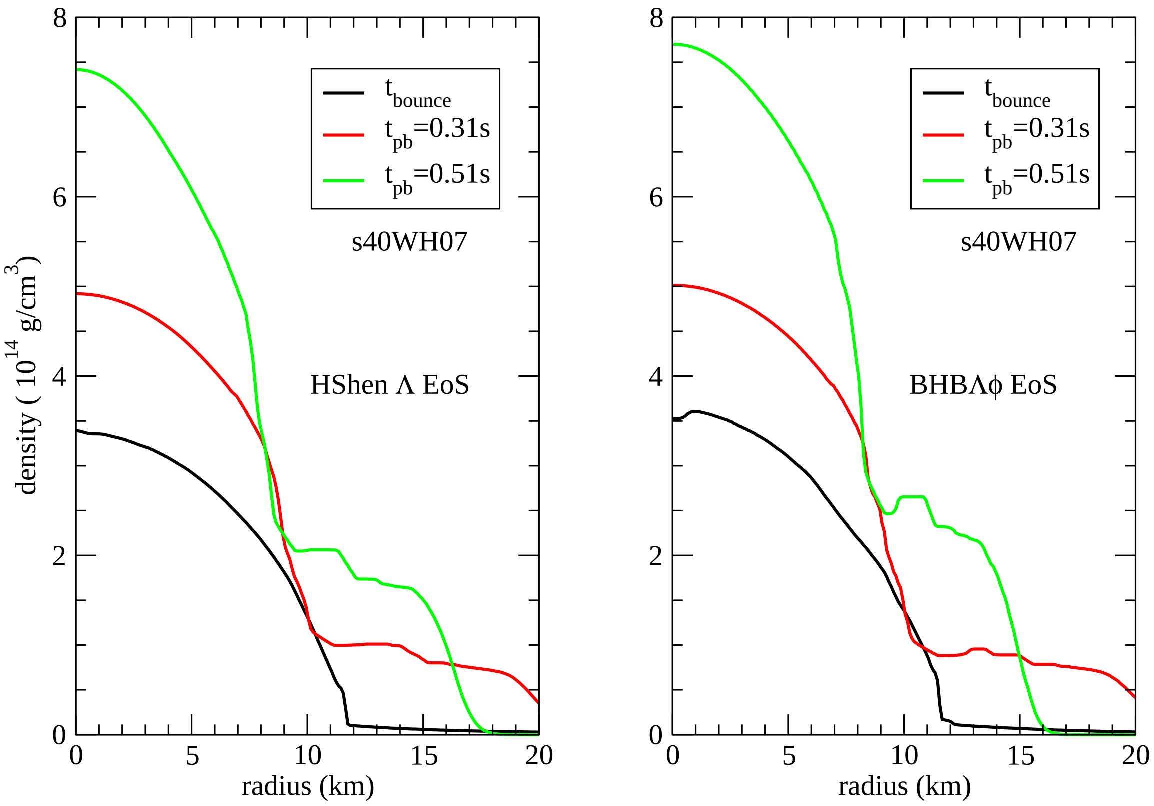

Figure 3.2: Density profiles of the PNS are shown as a function of radius for the HShen Λ EoS (left panel) and the BHB$\Lambda\phi$ EoS (right panel) at the core bounce and $t_{pb} = 0.31$ and 0.51 s. The results in both panels correspond to the s40WH07 model [108].

well as for $t_{pb} = 0.31$ and 0.51 s in Figure 3.2. The left panel of the figure corresponds to the HShen Λ EoS and the right panel implies the results of the BHB$\Lambda\phi$ EoS. At the bounce, the central density (ρ_c) of the PNS in both cases is just above the normal nuclear matter density, as evident by the figure. Though the density profiles for both EoS tables are quantitatively the same at $t_{pb} = 0$, they differ at later times. The central density at $t_{pb} =$ 0.51 in the right panel is higher than that of the left panel. In both cases, the central density exceeds two times the normal nuclear matter density. This high central density facilitates a significant population of Λs in the core of the PNS, as seen in Fig. 1. However, the density falls well below normal nuclear matter density at the tail of the profile. The off-center Λs

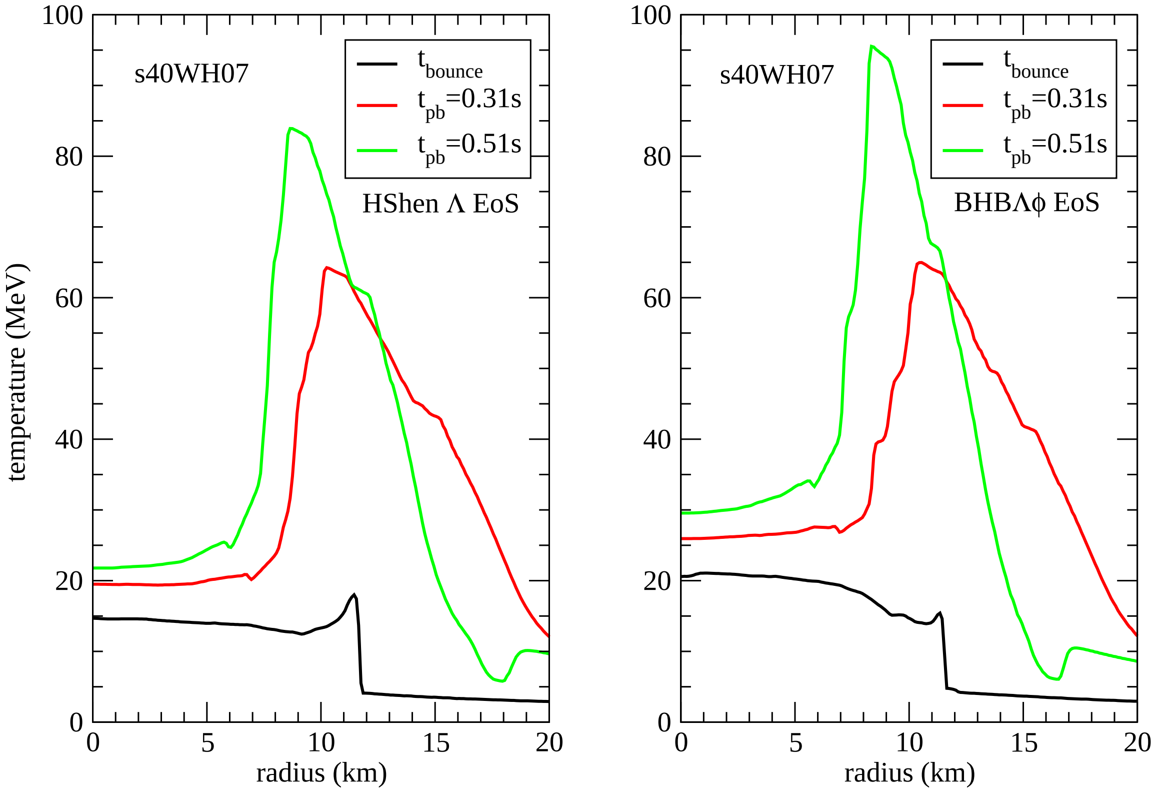

Figure 3.3: Temperature profiles of the PNS are shown as a function of radius for the HShen Λ EoS (left panel) and the BHB$\Lambda\phi$ EoS (right panel) at the core bounce and t_{pb} = 0.31 and 0.51 s. The results in both panels correspond to the s40WH07 model [108].

in Figure 3.1 could not be attributed to the density effect.

The temperature profiles as a function of radius are shown for s40WH07, with the HShen Λ hyperon (left panel) and the BHB$\Lambda\phi$ (right panel) EoS tables in Figure 3.3. Just as in Figure 3.2, the temperatures profiles are plotted at the core bounce and t_{pb} = 0.31 and 0.51 s in both panels of Figure 3.3. The peaks of temperature profiles located away from the center of the PNS for both EoSs after the core bounce later shift toward the center with time in both panels. It is to be noted that the central temperature at the bounce is higher for the BHB$\Lambda\phi$ EoS compared with the corresponding temperature for the HShen Λ EoS. Furthermore, the peak temperature around 8 km at 0.51 s after core bounce in the case of

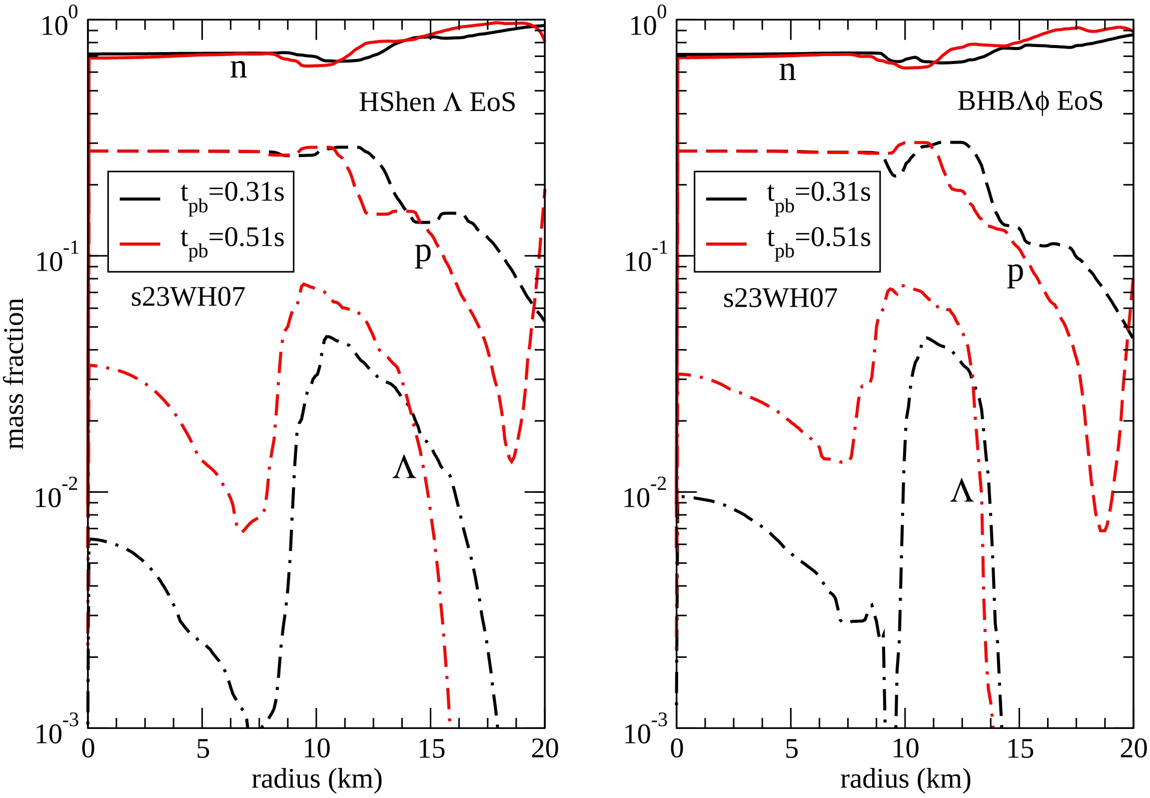

Figure 3.4: Same as Figure 3.1 but for the s23WH07 model. The results correspond to the HShen Λ EoS (left panel) and the BHB$\Lambda\phi$ EoS (right panel) at $t_{pb} = 0.31$ and 0.51 s [108].

the BHB$\Lambda\phi$ EOS is much higher than the corresponding scenario for the HShen Λ EoS. This high temperature results in thermally produced Λ hyperons away from the centre of the PNS as shown in Figure 3.1. We find from Figure 3.1 that thermal Λs are more abundant around 8 km at later times for the BHB$\Lambda\phi$ EoS due to a higher peak temperature.

We also study profiles of particle fraction, density, and temperature for s23WH07 using both hyperon EoS tables as shown in Figures 3.4, 3.5 and 3.6. We obtain qualitatively similar results for s23WH07 as we have already discussed for s40WH07.

Now we focus on the postbounce evolution of the PNS for different presupernova models with nuclear and Λ hyperon EoS tables corresponding to the HShen and BHB models. Figure 3.7 exhibits the evolution of the central density of the PNS with the postbounce

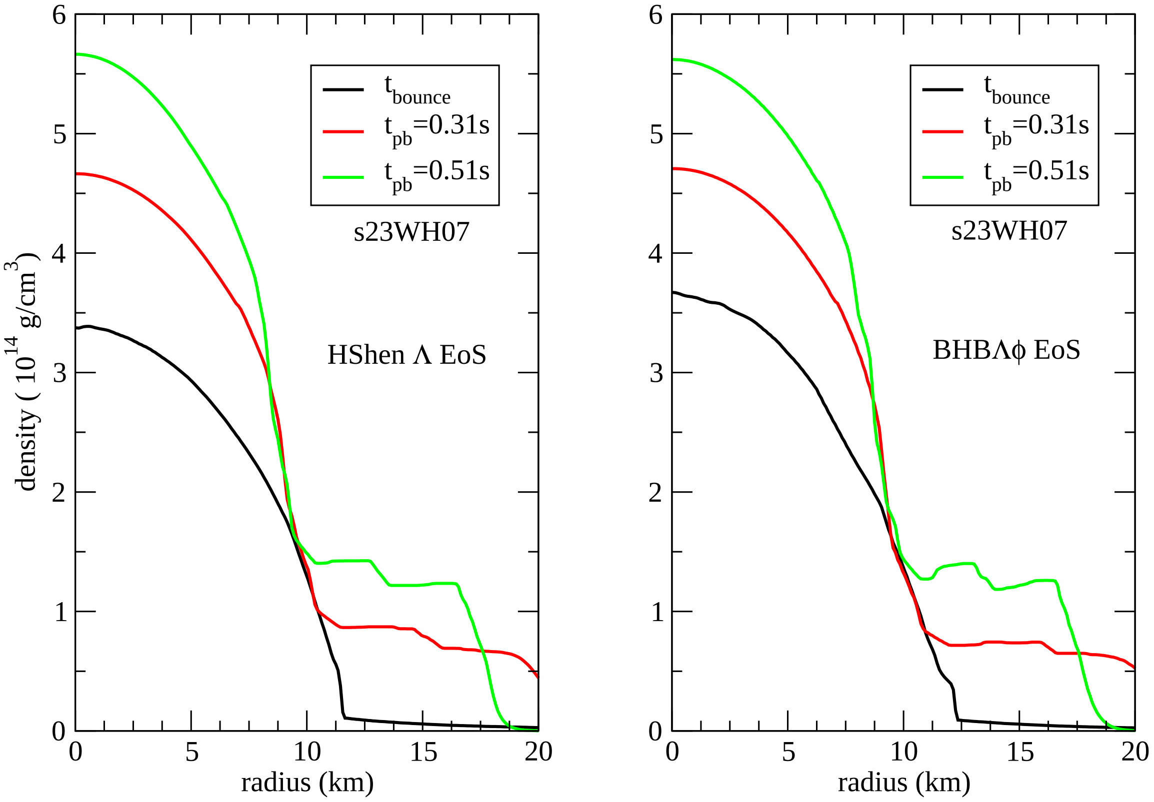

Figure 3.5: Same as Figure 3.2 but for the s23WH07 model. The results correspond to the HShen Λ EoS (left panel) and the BHB$\Lambda\phi$ EoS (right panel) at the core bounce and t_{pb} = 0.31 and 0.51 s [108].

times for s40WH07 (left panel) and s23WH07 (right panel). Results are shown in both panels for the HShen nuclear EoS, the HShen Λ EoS, the HS(DD2) nuclear EoS and the BHB$\Lambda\phi$ EoS. It should be noted that the core bounce time for the hyperon EoS is the same as that of the corresponding nuclear EoS.

In all cases in both panels of Figure 3.7, we find that the central density increases gradually to several times the normal nuclear matter density. Finally, there is a steep rise in the central density when the PNS dynamically collapses into a black hole in milliseconds. It should be noted that the black hole formation time is different for different EoS models. It is evident from the CCSN simulation of s23WH07 that the black holes are formed at

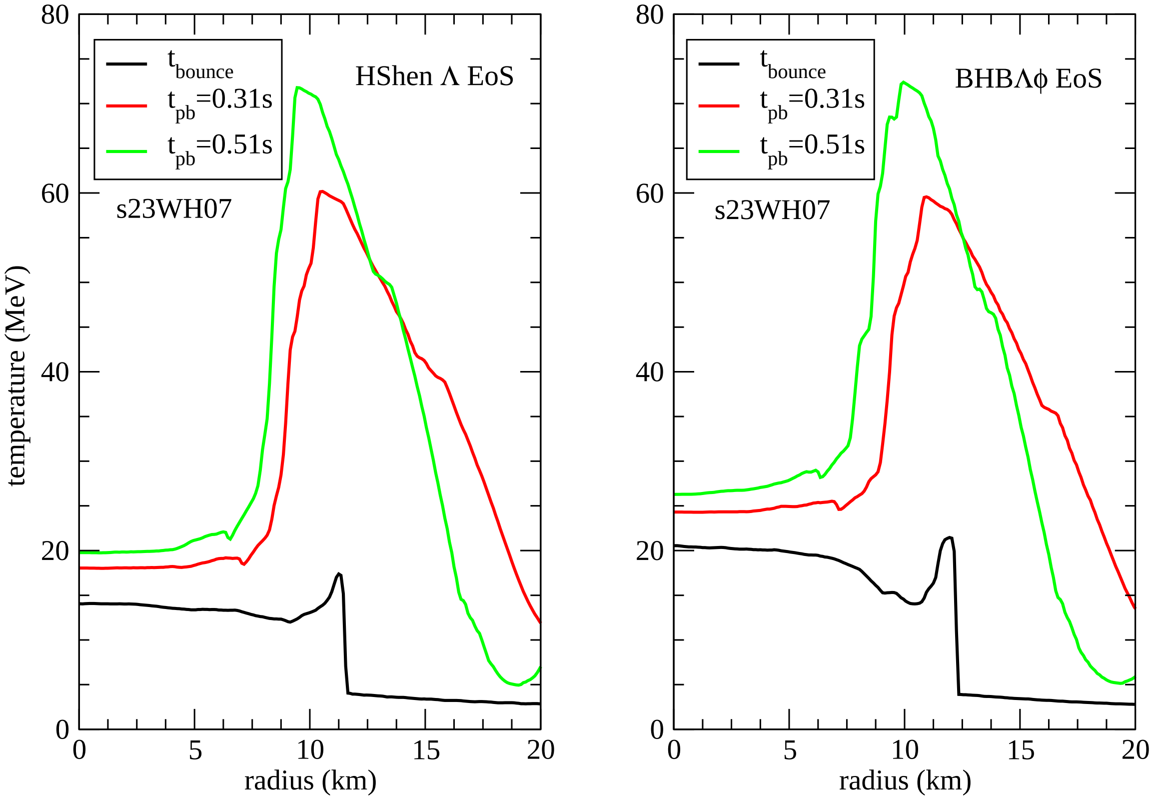

Figure 3.6: Same as Figure 3.3 but for the s23WH07 model. The results correspond to the HShen Λ EoS (left panel) and the BHB$\Lambda\phi$ EoS (right panel) at the core bounce and $t_{pb} =$ 0.31 and 0.51 s [108].

1.511 and 1.623 s after the core bounce for the HS(DD2) and the HShen EoS, respectively. For s40WH07, the black hole formation time is 0.942 s in the case of the HS(DD2) EoS, whereas it is 1.084 s for the HShen EoS. For both supernova models and nuclear EoS tables, the black hole is formed earlier in case of the HS(DD2) than the situation with the HShen EoS. The maximum gravitational (baryonic) PNS masses are 2.464 (2.616) $M_\odot$ and 2.459 (2.587) $M_\odot$ for s40SW07 with the HS(DD2) and the HShen EoS, respectively. Similarly, for s23WH07, those are 2.428 (2.605) $M_\odot$ and 2.383 (2.512) $M_\odot$ corresponding to the HS(DD2) and the HShen EoS. On the other hand, the dynamical collapse to a black hole is accelerated for the HShen Λ and BHB$\Lambda\phi$ EoS tables because hyperons make the

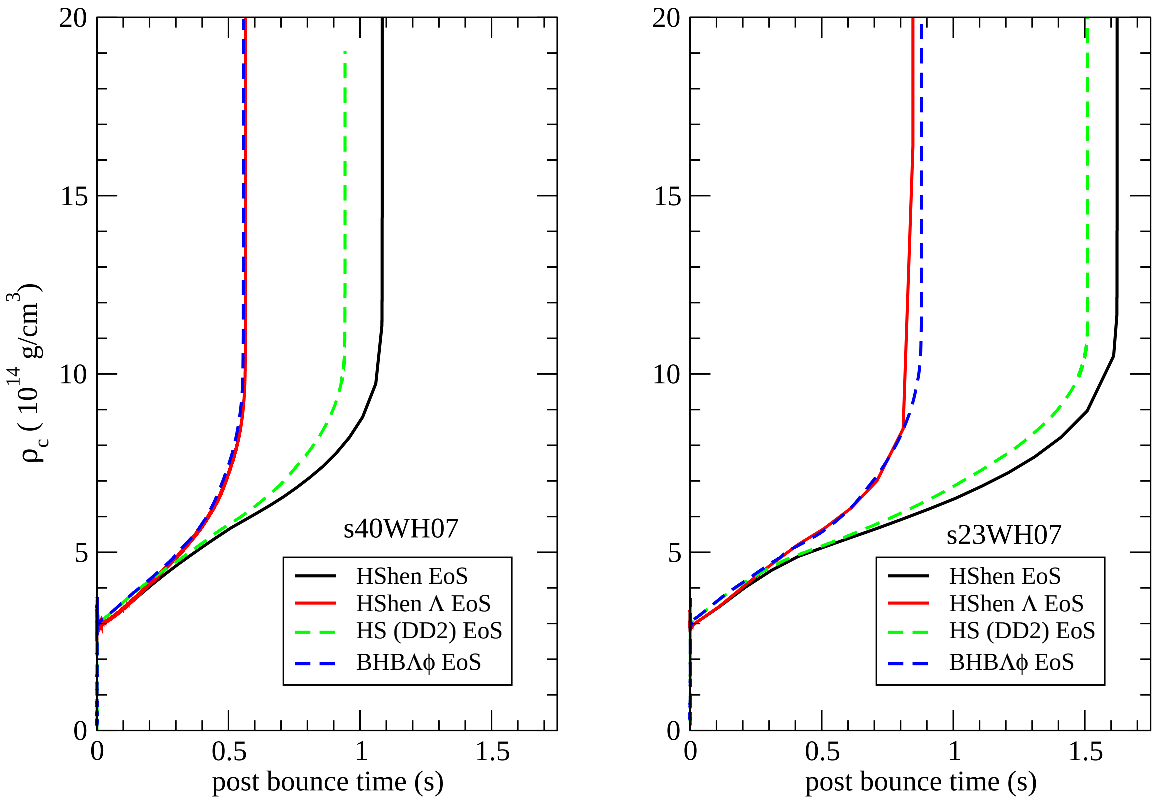

Figure 3.7: Central baryon density is plotted with the postbounce time for the HShen nuclear EoS, the HShen Λ EoS, the HS(DD2) and the BHB$\Lambda\phi$ EoS . The results in the left and right panels correspond to the s40WH07 and s23WH07 models [108].

EoS softer. It is evident from Figure 3.7 that the black hole formation time is shorter for hyperon EoS than that for the corresponding nuclear EoS. However, there is little difference between the black hole formation times corresponding to the HShen Λ and BHB$\Lambda\phi$ EoSs.

The results of CCSN simulations with other presupernova models are recorded in Table 3.2. The first column of the table lists the presupernova models of Ref. [120] starting from s20WH07 to s40WH07. Two EoS tables, such as the HShen Λ and the BHB$\Lambda\phi$ are adopted in these calculations. Under each EoS, the first column represents the black hole formation time (t_{BH}) estimated from the core bounce and the next column gives the maximum baryon mass (M$_{b,max}$) followed by the maximum gravitational mass (M$_{g,max}$) of the PNS at the point of instability corresponding to the central value of the lapse function 0.3. Further investigations with the two Λ hyperon EoSs reveal an opposite behaviour of t_{BH} than what has been observed for nuclear EoSs. For Λ hyperon EoS, t_{BH} for the BHB$\Lambda\phi$ is always greater than that of the HShen Λ for all presupernova models except s40WH07. The comparison of two hyperon EoSs shows that the BHB$\Lambda\phi$ is a stiffer EoS than the HShen Λ. The explanation of this behaviour may be traced back to the inclusion of repulsive Λ-Λ interaction in the BHB$\Lambda\phi$ EoS. For all presupernova models and EoSs adopted in simulations, it is evident from the table that the maximum gravitational mass of the PNSs in each case is higher than their corresponding maximum cold neutron star masses. However, in some cases, the maximum gravitational mass of the PNS collapsing into a black hole with the HShen Λ EoS is less than the two solar mass limit because the HShen Λ EoS does not result in a 2 $M_{\odot}$ cold neutron star. It is interesting to note that in the case of the HShen Λ EoS, the difference between $M_{g,max}$ of the PNS and the maximum mass of the cold neutron star that includes Λ hyperons (1.75 $M_{\odot}$) is appreciable, whereas the maximum gravitational mass of the PNS for the BHB$\Lambda\phi$ EoS is very similar to the value of the corresponding maximum mass of the cold neutron star with Λs (2.1 $M_{\odot}$) for the entire set of progenitor models. This shows that the thermal effects in the PNS for the BHBH$\Lambda\phi$ might not be as strong as in the PNS with the HShen Λ because the EoS is stiffer in the former case. The role of decreasing thermal pressure with increasing stiffness of the EoS was already noted by Ref. [116]. This should have interesting implications for the study of the metastability of the PNS with the BHB$\Lambda\phi$ EoS.

We compare our findings with other CCSN simulations with hyperon EoS. The Ishizuka hyperon EoS includes Λ, Σ, and Ξ hyperons and is an extension of the HShen nuclear EoS [41]. The CCSN simulations were performed in a spherically symmetric general relativistic neutrino radiation hydrodynamics model using a 40 $M_{\odot}$ progenitor of [15] and the Ishizuka

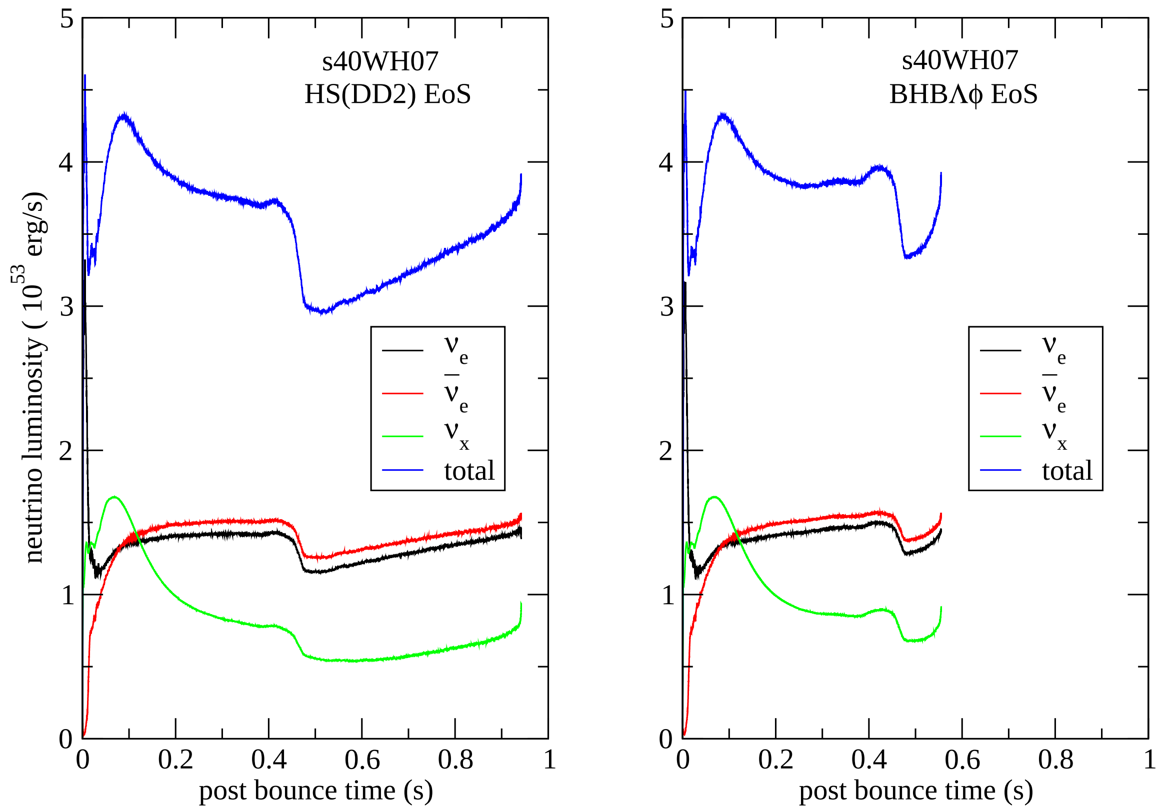

Figure 3.8: Total neutrino luminosity as well as ν_e, $\bar{\nu}_e$ and ν_x luminosities are plotted with the postbounce time for the HS(DD2) (left panel) and the BHBΛϕ (right panel) EoS. The results correspond to the s40WH07 model [108].

hyperon EoS [99, 100]. With the LS+Λ EoS [43] Peres et al. [121] carried out a similar investigation using an s40WW progenitor and a low metallicity 40 M$_\odot$ progenitor of Ref. [16] called u40. Banik (2014) [101] also studied CCSN simulations using the HShen Λ EoS and progenitor models of Ref. [120], particularly studying the long duration evolution of the PNS in the context of understanding the fate of the compact object in SN1987A. It should be noted that though our results with the BHBΛϕ EoS are qualitatively similar to those of earlier calculations, they are quantitatively different because only our Λ hyperon EoS is compatible with the 2 M$_\odot$ limit of cold neutron stars. The early black hole formation due to softening in the Λ hyperon EoS compared with the nuclear EoS is a robust conclusion

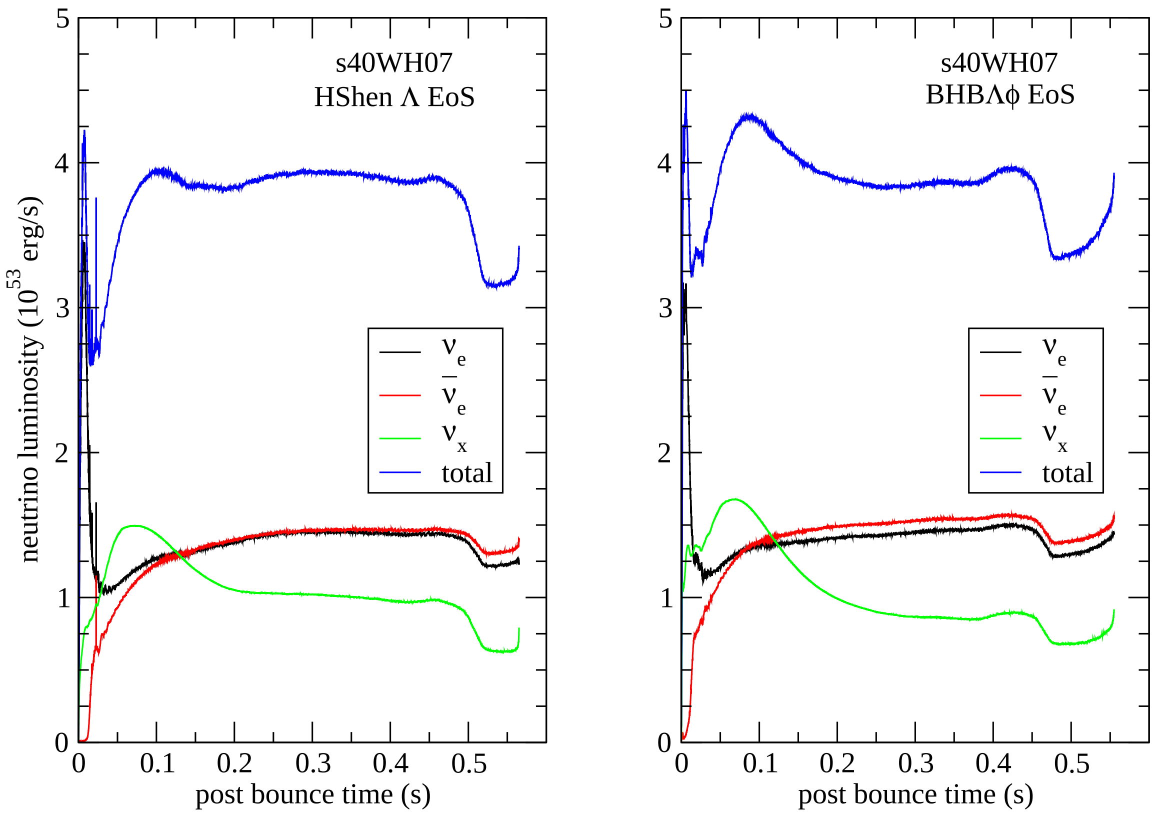

Figure 3.9: Total neutrino luminosity as well as ν_e, $\bar{\nu}_e$ and ν_x luminosities are plotted with the postbounce time for the HShen Λ (left panel) and the BHBΛϕ (right panel) EoS. The results correspond to the s40WH07 model [108].

in all of these calculations.

In this study, we have ignored the hyperon-neutrino interaction, as Peres. et al [121] have shown that neutrino scattering off hyperon may not be a significant factor in the evolution of the PNS. Total neutrino luminosity as well as ν_e, $\bar{\nu}_e$, and ν_x luminosities as a function of postbounce time are plotted in Figure 3.8 for the HS(DD2) (left panel) and the BHBΛϕ (right panel) EoS. The results are shown here for the s40WH07 model. It should be noted that the neutrino emission ceases earlier for the BHBΛϕ case than for the scenario with the HS(DD2) nuclear EoS. A similar conclusion was arrived at in the simulation with other hyperon EoSs [100, 101]. The shorter neutrino burst corresponding to the Λ hyperon

EoS before the collapse of the PNS into the black hole could be an important probe for the appearance of Λ hyperons in the PNS. This demands a more accurate treatment of neutrinos in the GR1D code.

Figure 3.9 exhibits the neutrino luminosities for both the Λ hyperon EoS and the s40WH07 model. We find similar features for neutrino luminosities for both cases. Though we are considering a phase transition from nuclear to Λ hyperon matter, we do not find any evidence for a second neutrino burst, which was observed in a first order quark-hadron phase and was responsible for a successful supernova explosion [45].

So far we have seen that simulations in the 1D CCSN model might lead to accretion driven black holes in failed supernovae. If a successful supernova occurs, can exotic matter such as hyperons make the PNS metastable and drive it to become a low mass black hole during the long duration evolution when thermal support decreases and deleptonization takes place in the PNS? Such a scenario was envisaged for the non-observation of a compact object in SN1987A [46, 122, 123]. This problem was also studied in CCSN simulations [101, 124, 125].

We continue our study by increasing the neutrino heating scale factor to $f_{heat} = 1.5$ for s20WH07 with the BHB$\Lambda\phi$ EoS. The left panel of Figure 10 exhibits the shock radius as a function of postbounce time. For the neutrino scale factor $f_{heat} = 1$, it fails to launch a successful supernova explosion and the shock radius recedes. Finally, the PNS collapses into a black hole. For $f_{heat} = 1.5$, it is observed that the shock radius increases with time after a successful supernova explosion. The PNS remains stable until 4 s. We do not find any onset of the metastability in the PNS due to the loss of thermal support and neutrino pressure during the cooling phase over a few seconds. The window for the metastability is very narrow because the maximum PNS mass in this case is 2.138 $M_{\odot}$ whereas the maximum cold neutron star mass corresponding to the BHB$\Lambda\phi$ EoS is 2.1 $M_{\odot}$. The PNS

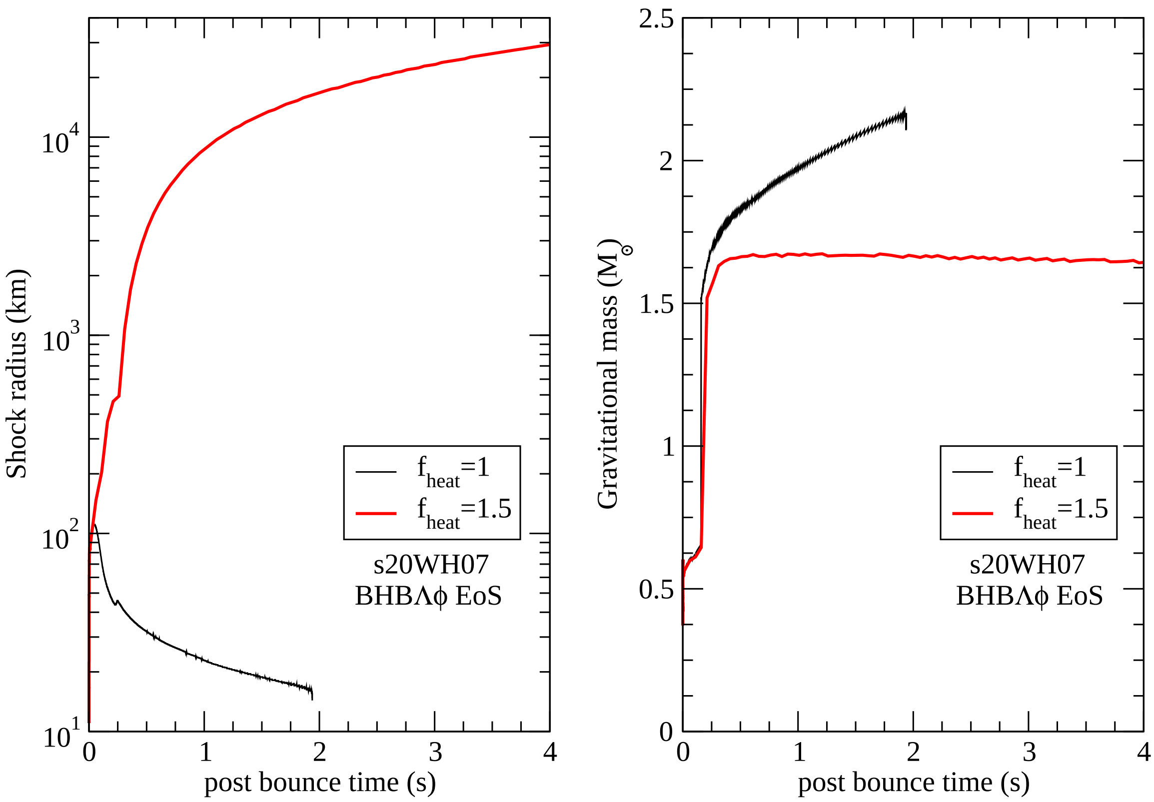

Figure 3.10: Shock radius (left panel) and gravitational mass of the PNS (right panel) are plotted with the postbounce time using the neutrino heating factor $f_{heat} = 1$ and 1.5 for the s20WH07 model and the BHB$\Lambda\phi$ EoS [108].

might evolve into a cold neutron star. Gravitational masses of the PNS for $f_{heat} = 1$ and 1.5 are shown as a function of postbounce time in the right panel of Figure 3.10. The PNS cools down to a neutron star with a mass ~ 1.64 M$_\odot$ at the end of 4 s.

3.4 Summary and Conclusions

We have performed CCSN simulations using the BHB$\Lambda\phi$ EoS, which is compatible with a 2 M$_\odot$ neutron star, and several progenitor models from the stellar studies of Ref. [120]. It is observed that Λs are produced a few hundred milliseconds after the core bounce.

The appearance of Λ hyperons is studied in great detail. It is evident from the density and temperature profiles as a function of radius that Λs are produced in the core of the PNS when the central density exceeds two times the normal nuclear matter density during the postbounce evolution phase. On the other hand, an off-center population of thermal Λ hyperons is the result of peak values of temperature away from the center of the PNS. When we set the neutrino heating scale factor $f_{heat} = 1$, each CCSN simulation ends with the formation of a black hole driven by mass accretion. It is interesting to find out that the black hole formation time for the BHB$\Lambda\phi$ EoS is shorter than that of the HShen Λ EoS though the opposite conclusion is drawn from the accretion driven black hole with the HShen nuclear and HS(DD2) EoS models. This is attributed to the fact that the repulsive Λ-Λ interaction in the BHB$\Lambda\phi$ EoS makes it a stiffer EoS than the HShen Λ EoS. Neutrino luminosity is found to cease with the formation of a black hole earlier for the Λ hyperon EoS than for the corresponding case with the nuclear EoS. We have studied the metastability of the PNS due to the BHB$\Lambda\phi$ EoS in the long duration evolution after a successful supernova explosion using the s20WH07 progenitor model with the increased neutrino heating scale factor of $f_{heat} =$ 1.5. In this case, we do not find any delayed collapse into the black hole due to the presence of Λ hyperons in the PNS. The PNS that has a mass ~ 1.64 M$_{\odot}$ remains stable until 4 s and might become a cold neutron star.

CHAPTER 4

EFFECTS OF EXOTIC MATTER ON NEUTRON STAR STRUCTURE

4.1 Introduction

It is still an open issue if novel phases of matter such as hyperons, Bose-Einstein condensates of pions and kaons and also quarks may exist in neutron star interior or not. The presence of hyperons and antikaon condensates makes the EoS softer resulting in a smaller maximum mass neutron star than that of the nuclear EoS [126, 127]. In fact strangeness in the high-density baryonic matter is almost the inevitable consequence of Pauli principle. Strange degrees of freedom would be crucial for long time evolution of the PNS [101] also. The observation of massive compact stars with mass $> 2M_\odot$ puts stringent constraint on the model of neutron stars and may abandon most of the soft EoS. However, it is at present not possible to rule out all exotica with recent observation as many model calculations including hyperons and/or quark matter could still be compatible with the observations. Many of these approaches are parameter dependent, for example the EoS with hyperons are compatible with the benchmark of $2M_\odot$ [86,92,93,121,128,129]. Antikaon condensate is another possible strange candidate in the dense interior of neutron stars. It was first demonstrated by Kaplan and Nelson within a chiral $SU(3)_L \times SU(3)_R$ model in dense matter formed in heavy ion collisions [130]. The isospin doublet for kaons is $K \equiv (K^+, K^0)$ and that for antikaons $\bar{K} \equiv (K^-, \bar{K}^0)$. The attractive interaction in nuclear matter reduces the in-medium energy of (anti)kaons; which at higher density eventually falls below the chemical potential of the leptons and electrons are replaced. Antikaon condensation was later studied in details in the context of cold neutron star and protoneutron star [123, 127, 131] in the RMF model, also in the density dependent RMF model [71]. The net effect of K^- condensates in neutron star matter is to maintain charge neutrality replacing electrons and to soften the EoS resulting in the reduction of maximum mass of the neutron star [71,123], which was found to be within the observational limit. Also the threshold of (anti)kaon condensation is sensitive to antikaon optical potential and presence of charged hyperons pushes the threshold to higher densities. In a recent study both the approaches, density dependent couplings and higher order couplings, in presence of (anti)kaon condensates have been compared [132]. All the parameter sets were found to produce $2M_\odot$ neutron stars without antikaon condensate and some with antikaon condensate, but hyperons were not included in that study.

We investigate the possibility of antikaon condensation in beta equilibrated hyperon matter relevant to the dense interior of compact stars. Here we work with less to moderately attractive antikaon optical potential depth. We also use ϕ-meson for hyperonic and kaonic interaction. Antikaon condensation in the presence of hyperon with additional ϕ-meson has been studied previously [71], but not in the realistic density dependent framework. In this work we are interested to explore in a density dependent model whether this softening of EoS that arises due to both antikaon condensation and hyperon, can still produce a $2M_\odot$ neutron star within the observational limit.

4.2 Formalism

A phase transition from hadronic to antikaon condensed matter is considered here. This phase transition could be either a first order or second order transition. The hadronic phase is made of different species of the baryon octet along with electrons and muons making a uniform background. This phase is described by the Lagrangian density of Eq. 2.1 as discussed in Chapter 2.

Now, we discuss the antikaon condensed phase composed of all the species of the baryon octet, the antikaon isospin doublet with electron and muons in the background. The baryon-baryon interaction in the antikaon condensed phase is also described by the Lagrangian density of Eq. (2.1). We choose the antikaon-baryon interaction on the same footing as the baryon-baryon interaction. The Lagrangian density for (anti)kaons in the minimal coupling scheme is given by [123, 127, 133, 134]

$$\mathcal{L}_K = D^*_\mu \bar{K} D^\mu K - m^{*2}_K \bar{K} K \,, \tag{4.1}$$

where the covariant derivative is $D_\mu = \partial_\mu + ig_{\omega K}\omega_\mu + ig_{\rho K}\boldsymbol{\tau}_K \cdot \boldsymbol{\rho}_\mu + ig_{\phi K}\phi_\mu$ and the effective mass of (anti)kaons is given by $m^*_K = m_K - g_{\sigma K}\sigma$ where m_K is the bare kaon mass. The isospin doublet for kaons is denoted by $K \equiv (K^+, K^0)$ and that for antikaons is $\bar{K} \equiv (K^-, \bar{K}^0)$. For s-wave ($\mathbf{p} = 0$) condensation, the in-medium energies of $\bar{K} \equiv$

$(K^-, \bar{K}^0)$ are given by

$$\omega_{K^-,\,\bar{K}^0} = m_K^* - g_{\omega K}\omega_0 - g_{\phi K}\phi_0 \mp g_{\rho K}\rho_{03}. \tag{4.2}$$

It is to be noted that for s-wave (**k**=0) $\bar{K}$ condensation at T=0, the scalar and vector densities of antikaons are same and those are given by [134]

$$n_{K^-,\,\bar{K}^0} = 2\left(\omega_{K^-,\bar{K}^0} + g_{\omega K}\omega_0 + g_{\phi K}\phi_0 \pm g_{\rho K}\rho_{03}\right)\bar{K}K\ . \tag{4.3}$$

The requirement of chemical equilibrium fixes the onset condition of antikaon condensations in neutron star matter.

$$\mu_n - \mu_p = \mu_{K^-} = \mu_e\ , \tag{4.4}$$

$$\mu_{\bar{K}^0} = 0\ , \tag{4.5}$$

where μ_{K^-} and $\mu_{\bar{K}^0}$ are respectively the chemical potentials of K^- and $\bar{K}^0$. In the mean field approximation, the meson field equations in the presence of antikaon condensates are given by

$$m_\sigma^2\sigma = \sum_B g_{\sigma B}n_B^s + g_{\sigma K}\sum_{\bar{K}} n_{\bar{K}}\ , \tag{4.6}$$

$$m_\omega^2\omega_0 = \sum_B g_{\omega B}n_B - g_{\omega K}\sum_{\bar{K}} n_{\bar{K}}\ , \tag{4.7}$$

$$m_\rho^2\rho_{03} = \sum_B g_{\rho B}\tau_{3B}n_B + g_{\rho K}\sum_{\bar{K}} \tau_{3\bar{K}}n_{\bar{K}}\ , \tag{4.8}$$

$$m_\phi^2\phi_0 = \sum_B g_{\phi B}n_B - g_{\phi K}\sum_{\bar{K}} n_{\bar{K}}\ , \tag{4.9}$$

Antikaon condensates do not directly contribute to the pressure so it is due to baryons and leptons only. However, the presence of additional term due to (anti)kaons in the meson field equations change the values of mean fields. Also K^- mesons modify the charge neutrality condition. Thus the values of rearrangement term, pressure etc. are changed when (anti)kaons appear. The energy density of (anti)kaons is given by $\epsilon_{\bar{K}} = m^*_K\,(n_{K^-} + n_{\bar{K}^0})$. The total energy density has contribution from the baryons, antikaons and leptons $\epsilon = \epsilon_B + \epsilon_{\bar{K}} + \epsilon_l$, where ϵ_B and ϵ_l are given by Eqs. 2.21 and 2.25, respectively. However, the expression for pressure in addition contains a rearrangement term in the condensed phase ($\Sigma^{(r)}_{\bar{K}}$), that has the same form as Eq. 2.18 and is given by

$$\begin{aligned} P^{\bar{K}} &= -\frac{1}{2}m_\sigma^2\sigma^2 + \frac{1}{2}m_\omega^2\omega_0^2 + \frac{1}{2}m_\phi^2\phi_0^2 + \frac{1}{2}m_\rho^2\rho_{03}^2 + \Sigma^{(r)}_{\bar{K}}\sum_B n_B^{\bar{K}} \\ &+ \frac{1}{3}\sum_B \frac{2J_B+1}{2\pi^2}\int_0^{k_{F_B}} \frac{k^4 dk}{(k^2+m_B^{*2})^{1/2}} + \frac{1}{3}\sum_l \frac{1}{\pi^2}\int_0^{K_{F_l}} \frac{k^4 dk}{(k^2+m_l^2)^{1/2}} \end{aligned} \tag{4.10}$$

Next, we proceed to calculate the mass, radius and structure of compact stars using the realistic equations of state described above. We consider a spherically symmetric star of ideal fluid in hydrostatic equilibrium and solve the Tolman-Oppenheimer-Volkoff (TOV) equation,

$$\frac{dP}{dr} = -\frac{[P(r)+\epsilon(r)][M(r)+4\pi r^3 P(r)]}{r[r-2M(r)]} \ . \tag{4.11}$$

Here, $P(r)$, $\epsilon(r)$ represent the pressure, energy density of the fluid at radius r . The total gravitational mass $M(r)$ enclosed by radius r is given by,

$$M(r) = 4\pi\int_0^r \epsilon(r')r'^2 dr' \tag{4.12}$$

We integrate the TOV equation with the initial condition at the center $P(r=0) = P_c$ and boundary condition at the surface $P(r=R) = 0$.

4.3 Model Parameters

Next, we compute the meson-anti(kaon) couplings on the same footing as that of meson-hyperon couplings. However, we do not consider any density-dependence here. Coupling constants of ω and ρ mesons with kaons are obtained from the quark model and isospin counting rule [127, 134] and the coupling constant of ϕ mesons with kaons is given by the SU(3) relations and the value of $g_{\pi\pi\rho}$ [70],

$$g_{\omega K} = \frac{1}{3} g_{\omega N}; \quad g_{\rho K} = g_{\rho N} \quad \text{and} \quad \sqrt{2}\, g_{\phi K} = 6.04. \tag{4.13}$$

The scalar coupling constant ($g_{\sigma K}$) is obtained from the real part of the K^- optical potential at the normal nuclear matter density [70, 71, 123, 127]

$$U_{\bar{K}}\,(n_0) = -g_{\sigma K}\sigma - g_{\omega K}\omega_0 \, + \Sigma_N^{(r)} \,. \tag{4.14}$$

The study of kaonic atoms clearly suggests an attractive (anti)kaon nucleon optical potential [135, 136]. However, there is controversy about how deep the potential is, whether the (anti)kaon optical potential is extremely deep, as it is preferred by the phenomenological fits to kaonic atoms data, or shallow, as it comes out from unitary chiral model calculations [137]. Different experiments also suggest a range of values for $U_{\bar{K}}$ from -50 to -200MeV and do not come to any definite consensus [138]. We chose a set of values of $U_{\bar{K}}$ from -60 to -140 MeV. The coupling constants for kaons with σ-meson, $g_{\sigma K}$ at the saturation density for these values of $U_{\bar{K}}$ for DD2 model is listed in Table 4.1.

Table 4.1: Parameters of the scalar σ meson -(anti)kaon couplings in DD2 model [97].

$U_{\bar{K}}$ (MeV)	-60	-80	-100	-120	-140
$g_{\sigma\bar{K}}$	-1.24609	-0.72583	-0.20557	0.31469	0.83495

4.4 Results

We report our results calculated using the DD2 model. We begin with the composition of the star in the presence of different exotic particles. As the neutron chemical potential and the Fermi level of nucleons become sufficiently large at high density, different exotic particles could be populated in the core of the star. First we consider antikaon condensates $(K^-, \bar{K}^0)$ in the nucleon-only system consisting of proton, neutron, electron and muon. For $U_{\bar{K}}(n_0) = -60$MeV, K^- appears at $4.11n_0$ in the nucleon-only matter. The threshold density of K^- condensation decreases as the antikaon potential in nuclear matter becomes more attractive. We note that the threshold density of $\bar{K}$ condensation shifts towards lower density as the strength of $|U_{\bar{K}}(n_0)|$ increases. Also, it is observed that K^- condensates populate before $\bar{K}^0$ condensate appears. It is always energetically favorable to populate the condensates of negatively charged kaons, that takes care of the charge neutrality but being condensates, do not add to the pressure unlike the leptons. The threshold densities of $K^-(\bar{K}^0)$ in β-equilibrated matter with different compositions are listed in Table 4.2, the values corresponding to $\bar{K}^0$ condensates are given in the parentheses.

Next, we consider Λ and Ξ^-, Ξ^0 apart from nucleons. At low density, the system consists of only nucleon and leptons until strange baryons appear beyond twice the normal matter density. Λ hyperons are the first to appear at $2.22n_0$, followed by Ξ^- at $2.44n_0$ and finally Ξ^0 sets in at $7.93n_0$. If we allow the (anti)kaons in addition to Λ hyperons, K^-

Table 4.2: Threshold density (in units of n_0) of the K^- ($\bar{K}^0$) condensates in the DD2 model. (-) denotes no-show of them [97].

$U_{\bar{K}}$ (MeV)	-60	-80	-100	-120	-140
np$K^-\bar{K}^0$	4.11(7.16)	3.74(6.62)	3.40(6.07)	3.08(5.54)	2.79(5.00)
np$\Lambda K^-\bar{K}^0$	6.54(-)	5.30(-)	4.35(-)	3.63(7.65)	3.07(6.40)
np$\Lambda\Xi^-\Xi^0 K^-\bar{K}^0$	-(-)	-(-)	-(-)	6.07(8.95)	3.81(6.79)

appears at $3.07n_0$ and $6.54n_0$ at $U_{\bar{K}} = -140$MeV and -60 MeV, respectively. However, $\bar{K}^0$ appears only at higher density and for a deeper potential depth ($|U_{\bar{K}}| \geq 120$ MeV). The presence of hyperons delays the onset of $\bar{K}$ condensation to higher density as evident from Table 4.2. Moreover, negatively charged hyperons diminish the electron chemical potential delaying the onset of K^- condensation.

In Fig. 4.1 we compare the particle fractions for a particular value of $U_{\bar{K}} = -120$MeV. Before the onset of exotic particles, the charge neutrality is maintained among protons, electrons and muons. We see that Λ hyperons appear at 2.22n_0 and its density rises fast at the cost of neutrons. We notice that the onset of K^- condensates takes care of the charge neutrality of the system as soon as it appears at $3.63n_0$ and leptons are depleted. This behaviour is quite expected, as K^- mesons, being bosons, condense in the lowest energy state and are therefore energetically favorable to maintain the charge neutrality of the system. Another notable fact is the rise of proton fraction as soon as the K^- condensate takes care of the negative charge neutrality; leads to an almost iso-spin symmetric matter at higher density.

In case Ξ^- is also present, both the (anti)kaons condense only at higher density and for $|U_{\bar{K}}| \geq 120$ MeV as is noticed in Fig. 4.2. The early onset of Ξ^- hyperons does not allow $\bar{K}$ to appear in the system for lower values of $U_{\bar{K}}$. We see the competition of all the exotic

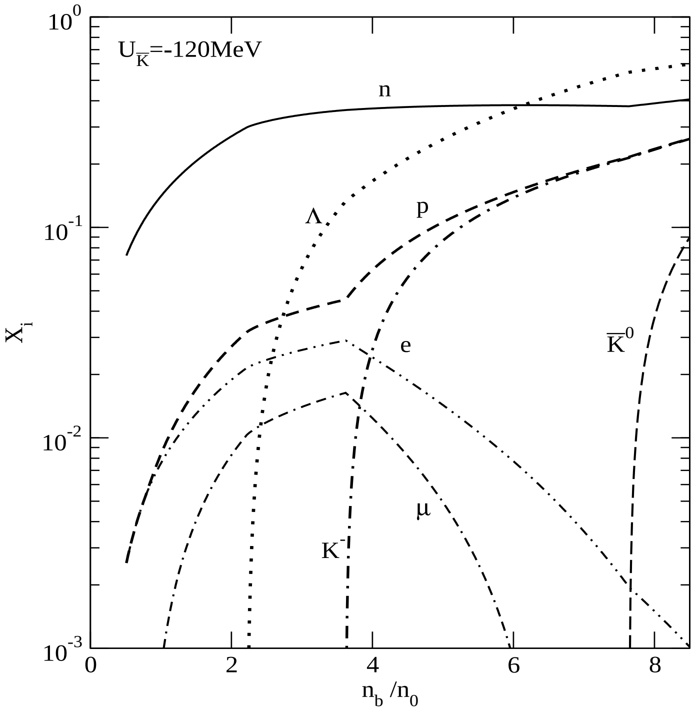

Figure 4.1: Fraction of various particles in β-equilibrated n, p, Λ and lepton matter including K^- and $\bar{K}^0$ condensates for $U_{\bar{K}}(n_0) = -120$ MeV as a function of normalized baryon density [97].

particles in Fig. 4.2 for $U_{\bar{K}} = -120 \text{ and } - 140$MeV. Though the onset of Ξ^- delays the appearance of antikaon condensates, with stronger $U_{\bar{K}} = -140$MeV, K^- suppresses Ξ^- and even manages to replace it completely at higher density.

In Fig. 4.3 pressure (P) is plotted against energy density (ϵ) for system consisting of nucleons and (anti)kaons for different $U_{\bar{K}}$. The solid line corresponds to the nucleon-only matter whereas the other lines correspond to the matter including K^- and $\bar{K}^0$ condensates for antikaon optical potentials $U_{\bar{K}}(n_0)$ = -60 to -140 MeV. The EoS is softened as soon as the K^- and $\bar{K}^0$ appear, the effect being more pronounced for a deeper $U_{\bar{K}}$. The EoS with $U_{\bar{K}} = -140$MeV is the softest. The kinks in the EoS at mid energy densities ($426.5 \text{ to } 693.0 MeV fm^{-3}$) correspond to the K^- onset and those at higher densities

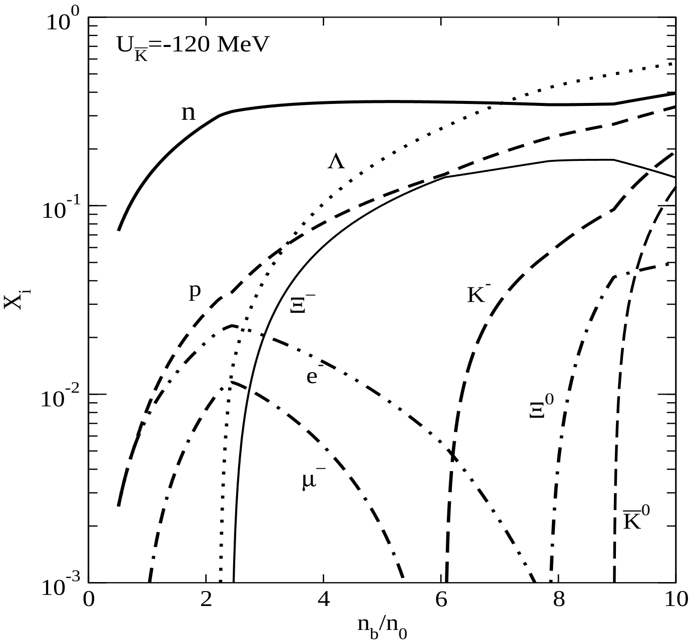

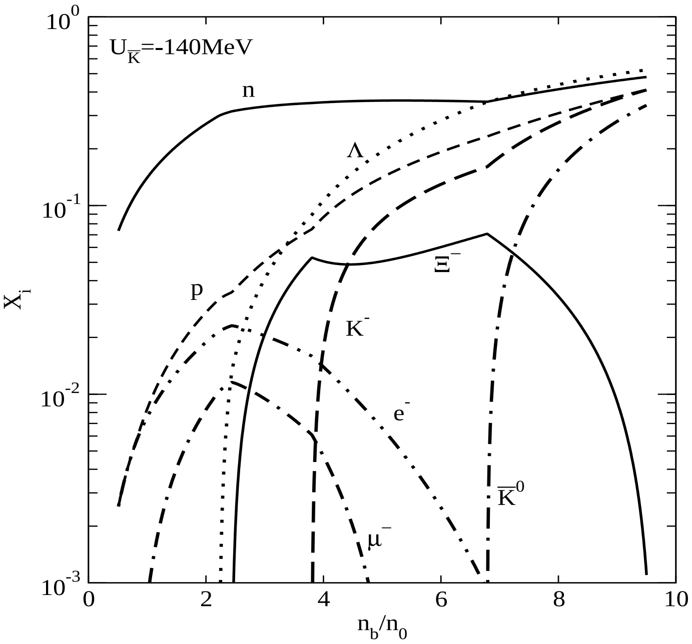

Figure 4.2: Fraction of various particles in β-equilibrated n, p, Λ, Ξ^-, Ξ^0 and lepton matter including K^- and $\bar{K}^0$ condensates for $U_{\bar{K}}(n_0) = -120$ MeV and -140 MeV as a function of normalized baryon density [97].

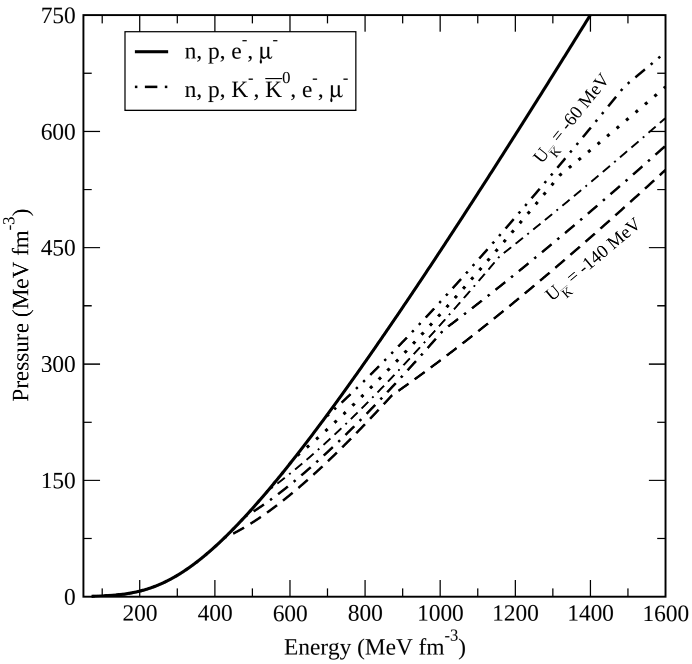

Figure 4.3: The equation of state (EoS), pressure (P) vs energy density (ϵ). The full line is for n, p, and lepton matter whereas others are with additional K^- and $\bar{K}^0$ condensates calculated with $U_{\bar{K}}(n_0)$= -60,-80,-100,-120 and -140 MeV. Deeper $U_{\bar{K}}$ corresponds to softer EoS [97].

(872.1 to $1492.6 MeV fm^{-3}$) mark the $\bar{K}^0$ condensation. Similarly we draw the EoS in the presence of hyperons in Fig. 4.4. With the appearance of Λ hyperons at $330\text{MeV}fm^{-}3$, the slope of the EoS deviates from the nucleon one. The EoS is further softened at the onset of Ξ^-. However, the EoS considering all the exotic particles is not the softest one here. We have seen that hyperons delay (anti)kaons to higher density. This explains the relative stiffness of the EoS at higher density in the presence of Ξ along with other particles. In the figure we only draw the (anti)kaon EoS corresponding to $U_{\bar{K}}(n_0) = -120$ MeV.

We solve the TOV equations to find the stellar structure of a static compact stars and show our result in Figs. 4.5, 4.6 corresponding to the equations of state of Fig 4.3 and 4.4, respectively. For low density ($n < 0.001 fm^{-3}$) crust, we used the EoS of Baym,

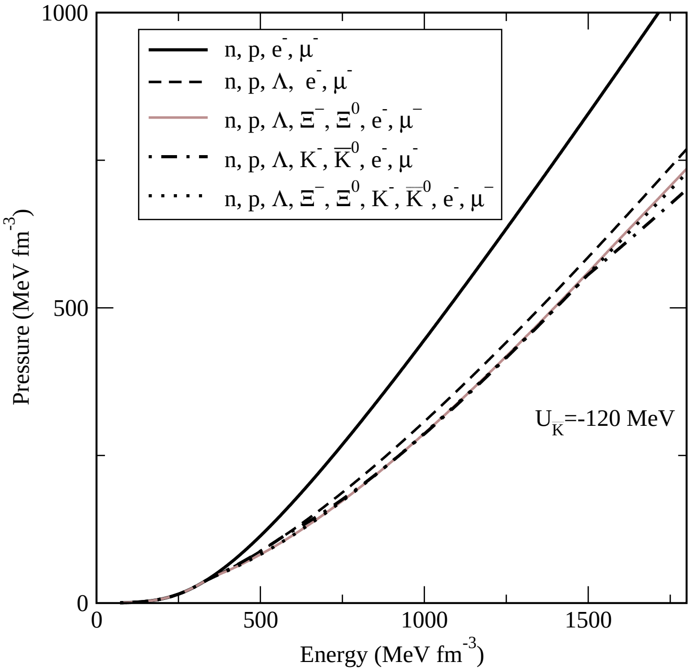

Figure 4.4: The equation of state (EoS), pressure (P) vs energy density (ϵ) for various particle combination of n, p, Λ, Ξ^-, Ξ^0 and lepton in β-equilibrated matter including K^- and $\bar{K}^0$ condensates with $U_{\bar{K}}(n_0)$=-120 MeV [97].

Pethick and Sutherland [139]. The set of maximum mass of the nucleons-only and hyperon stars and their corresponding central densities and radii corresponding to EoS of Fig. 4.4, are listed in Table 4.3. The gray band in both figures marks the observational limits of Refs. [49, 50]. We notice that in all the cases the values of the maximum mass lie

Table 4.3: Maximum mass, central density and radius of nucleons only as well as hyperon compact stars in the DD2 model. Maximum mass is in $M_\odot$, central density with respect to the saturation density n_0, radius in km. [97]

	$M(M_\odot)$	n_c (n_0)	R (Km)
np	2.417	5.71	11.87
npΛ	2.10	6.40	11.57
np$\Lambda\Xi$	2.032	6.66	11.42

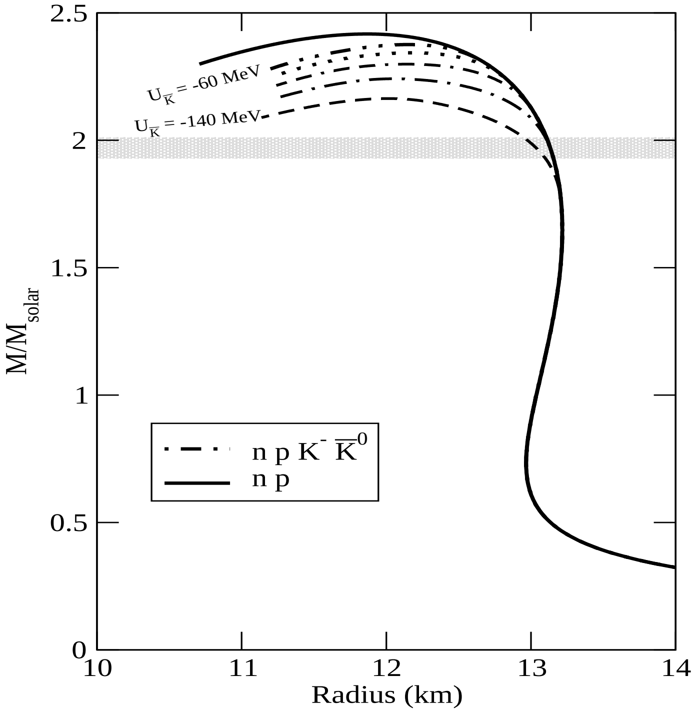

Figure 4.5: The neutron star mass sequences are plotted with radius for the equations of state of Fig. 4.3. The full line is for n, p, and lepton matter whereas others are with additional K^- and $\bar{K}^0$ condensates calculated with $U_{\bar{K}}(n_0)$= -60,-80,-100,-120 and -140 MeV. Deeper $U_{\bar{K}}$ corresponds to lower line. The gray band specifies the observational limits [97].

well above the benchmark $2.0\ M_\odot$, the radii being within the range of 11.42 to 11.87 km. Radii decreases with additional exotic degrees of freedom. Softer the EoS, less mass it can support against gravity and more compact is the star. The maximum mass of a nucleon-only star is $2.417 M_\odot$, with the inclusion of Λ and Ξ hyperons this reduces to $2.1 M_\odot$ and $2.032 M_\odot$ respectively. It is noted that the core contains Λ and Ξ^-, but no Ξ^0 and is denser compared to the nucleon-only case.

Table 4.4 enlists the values of maximum mass and its corresponding central energy density and radius for the hyperons and (anti)kaons EoS with different values of optical potential. When we consider (anti)kaons in addition to the nucleons, they are found to

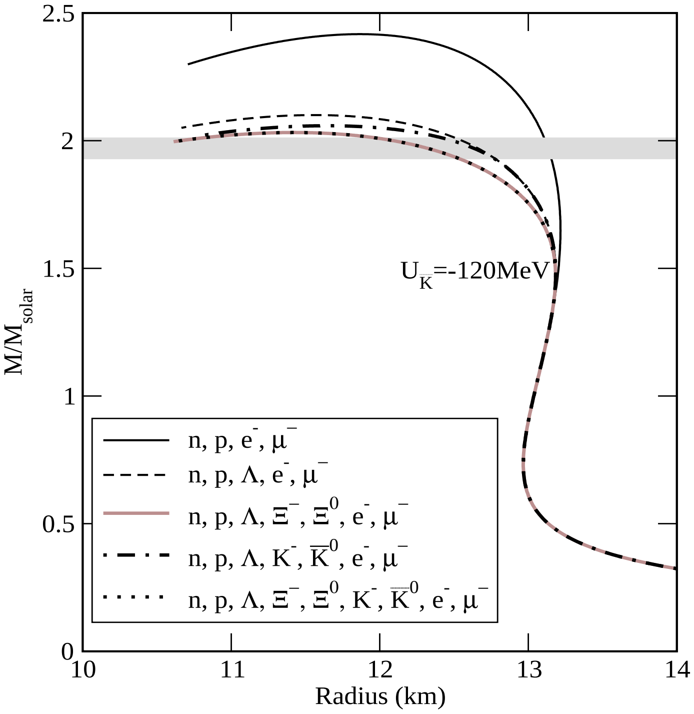

Figure 4.6: The neutron star mass sequences are plotted with radius for the equations of state of Fig. 4.4. The gray band specifies the observational limits [97].

reduce the maximum mass of the star for all $U_{\bar{K}}$, but the central density does not increase until it has got $\bar{K}^0$, which happens only $|U_{\bar{K}}| \geq 120$ MeV. In the presence of Λ hyperons, for $U_{\bar{K}}$ as low as -60 MeV, antikaons do not have any effect on the maximum mass, as K^- condensate appears at $6.54n_0$, that is beyond the central density and $\bar{K}^0$ does not appear at all. The effect of K^- condensates is pronounced from $|U_{\bar{K}}| = 80$ MeV, where the core contains considerable fraction of K^-, but still no $\bar{K}^0$ condensates. Both (anti)kaons appear only at $|U_{\bar{K}}| \geq 120$ MeV and reduce the maximum mass.

Next we discuss the scenario when our system contains Ξ's in addition to nucleons, Λ and $\bar{K}$. Though $\bar{K}$ appears for $|U_{\bar{K}}| \geq 120$ MeV, the maximum mass is reduced for $U_{\bar{K}} = -140$ MeV only. As it is evident from Fig. 4.2, the core (density $6.65n_0$) contains only 2% and 15.5% of K^- condensate for the two cases respectively whereas $\bar{K}^0$ does

Table 4.4: Maximum mass, central density and radius of compact stars with nucleons, hyperons and (anti)kaons for different values of optical potential depth in the DD2 model. Maximum mass is in M_{solar}, central density in n_0, radius in km and $U_{\bar{K}}$ in MeV. [97]

$U_{\bar{K}}$	-60			-80			-100			-120			-140		
	M	n_c	R	M	n_c	R	M	n_c	R	M	n_c	R	M	n_c	R
np$K^-\bar{K}^0$	2.376	5.54	12.15	2.343	5.53	12.18	2.299	5.6	12.14	2.242	5.78	12.05	2.164	5.91	12.01
np$\Lambda K^-\bar{K}^0$	2.10	6.4	11.57	2.098	6.35	11.62	2.085	6.29	11.68	2.058	6.36	11.64	2.02	6.63	11.48
np$\Lambda\Xi^-\Xi^0 K^-\bar{K}^0$	2.032	6.66	11.42	2.032	6.66	11.42	2.032	6.66	11.42	2.032	6.65	11.43	2.016	6.67	11.4

not populate the core at all. So only K^- condensate plays effective role in reducing the maximum mass of the star, that also for optical potential deeper than -120 MeV.

4.5 Summary

We study the equation of state and compositions of hyperons and antikaon condensates in neutron star matter within the framework of relativistic field theoretical model with density-dependent couplings. The density dependence of nucleon-meson couplings are determined following the DD2 model of Typel *et. al* [72, 73]. The density dependent meson-hyperon vertices are obtained from the density dependent meson-nucleon couplings using hypernuclei data [70], scaling law [140] and SU(6) symmetry. The scalar meson coupling to Λ and Ξ hyperons are fitted to the potential depth of respective hyperons in saturated nuclear matter, which is available from experiments. A repulsive interaction between the hyperons is mediated by the exchange of $\phi(1020)$ mesons. The couplings of antikaon-nucleon interactions are obtained in the similar manner. However, they are not density-dependent.

The abundance of all the particles considered here matches with the results of other models. In all the cases, Λ hyperons get into the system first, followed by the negatively charged Ξ^- hyperons. The antikaon condensates also populate the nuclear matter at reasonably low densities for a deeper optical potential. However, in hyperon-rich matter their appearance is delayed until higher densities. Also, the negatively charged hyperons diminish the electron chemical potential delaying the onset of K^- condensation. All these findings are consistent with earlier results.

Neutron star masses have been precisely measured for some binary pulsars. Until very recently, the largest precisely measured NS mass is $1.97 \pm 0.04 M_\odot$ for PSR J1614-2230, and $2.01 \pm 0.04 M_\odot$ for PSR J0348+0432. We observe that the strangeness degrees of freedom softens the nuclear EoS that results into the reduction of neutron star maximum mass. Most of the existing models conflicts with the observation of such high pulsar masses. However, in all the cases we find the maximum mass within the constraint of observational limits. So we conclude that exotic EoS can not be ruled out by the observation of a $2M_\odot$ compact star. In the framework of the DD2 model, there is a scope for accommodating strange hyperons and antikaon condensates within the observational limits of neutron star mass.

CHAPTER 5

MAGNETOELASTIC OSCILLATIONS OF NEUTRON STARS

5.1 Introduction

Soft gamma repeaters (SGRs) are characterized by their emission of bright and repetitive flashes of soft gamma rays. There are about 14 SGRs known observationally [141]. In section 1.6, we have discussed the types of bursting events and their luminosities that can be associated with the SGRs. Among them, the giant flares are very rare and exceptional event that can only be exceeded by gamma ray bursts and blazers in terms of luminosity [53]. So far only three cases of giant flares have been recorded and those are SGR 0526-66 in 1979, SGR 1900+14 in 1998 and SGR 1806-20 in 2004 [54, 142–145]. In all those giant flares, the early part of the light curve was dominated by a spectrally hard spike of short duration (~ 0.5s) followed by an extended softer decaying tail which is modulated at the neutron star's spin period. The tail pulsated with high amplitude and lasted for a few hundreds of seconds (~ 50 cycles) [146].

SGRs are proposed candidates for magnetars which are neutron stars that have very high magnetic fields $\sim 10^{14} - 10^{15}$ G [52,147,148] on the surface and possibly much higher internal fields [149, 150]. Giant flares might be caused by the evolving magnetic field. Since the field is very strongly coupled with the the crust of magnetars, its reconfiguration could induce severe stress on the crust that might result in starquakes. The precise interplay between the magnetospheric twist and magnetar crust is still not well understood. However, it was argued that starquakes produced by the giant flares could excite Global Seismic Oscillations (GSOs) [147]. Quasi-periodic oscillations were found in the decaying tail of giant flares of SGR 1806-20 and SGR 1900+14. Detected frequencies for SGR 1806-20 are 18, 26, 30, 92.5, 150, 626 and 1838 Hz [54–56], whereas for SGR 1900+14 detected frequencies are 28, 53.5, 84 and 155 Hz [151]. Huppenkothen et al [152–154] recently analyzed short bursts of some SGRs and found QPOs with frequencies 93 and 127 Hz in SGR J1550-5418 [152] and with 57 Hz in SGR 1806-20 [153].

It was noted from earlier theoretical models, that the higher frequencies of the observed QPOs could be explained reasonably well using pure shear modes as well as crustal magneto-elastic (CME) modes [144, 147, 155–160]. On the other hand, the lower frequencies might be identified with the Alfvén oscillation of the fluid core. This makes the study of the oscillations of magnetar more difficult. There were models to explain frequencies of QPOs using only Alfvén oscillations of the fluid core neglecting the effect of the crust [158, 161–163]. Levin [161, 164] first pointed out that the strong magnetic fields of magnetars should couple the Alfvén oscillations of fluid core with the oscillations in the solid crust. After that many authors studied the problem in detail [165–169]. The magneto-hydrodynamics (MHD) coupling between the crust and core causes pure crustal modes to decay by emitting Alfvén waves into the crust. It was argued that CME modes might still appear in GSOs and explain frequencies of observed QPOs for not very strong magnetic fields [170]. But global modes are expected to couple to the Alfvén continuum in the core, and leads to the damping of the modes. Simulations to simplified models show [161, 165] that CME oscillations are efficiently damped in the Alfvén continuum as the crust reacts to the motion of the core. Consequently long-lived QPOs can be generated at special points of the continuum (turning points and edges of continuum).

Several groups also studied the effect of neutron superfluidity and/or proton superconductivity of the crust and/or core on the calculated frequencies of magnetars [171–173]. It was noted that neutron superfluidity enhanced fundamental frequencies of magneto-elastic oscillations. On the other hand, it was argued that proton superconductivity could be destroyed in magnetic fields $> 5 \times 10^{16}$ G [174].

Nuclear physics of crusts plays an important role on the magneto-elastic modes of magnetars. In particular, the effects of the nuclear symmetry energy on the CME frequencies were investigated recently [160]. CME mode frequencies are sensitive to the shear modulus of neutron star crusts which strongly depends on the composition of the crusts. In earlier studies of magneto-elastic modes the effect of magnetic field on the composition of the crust was not considered. Surface magnetic fields as large as $\sim 10^{15}$ G have been reported in magnetars. Further, indirect estimates using the scalar virial theorem does not exclude internal magnetic fields up to 10^{18} G. Such large magnetic fields in magnetars may influence the ground state properties of neutron star crusts. Recently, the influence of Landau quantization of electrons on the compositions and equations of state (EoS) of outer and inner crusts have been investigated and appreciable changes were obtained in those properties when the magnetic field is very strong ($B \geq 10^{17}$ G) [175, 176]. This, in turn, might influence the shear modulus of crusts and thereby magneto-elastic frequencies of magnetars. This motivates us to study both crustal and global modes of oscillations of magnetars using magnetized crusts. We define the crust to be magnetized (non-magnetized) when the effect of magnetic field on the crustal composition is considered (not considered).

We organize the chapter in the following way. We describe models for calculating oscillation modes, shear modulus and compositions and EoS of magnetized crusts in Sec. 5.2. Results of this calculation are discussed in Sec. 5.3. Sec. 5.4 gives the summary and conclusions.

5.2 Formalism

QPOs were investigated in Newtonian gravity [147,155,177,178] as well as general relativity [156, 158, 170, 179, 180] with and without magnetic fields and also crust-core coupling was included in some of those studies. But the magnetic field strongly couples the crust to the core and we need to take that into consideration while calculating the magneto-elastic modes.

Here we first study the effects of magnetized crusts on the magneto-elastic modes confined to the crust (CME) only, by considering a free slip between the crust and the core. Next, we calculate the global magneto-elastic (GME) modes where coupling between the crust and the core has been considered. Mode frequencies are calculated following the model of Refs. [156, 180, 181]. The spherically symmetric general relativistic model of Sotani et al. [181] adopted in this calculation is a simplified one compared with the state-of-the-art general relativistic magnetohydrodynamical (MHD) model [168]. Furthermore, we do not consider the coupling to the Alfvén continuum within the framework of this study, as the aim of this work primarily is to investigate the influence of magnetized crusts on QPOs.

It is well known that a strong magnetic field breaks the spherical symmetry of a neutron star due to anisotropy of the energy momentum tensor [182]. Hence the isotropic Tolman-Oppenheimer-Volkoff (TOV) equations are no longer applicable for computing the mass-radius relations for polar magnetic fields $\sim 10^{17}$ G.

Ideally for large magnetic fields, one must then calculate the neutron star structure using the anisotropic stress-energy tensor and solving equations for hydrostatic equilibrium [149]. Although this approximation is reasonable for magnetic fields $< 10^{17}$ G, the deviations from spherical symmetry become non-negligible for higher fields. However, the aim of this work is to study the relative changes in the mode frequencies due to magnetic fields. For this reason, we neglect the deformation of the neutron star and assume it to be spherically symmetric. The metric used to determine equilibrium stellar models has the form,

$$ds^2 = -e^{2\Phi}dt^2 + e^{2\Lambda}dr^2 + r^2\left(d\theta^2 + sin^2\theta d\phi^2\right) \ . \tag{5.1}$$

The equilibrium models are obtained by solving the Tolman-Oppenheimer-Volkoff (TOV) equation with a perfect fluid EoS.

Here we consider an axisymmetric poloidal magnetic field generated by four current $J_\mu = (0, 0, 0, J_\Phi)$ and expand the four-potential into vector spherical harmonics as $A_\mu = a_{\ell_m}(r)sin\theta\partial_\theta P_{\ell_m}(cos\theta)$.

The perturbed equations are obtained by linearizing the equations of motion of the fluid and the magnetic induction equation [156, 180]. Torsional modes are incompressible and do not result in any appreciable density perturbation in equilibrium stars. Consequently, one may adopt the relativistic Cowling approximation and neglect metric perturbations $\delta g_{\mu\nu}$=0 [183]. We consider axial type perturbation in the four velocity and the relevant perturbed matter quantity is the ϕ-component of the perturbed four velocity ∂u^{ϕ} [156]

$$\partial u^{\phi} = e^{-\Phi}\partial_t \mathcal{Y}(t,r)\frac{1}{sin\theta}\partial_\theta P_l(cos\theta) \ , \tag{5.2}$$

where ∂_t and ∂_θ correspond to partial derivatives with respect to time and θ, respectively, $P_l(cos\theta)$ is the Legendre polynomial of order l and $\mathcal{Y}(t,r)$ is the angular displacement of the matter. It is to be noted that the radial and angular variations of azimuthal displacement of stellar matter lead to shears of the crystal lattice in neutron star crusts which are described by the shear tensor $S_{\mu\nu}$ [179]. Further, the shear stress tensor is given by $T_{\mu\nu} = -2\mu S_{\mu\nu}$, where μ is the isotropic shear modulus. The linearized equations of motion includes the contribution of $\delta T_{\mu\nu}$ [156].

Assuming a harmonic time dependence for $\mathcal{Y}(t,r) = e^{i\omega t}\mathcal{Y}(r)$ and neglecting $\ell \pm 2$ terms, one obtains the eigenvalue equation for the mode frequency [156]

$$\begin{aligned}
&\left[\mu + (1+2\lambda_1)\frac{{a_1}^2}{\pi r^4}\right]\mathcal{Y}'' + \Biggl\{ \left(\frac{4}{r} + \Phi' - \Lambda'\right)\mu \\
&\qquad + \mu' + (1+2\lambda_1)\frac{a_1}{\pi r^4}\left[\left(\Phi' - \Lambda'\right)a_1 + 2{a_1}'\right]\Biggr\}\mathcal{Y}' \\
&\qquad + \Biggl\{\left[\left(\epsilon + p + (1+2\lambda_1)\frac{{a_1}^2}{\pi r^4}\right)e^{2\Lambda} - \frac{\lambda_1 {a_1'}^2}{2\pi r^2}\right]\omega^2 e^{-2\Phi} \\
&\qquad - (\lambda - 2)\left(\frac{\mu e^{2\Lambda}}{r^2} - \frac{\lambda_1 {a_1'}^2}{2\pi r^4}\right) \\
&\qquad + \frac{(2+5\lambda_1)a_1}{2\pi r^4}\left[\left(\Phi' - \Lambda'\right){a_1}' + {a_1}''\right]\Biggr\}\mathcal{Y} = 0 \ ,
\end{aligned} \tag{5.3}$$

where $\lambda = \ell(\ell{+}1)$ and $\lambda_1 = -\ell(\ell{+}1)/(2\ell{-}1)(2\ell{+}3)$. Equation (5.3) reduces to the non-magnetic case when we put $a_1 = 0$ [156]. Sotani et al. [159] showed that the $\ell{\pm}2$ truncation worked well for oscillations confined to the crust only. The eigenvalue equation for modes confined to the crust was solved using a two dimensional numerical method where $\ell \pm 2$ terms were not truncated [159]. It was demonstrated that results were unaffected whether $\ell \pm 2$ terms were truncated or not. With suitable choice of new variables, Eq.(5.3) results in a system of first order ordinary differential equations [156]. For magneto-elastic modes confined to the crust, we impose a zero traction boundary condition at the interface between the core and the crust as well as the zero torque condition at the surface [156, 170]. These conditions imply $\mathcal{Y}' = 0$ at the surface ($r = R$) of the star and the interface ($r = R_c$) of the crust and core. For the GME modes the boundary condition at the surface is the same as CME modes [156, 168]. The other boundary condition is the regularity at the center ($\mathcal{Y} \sim r^{\ell-1}$). Finally, we estimate eigenfrequencies by solving two first order differential equations.

The knowledge of the shear modulus of magnetized crusts is an important input in the eigenvalue equation [Eq.(5.3)] for the CME mode calculation. Here we adopt the following expression of the shear modulus at zero temperature [184, 185]

$$\mu = 0.1194\frac{n_i(Ze)^2}{a} \,, \tag{5.4}$$

where $a = [3/(4\pi n_i)]^{1/3}$, Z is the atomic number of a nucleus and n_i is the ion density. This form of the shear modulus was obtained by assuming a bcc lattice and performing directional averages [186]. Further the dependence of the shear modulus on temperature was also investigated with the Monte Carlo sampling technique by Strohmayer et al. [185]. The composition and equation of state of neutron star crusts are essential ingredients for the calculation of the shear modulus as it is evident from Eq.(5.4).

Now we describe the ground state properties in outer and inner crusts in the presence of strong magnetic fields. The outer crust is composed of nuclei immersed in a uniform background of a non-interacting electron gas. To minimize the Coulomb energy, nuclei are arranged in a bcc lattice in neutron star crusts [139]. In the Wigner-Seitz approximation, each lattice point is replaced by a spherical, charge-neutral cell with a nucleus (A, Z) at the center. Equilibrium nucleus is obtained by minimizing Gibbs free energy per particle at fixed pressure$P$ and varying A and Z,

$$g = \frac{E_{tot} + P}{n_b}, \tag{5.5}$$

where n_b is the baryon density and the energy density $E_{tot} = n_N(W_N + W_L) + \varepsilon_e$ includes contributions from the energy of the nucleus (W_N), lattice energy (W_L) of the cell including the finite size effects and free electron gas (ε_e) [175, 187]. Similarly, the pressure is given by the sum of the pressure of the lattice and free electron gas.

$$P = P_e + \frac{1}{3} W_L n_N \ , \tag{5.6}$$

where, the electron gas pressure, $P_e = \mu_e n_e - \varepsilon_e$.

At neutron drip point, neutrons start coming out of nuclei. This is the beginning of the inner crust where nuclei are immersed both in free neutrons as well as electrons. The ground state properties of matter of the inner crust is described using the Thomas-Fermi model [175]. Nuclear liquid phase co-exists with the free neutron gas phase in the spherical Wigner-Seitz cell but a clear nucleus is not defined. We adopt the procedure of Bonche, Levit and Vautherin to subtract the free neutron gas of the cell and obtain the nucleus [188–190]. The thermodynamic potential of the nucleus is given by,

$$\Omega_N = \Omega_{NG} - \Omega_G, \tag{5.7}$$

where Ω_G Ω_{NG} are the thermodynamical potentials for the free neutron gas and the total of the nucleus plus the free neutron gas respectively. Here, the thermodynamic potential is defined by,

$$\Omega = \mathcal{F} - \sum_{q=n,p} \mu_q n_q \ , \tag{5.8}$$

where $\mathcal{F}$, μ_q and n_q are the free energy density, baryon chemical potential and number density respectively. The free energy density is defined by,

$$\mathcal{F}(n_q, Y_p) = \int [\mathcal{H} + \varepsilon_c + \varepsilon_e] d\mathbf{r} \ , \tag{5.9}$$

which includes nuclear energy density calculated from nucleon-nucleon potentials, Coulomb energy density and energy density of free electron gas [176, 190].

For neutron star crusts in strongly quantizing magnetic fields, it was showed earlier that the Landau quantization of electrons strongly influenced ground state properties of neutron star crusts in strong magnetic fields $\sim 10^{17}$ G [175, 176]. Energy and number densities of electrons in presence of a magnetic field B are given by [175, 187],

$$\varepsilon_e = \frac{eB}{2\pi^2} \sum_0^{\nu_{max}} g_\nu \int_0^{p_{f_e}(\nu)} E_e(\nu, p_z) dp_z \ , \tag{5.10}$$

$$n_e = \frac{eB}{2\pi^2} \sum_0^{\nu_{max}} g_\nu p_{f_e}(\nu) \ , \tag{5.11}$$

where, ν is the Landau quantum number, g_ν is the spin degeneracy factor, p_{f_e} is the Fermi momentum of electron and

$$E_e(\nu, p_z) = \left[p_z^2 + m_e^2(1 + 2\nu B_*)\right]^{1/2} \ , \tag{5.12}$$

is the energy eigenvalue of relativistic electrons. These quantities are affected by the phase space modifications due to Landau quantization of electrons. So, the modification in the electron energy density will be manifested in Eqs. 5.5, 5.6 and 5.9 which, in turn, will modify the compositions and EoS of crusts. It is to be noted that protons are only influenced by magnetic fields through the charge neutrality condition.

5.3 Results and Discussions

The composition and EoS of ground state matter in neutron star crusts in strong magnetic fields have already been studied [175, 176]. We noted that the electron number density in the outer crust was enhanced compared with the field free case when a few Landau levels were populated for magnetic fields $> 4.414 \times 10^{16}$ G [175]. It was observed that this enhancement grew stronger when only the zeroth Landau level was populated at a magnetic field strength of 4.414 $\times 10^{17}$ G. Consequently, it was found that modifications in the sequence of equilibrium nuclei which was obtained by minimizing the Gibbs free energy per nucleon. It was noted that some new nuclei such as $^{88}_{38}$Sr and $^{128}_{46}$Pd appeared and some nuclei such as ^{66}Ni and ^{78}Ni disappeared in a magnetic field of $B = 4.414 \times 10^{16}$ G [175] when this was compared with the zero field case. It was further observed that the neutron drip point was shifted to higher density in presence of a strong magnetic field with respect to the field free case [175]. Nandi et. al also performed the calculation of the inner crust using the SLy4 and SkM nucleon-nucleon interactions [176]. In this case too, they calculated the equilibrium nucleus at each density point. Like the outer crust in strong magnetic fields, the electron number density was enhanced due to the electron population in the zero Landau level for magnetic fields $\geq 10^{17}$ G which , in turn, led to a large proton fraction because of charge neutrality. For magnetic fields $> 10^{17}$ G, equilibrium nuclei with larger mass and atomic numbers were found to exist in the crust [176]. The free

Table 5.1: Saturation nuclear matter properties of different Skyrme nucleon-nucleon interactions used in this work such as saturation density (ρ_0), binding energy (BE), incompressibility (K), symmetry energy (J) and its slope coefficient (L) [191]

Parameter set	ρ_0 (fm^{-3})	BE (MeV)	K (MeV)	J (MeV)	L (MeV)
SLy4	0.16	15.97	229.91	32.00	45.94
SkM	0.16	15.77	216.61	30.75	49.34
Sk272	0.155	16.28	271.51	37.40	91.67

energy per nucleon of the nuclear system was reduced in magnetic fields compared with the corresponding case without a magnetic field. Furthermore, it was noted that higher symmetry energy in the sub-saturation regime for the SLy4 interaction resulted in nuclei with larger mass and atomic numbers than those of the SkM interaction.

In this work, we perform calculations of shear modulus and magneto-elastic mode frequencies using the SLy4, SkM and Sk272 nucleon-nucleon interactions. Saturation nuclear matter properties of those interactions are listed in Table 5.1. It is evident from the table that those nucleon-nucleon interactions differ in the symmetry energy and its slope coefficient from one interaction to the other. It is to be seen how the behaviour of the symmetry energy and its slope coefficient in the sub-saturation density would impact the compositions of magnetized crusts, its shear modulus and finally magneto-elastic modes.

We calculate the shear modulus using Eq. 5.4 and the above mentioned models of magnetized crusts. Figure 5.1 displays the shear modulus as a function of mass density for three nucleon-nucleon interactions of Table 5.1 with and without magnetic fields. Here we have shown results for $B_* = B/B_c = 10^4$ where $B_c = 4.414 \times 10^{13}$ G, where B denotes the magnetic field strength at the pole. When the field strength is $< 10^{17}$ G, the shear modulus does not show any appreciable change from that of the zero field because of large numbers of Landau levels are populated in this case. As the field strength is increased, less

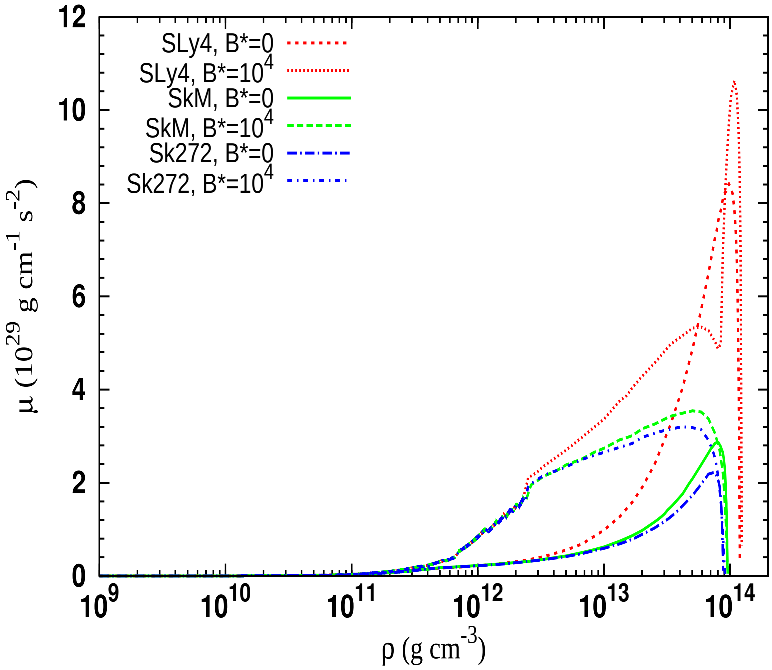

Figure 5.1: Shear modulus as a function of mass density for a neutron star of 1.4 $M_\odot$ with magnetic fields $B_* = 0$ and $B_* = 10^4$ and Skyrme nucleon-nucleon interactions of Table 5.1 [191].

numbers of Landau levels are populated. For $B_* = 10^4$ i.e. 4.414×10^{17} G, the shear modulus is enhanced due to the population of all electrons in the zeroth Landau level. In all three cases, the shear modulus increases with mass density well before the crust-core interface. It is observed from Fig. 5.1 that the shear modulus is highest for the SLy4 nucleon-nucleon interaction whereas it is the lowest for the Sk272 interaction. This can be understood by noting that the symmetry energy at sub-saturation densities is highest for the SLy4 interaction. In this density regime, the symmetry energy decreases from its value at the saturation density according to the slope coefficient (L). As the SLy4 interaction has the lowest value of L (see Table 5.1), it has the highest value of the symmetry energy among all three nucleon-nucleon interactions. Higher symmetry energy leads to higher proton fraction and consequently higher electron fraction due to the charge neutrality. Therefore, higher symmetry energy implies higher shear modulus as is evident from Eq. (5.4). The shear modulus and shear speed $v_s = (\mu/\rho)^{1/2}$ are extrapolated to the zero value at the crust-core interface for magnetized as well as non-magnetized crusts. At densities close to the crust-core boundary nuclei can take various non-spherical shapes collectively known as nuclear pasta [192–194]. As the detailed nature of this pasta phase is not fully settled and there is no calculation of the shear modulus of this phase yet and as the shear modulus should vanish at the crust-core boundary, we extrapolate the shear modulus and shear speed $v_s = (\mu/\rho)^{1/2}$ to the zero value at the crust-core interface for magnetized as well as non-magnetized crusts. This approach is similar to that of Ref. [170] where an arbitrary fit was used so that the shear modulus smoothly decreases to zero at the crust-core interface, in the absence of magnetic fields. We generate profiles of the shear modulus as a function of radial distance in a neutron star for calculating frequencies of magneto-elastic modes. The shear modulus profiles along with the profiles of energy density and pressure are obtained by solving the TOV equation. In this context, we construct the EoS of dense nuclear matter in strong magnetic fields in neutron star core using a relativistic mean field model with the GM1 parameter set as described in Ref. [150, 195, 196]. This EoS of dense nuclear matter is matched with the EoS of the crust and used in the TOV equation.

5.3.1 CME modes

First we study the magneto-elastic modes confined to the crust only. We investigate the dependence of these mode frequencies on the compositions and the shear modulus of magnetized crusts. Earlier all calculations were performed using non-magnetic neutron star crusts. Here we exploit models of non-magnetic as well as magnetic crusts which were

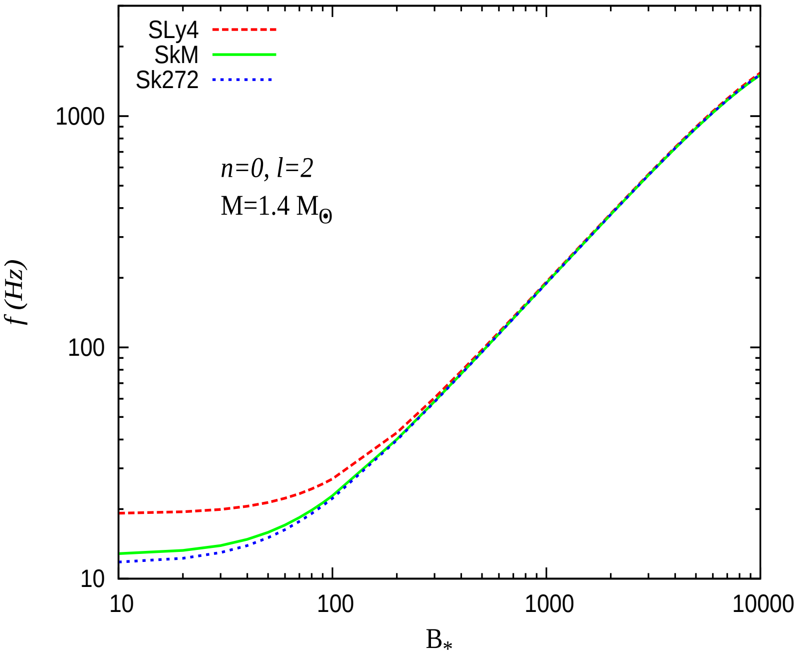

Figure 5.2: Frequency of fundamental ($n = 0$, $\ell = 2$) CME mode for a neutron star of 1.4 $M_\odot$ is shown as a function of magnetic field $B_* = B/B_c$ where $B_c = 4.414 \times 10^{13}$ G. Results of our calculations using the SLy4, SkM and Sk272 nucleon-nucleon interactions are shown here. [191].

already described in this section. We consider CME modes of a neutron star of mass 1.4 $M_\odot$. Frequencies of fundamental ($n = 0$, $\ell = 2$) CME modes are plotted with magnetic fields in Fig. 5.2 for all three nucleon-nucleon interactions. Here n gives the number of radial nodes in the eigenfunction $\mathcal{Y}(r)$, in the crust.

It is observed that in each case the frequency increases very slowly with magnetic field for $B^* < 100$. But for $B^* > 100$, the frequency increases linearly with magnetic fields. This behavior was also observed in earlier studies [156, 181]. The frequencies corresponding to the SLy4 interaction for $B^* < 100$, are almost two times higher than those of the SkM and Sk272 interactions. This is the direct consequence of the higher value of shear modulus for the SLy4 interaction than the other two interactions. However,

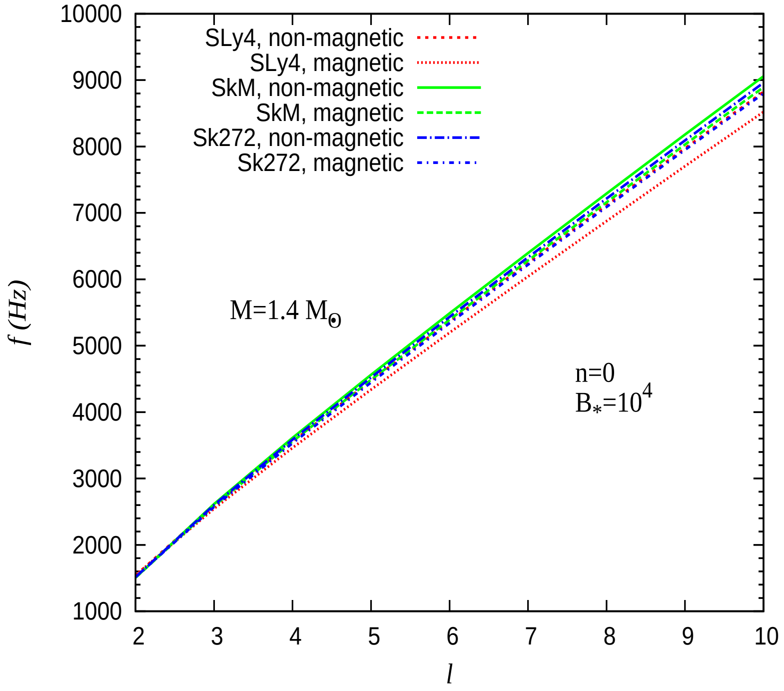

Figure 5.3: Fundamental frequencies ($n = 0$) of CME modes are plotted as a function of ℓ values with and without magnetic crusts of a 1.4 $M_\odot$ neutron star based on the SLy4, SkM and Sk272 nucleon-nucleon interactions for $B_* = 10^4$. [191]

there are no differences between our results with and without magnetized crusts. This shows that the increase in shear modulus due to magnetic field is too small to change the fundamental modes even for very high fields ($\gtrsim 10^{17}$ G).

Figure 5.3 shows frequencies of CME modes corresponding to $n = 0$ plotted as a func-

Table 5.2: Radius and crust thickness for all three interactions at $B* = 0$ and $B* = 10^4$ [191]

	$B = 0$		$B_* = 10^4$	
Set	R(km)	△R/R	R(km)	△R/R
SLy4	13.972	0.096	13.987	0.100
SkM	13.875	0.086	13.892	0.088
Sk272	13.910	0.089	13.927	0.092

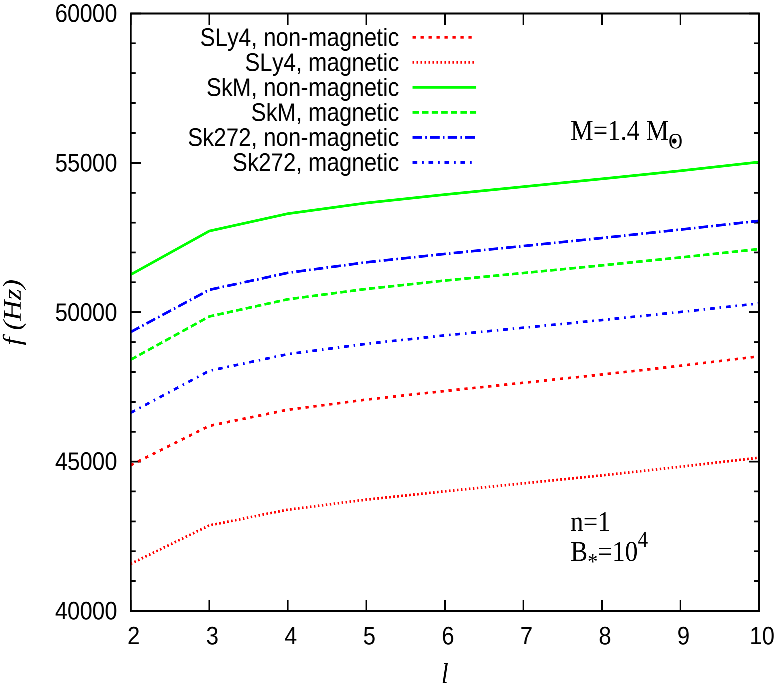

Figure 5.4: Frequencies of first overtones ($n = 1$) of CME modes are shown as a function of ℓ values with and without magnetic crusts of a 1.4 $M_\odot$ neutron star based on the SLy4, SkM and Sk272 nucleon-nucleon interactions for $B_* = 10^4$. [191]

tion of ℓ values for a 1.4 $M_\odot$ neutron star, magnetic field $B_* = 10^4$ and all three nucleon-nucleon interactions. Furthermore, we calculate frequencies using the non-magnetic as well as magnetic crusts. In all cases frequency increases with higher ℓ values. For higher values of ℓ, frequencies with magnetic crusts are found to be slightly smaller than those of non-magnetic crusts, i.e. when the effect of magnetic field on the crustal composition is neglected. This is true for all three nucleon-nucleon interactions used in this calculation. The small decrease in frequencies in case of magnetized crusts is due to increase of radius (R) of the star for $B_* = 10^4$ as is evident from Table 5.2 because fundamental frequencies are inversely proportional to R.

We continue our investigation on frequencies of first overtones ($n = 1$) of CME modes

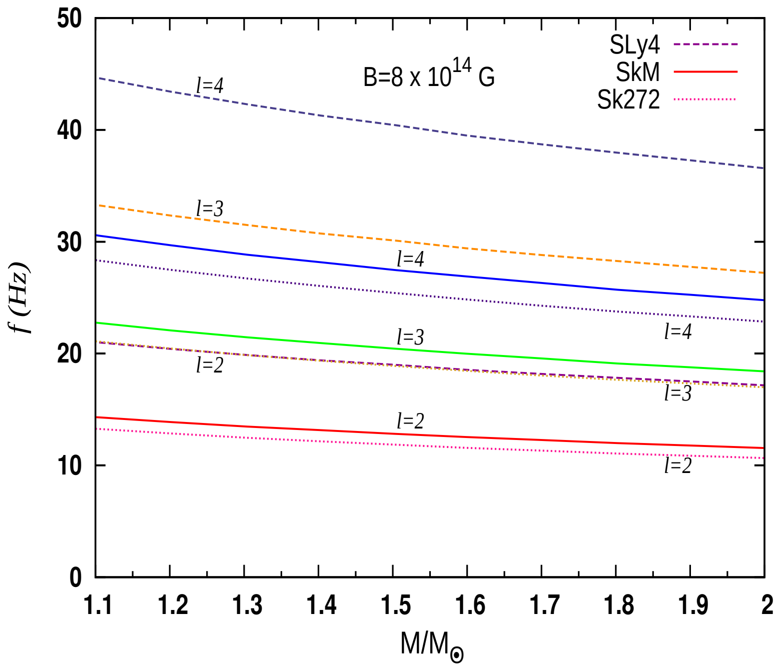

Figure 5.5: Frequencies of CME modes corresponding to $n = 0$ and $\ell = 2, 3, 4$ are plotted as a function of neutron star mass for a magnetic field $B = 8 \times 10^{14}$ G using magnetized crusts based on the SLy4, SkM and Sk272 nucleon-nucleon interactions. [191]

in the presence of magnetic fields. Frequencies of first overtones are shown as a function of ℓ values for a neutron star of 1.4 $M_\odot$, magnetic field $B_* = 10^4$ and all nucleon-nucleon interactions of Table 5.1 in Fig. 5.4. It is observed that the frequencies obtained with magnetized crusts are significantly suppressed compared with those of non-magnetized crusts for each nucleon-nucleon interaction and for all values of ℓ. This is understood if we remember the fact that the radius of a star is sensitive to the crustal EoS. Since strong magnetic fields ($\gtrsim 10^{17}$G) change the composition as well as EoS of the crust, the stellar radius as well as crustal thickness also get affected. In Table 5.2, we have shown the radius (R) and the ratio of the crust thickness (△R) to the radius of a neutron star for $B* = 0$ and $B_* = 10^4$, for all three nuclear interactions. From the table we see that the value of

$\triangle$R/R is larger for $B* = 10^4$ than for $B = 0$. It was noted that the ratio of the crust thickness to the radius of a neutron star was inversely proportional to the frequencies of overtones [156]. Hence, it explains why overtone frequencies are smaller for magnetized crusts with $B* = 10^4$, even though the shear moduli are little larger for this case than that of $B_* = 0$. The effects of nucleon-nucleon interactions are evident from the figure where the results of the SkM lie at the top and those of the SLy4 are at the bottom. This can also be understood from Table 5.2 if we note that the ratio ($\triangle$R/R) is the highest for the SLy4 interaction and lowest for the SkM interaction.

The dependence of frequencies of the fundamental mode and higher harmonics on neutron star masses is demonstrated in Fig. 5.5 for the SLy4, SkM and Sk272 nucleon-nucleon interactions. Here the frequencies corresponding to $n = 0$ and $\ell = 2, 3, 4$ are shown as a function of neutron star masses for a magnetic field $B = 8 \times 10^{14}$ G. For all cases, frequen-

Table 5.3: Frequencies of CME modes calculated using magnetized crusts based on the SLy4, SkM and Sk272 nucleon-nucleon interactions are compared with observed QPO frequencies of SGR 1806-20 [54–56, 153]. The magnetic field used in this calculation is $B = 8 \times 10^{14}$ G. Here f, n and ℓ represent frequency, radial node and angular node, respectively [191].

Observed frequency (Hz)	Calculated frequency (Hz)								
	SLy4 ($1.3M_\odot$)			SkM ($1.4M_\odot$)			Sk272 ($1.7M_\odot$)		
	f	n	ℓ	f	n	ℓ	f	n	ℓ
18	20.0	0	2	13.0	0	2	18.0	0	3
26	-	-	-	20.7	0	3	24.3	0	4
30	31.7	0	3	27.8	0	4	30.3	0	5
57	53.1	0	5	55.0	0	8	59.5	0	10
92.5	94.1	0	9	94.5	0	14	93.9	0	16
150	154.6	0	15	152.6	0	23	150.0	0	26
626	627.9	1	16	626.9	1	27	625.9	1	34
1838	1834.5	4	2	1836.3	4	2	1841.9	4	2

Table 5.4: Same as Table 5.3 but for SGR 1900+14 [151]. The magnetic field used in this calculation is $B = 4 \times 10^{14}$ G [191].

Observed frequency(Hz)	Calculated frequency (Hz) SLy4 $(1.7M_\odot)$			SkM $(1.2M_\odot)$			Sk272 $(1.2M_\odot)$		
	f	n	ℓ	f	n	ℓ	f	n	ℓ
28	28.4	0	3	28.3	0	4	26.6	0	4
54	56.7	0	6	55.8	0	8	52.5	0	8
84	84.2	0	9	82.7	0	12	83.8	0	13
155	156.4	0	17	155.2	0	23	157.1	0	25

cies of CME modes decrease with increasing mass, whereas higher ℓ values lead to higher frequencies. It is observed from Fig. 5.5 that frequencies corresponding to (non)magnetic crusts based on the SLy4 nucleon-nucleon interaction are much higher than those of other two nucleon-nucleon interactions. When the calculated frequencies are compared with the frequencies of observed QPOs, the latter might put a strong constraint on the EoS if masses of neutron stars are known accurately.

Next, we compare the calculated frequencies of CME modes with frequencies of observed QPOs. These comparisons are shown in Tables 5.3 and 5.4. Here we have also included QPO of 57 Hz found recently by Huppenkothen *et al.* [153] in the short bursts of SGR 1806-20. For SGR 1806-20, our results in Table 5.3 are obtained using the magnetized crusts of 1.3, 1.4 and 1.7 $M_\odot$ neutron stars based on the SLy4, SkM and Sk272 nucleon-nucleon interactions, respectively, and magnetic field $B = 8 \times 10^{14}$ G. It is noted that calculated frequencies below 93 Hz for each nucleon-nucleon interaction can not explain the observed frequencies whereas our results above 93 Hz are in very good agreement with observed QPO frequencies [54–56]. Similarly for SGR 1900+14, we calculate CME mode frequencies using magnetized crusts of 1.7, 1.2 and 1.2 $M_\odot$ neutron stars corresponding to the SLy4, SkM and Sk272 nucleon-nucleon interactions and $B = 4 \times 10^{14}$ G. These

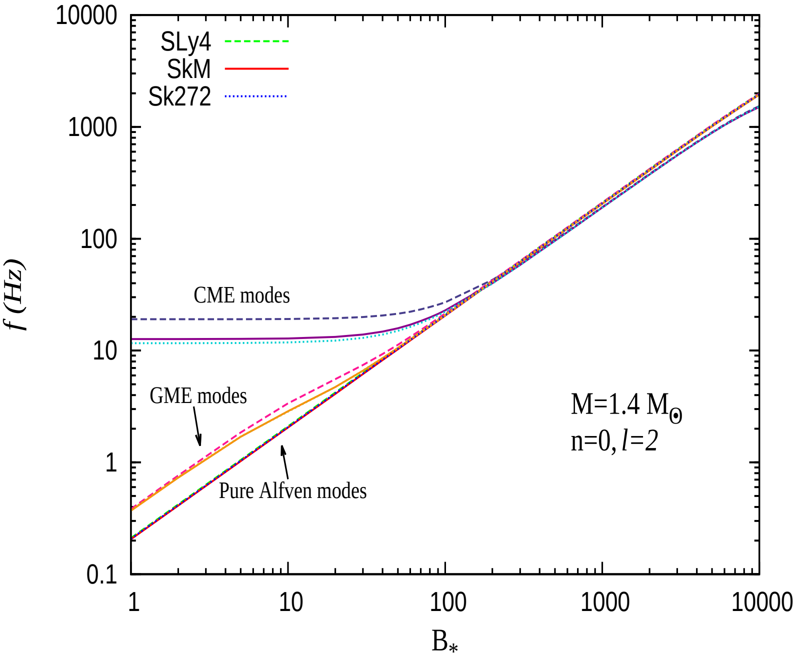

Figure 5.6: Comparison of the GME frequencies with pure Alfvén frequencies as well as CME frequencies is shown as a function of magnetic field using the magnetized crusts based on the SLy4, SkM and Sk272 nucleon-nucleon interactions. [191]

results are shown in Table 5.4. Our calculated frequencies for all three nucleon-nucleon interactions are in agreement with the observed QPO frequencies of SGR 1900+14 [151].

5.3.2 GME modes

First we calculate pure Alfvén modes of a neutron star of mass $1.4M_\odot$, by ignoring the presence of the solid crust. In Fig. 5.6, we show the pure Alfvén mode corresponding to $n = 0$; $\ell = 2$ as a function of magnetic field (B_*). Here, n stands for the number of radial nodes in the eigenfunctions, in the liquid core. We see that the frequency of this mode increases linearly with magnetic field and become equal to those of the CME modes above $B_* = 100$. Next, we calculate corresponding GME mode frequencies for various

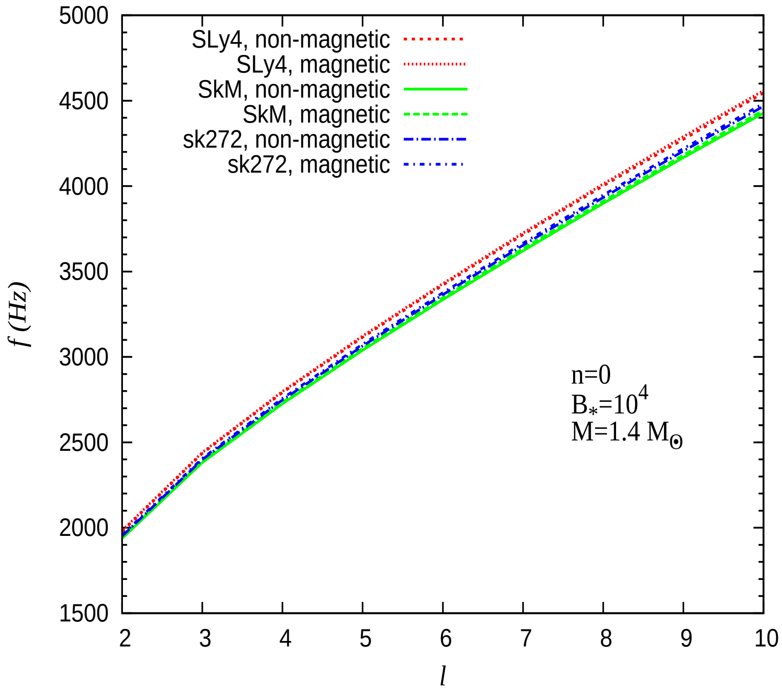

Figure 5.7: GME mode frequencies for $n = 0$ are shown as a function of ℓ values with and without magnetic crusts of a neutron star of mass $1.4M_{\odot}$ based on the SLy4, SkM and Sk272 nucleon-nucleon interactions for $B_* = 10^4$ [191].

magnetic fields, taking magnetic crusts into consideration. Magnetized crusts used here are calculated with the SLy4, SkM and Sk272 nucleon-nucleon interactions.

It is observed that at low magnetic fields global mode frequencies have higher values as compared to those of pure Alfvén modes. The GME modes are found to be confined to the core for low magnetic field strengths. This scenario is similar to the reflection of GME modes at the crust-core interface as manifested in the state-of-the-art model of Gabler et al. [168]. Consequently, this leads to higher frequencies for GME modes compared with those of pure Alfvén modes. But at higher magnetic fields, GME mode frequencies merge with that of pure Alfvén modes. This happens because at higher values of fields ($B \geq 4.14 \times 10^{15}$) shear modulus becomes negligible as compared to the magnetic effect

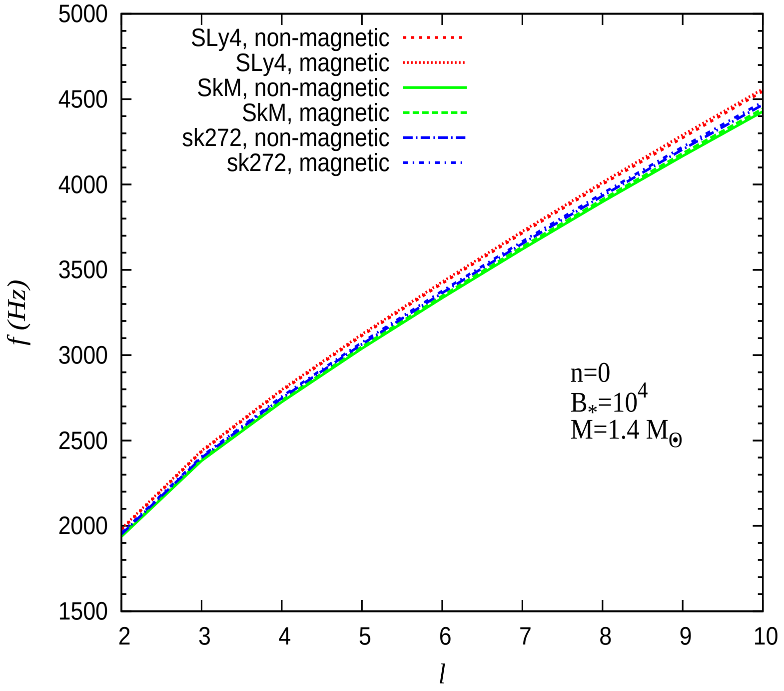

Figure 5.8: GME mode frequencies for $n = 1$ are plotted as a function of ℓ values with and without magnetic crusts of a neutron star of mass $1.4M_\odot$ based on the SLy4, SkM and Sk272 nucleon-nucleon interactions for $B_* = 10^4$ [191].

($\mu \ll B^2$); in other words Alfvén velocity ($B/\sqrt{4\pi\rho}$) becomes much larger compared to the shear velocity ($\sqrt{\mu/\rho}$). We also show the frequencies of CME modes for comparison. It is also evident from Fig. 5.6 that the effects of crusts on frequencies disappear at very high magnetic fields $B_* > 100$ and oscillations become magnetic oscillations [197].

To see the effects of magnetic crusts on GME modes we calculate these modes with and without magnetic crusts based on the SLy4, SkM and Sk272 nucleon-nucleon interactions. Figures 5.7 and 5.8 show results for modes with $n = 0$ and $n = 1$, respectively as a function of ℓ for a neutron star of mass $1.4M_\odot$ and magnetic field $B_* = 10^4$. We can see there is no significant change in frequencies if the crust is considered to be magnetic. For fundamental modes in Fig. 5.7, there is no appreciable change in frequencies with and without magnetic

Table 5.5: GME mode frequencies obtained using the magnetized crusts based on the SLy4, SkM and Sk272 nucleon-nucleon interactions are compared with observed frequencies in SGR 1806-20. The magnetic field used in this calculation is $B = 3.1 \times 10^{15}$ G [191].

Observed frequency(Hz)	Calculated frequency (Hz)								
	SLy4			SkM			Sk272		
	$(1.5M_\odot)$			$(1.4M_\odot)$			$(1.4M_\odot)$		
	f	n	ℓ	f	n	ℓ	f	n	ℓ
18	17.8	0	3	18.2	0	3	18.1	0	3
26	26.1	0	6	26.1	0	6	25.8	0	6
30	30.7	0	8	30.7	0	8	30.4	0	8
57	57.8	1	7	57.1	1	6	56.7	1	6
92.5	93.0	4	2	91.6	2	8	94.5	2	9
150	150.0	6	4	150.9	4	10	150.3	6	3
626	624.3	30	6	626.4	28	6	628.6	27	9
1838	1837.3	96	5	1836.4	97	2	1835.8	87	10

crusts. Unlike Fig. 5.3 for CME modes, GME modes are insensitive to the small change in R. In case of first overtones in Fig. 5.8, we do not find any appreciable effects of crusts on frequencies because the magnetic field $B_* = 10^4$ is so high that oscillations become magnetic oscillations.

We also attempt to match the observed frequencies with those of calculated GME

Table 5.6: Same as Table 5.5 but for the SGR 1900+14. The magnetic field adopted here is $B = 1.34 \times 10^{15}$ G [191].

Observed frequency(Hz)	Calculated frequency (Hz)								
	SLy4			SkM			Sk272		
	$(1.4M_\odot)$			$(1.3M_\odot)$			$(1.3M_\odot)$		
	f	n	ℓ	f	n	ℓ	f	n	ℓ
28	28.0	1	6	28.4	1	6	28.0	1	5
54	54.7	3	8	54.7	3	7	53.6	2	11
84	84.7	7	5	84.1	6	6	84.4	5	8
155	155.6	16	3	154.7	14	4	154.5	11	9

modes. The results are shown in Tables 5.5 and 5.6. For SGR1806-20, we compute frequencies using the magnetized crusts of 1.5, 1.4 and 1.4 $M_\odot$ neutron stars based on the SLy4, SkM and Sk272 nucleon-nucleon interactions, respectively, and magnetic field $B = 3.1 \times 10^{15}$ G. These results are given by Table 5.5. We find that the calculated frequencies agree well with the lower and higher frequencies of observed QPOs. However, it is noted that large values of n are needed to fit higher frequencies. This feature for higher frequencies was also obtained by Sotani et al. [181]. On the other hand, we exploit magnetized crusts of 1.4, 1.3 and 1.3 M$_\odot$ neutron stars corresponding to the SLy4, SkM and Sk272 nucleon-nucleon interactions and magnetic field $B = 1.34 \times 10^{15}$ G for SGR 1900+14. The Table 5.6 demonstrates that the calculated frequencies are in good agreement with the observed frequencies of SGR 1900+14. We do not find any appreciable effects of nucleon-nucleon interactions in either table.

5.4 Summary and Conclusions

We have estimated frequencies of global magneto-elastic modes as well as magneto-elastic modes confined to the crust only of magnetars assuming a dipole magnetic field configuration. Frequencies are computed using our models of magnetized crusts based on the SLy4, SkM and Sk272 nucleon-nucleon interactions. Though the formalism used in Sotani et al. [181] and in this calculation are same, magnetized crusts are employed for the first time here. The shear modulus of magnetized crusts is found to be enhanced in strong magnetic fields $\sim 4.414 \times 10^{17}$ G because electrons populate the zeroth Landau level. It is observed that frequencies of the fundamental ($n = 0$, $\ell = 2$) CME mode are not sensitive to this enhancement in the shear modulus in strong magnetic fields. On the other hand, frequencies of first overtones ($n = 1$) of CME modes in the presence of strongly quantizing magnetic fields are distinctly different from those of the field free case. It is shown that that this is related to the the ratio of the crust thickness to the radius of a magnetar. We have found that at $B_* = 10^4$, the $\triangle R/R$ is increased by $2 - 4\%$, which causes frequencies of overtones to decrease by $5 - 7\%$, for the models we used here. For GME modes, the effects of crusts disappear above a critical field ($B > 4 \times 10^{15}$ G) and oscillations become magnetic oscillations. We have compared frequencies of CME and GME modes calculated using different stellar models, magnetic field strengths and magnetized crusts based on three nucleon-nucleon interactions with frequencies of observed QPOs and conclude that the agreement is reasonable for SGR 1900+14 in both cases. However, the calculated frequencies of CME modes do not match with lower frequencies of SGR 1806-20, but can explain higher frequencies well. In the case of GME modes, we find the opposite trends in fitting the frequencies of SGR 1806-20. Finally new results that we have obtained would be reproduced even in a sophisticated MHD calculation.

BIBLIOGRAPHY

[1] W. Baade and F. Zwicky, Proc. Nat. Acad. Sci., **20**, 254, (1934).

[2] S. A. Colgate , M. H. Johnson, Phys. Rev. Lett. **5**, 235 (1960).

[3] S. A. Colgate , R. H. White, Astrophys. J. **143**, 626 (1966).

[4] W. D. Arnett, Can. J. Phys. **44**, 2553 (1966).

[5] J. R. Wilson, Astrophys. J. **163** 209 (1971).

[6] H. A. Bethe, Ann. Rev. Nucl. Part. Sci. **38**, 1 (1988)

[7] H. A. Bethe, Rev. Mod. Phys. **62**, 801 (1990)

[8] A. Burrows, J. Hayes, & B.A. Fryxell, Astrophys. J. **450**, 830 (1995)

[9] H.-T. Janka, K. Langanke, A. Marek, G. Martínez-Pinedo, & B. Müller, Phys. Rep. **442**, 38 (2007)

[10] H.-T Janka, Annu. Rev. Nucl. Part. Sci. **62**, 407 (2012)

[11] K. Kotake, T. Takiwaki, Y. Suwa, W. I. Nakano, S. Kawagoe, Y. Masada and S. i. Fujimoto, Adv. Astron. **2012**, 428757 (2012)

[12] K. Kotake, K. Sumiyoshi, S. Yamada, T. Takiwaki, T. Kuroda, Y. Suwa and H. Nagakura, PTEP **2012**, 01A301 (2012)

[13] A. Burrows, Rev. Mod. Phys. **85**, 245 (2013)

[14] S. E. Woosley, & T. A. Weaver, Ann. Rev. Astron. Astrophys. **24**, 205 (1986)

[15] S. E. Woosley, & T. A. Weaver, Astrophys. J. Suppl. Ser. **101**, 181 (1995)

[16] S. E. Woosley, A. Heger, & T. A. Weaver, Rev. Mod. Phys., **75**, 1015, (2002)

[17] H. Bethe, J. R. Wilson, Astrophys. J. **295**, 14 (1985)

[18] A. Burrows, L. Dessart, E. Livne, C.D. Ott, & J.W. Murphy, Astrophys. J. **664**, 416 (2007)

[19] T. Takiwaki, & K. Kotake, Astrophys. J. **743**, 30 (2011)

[20] A. Burrows, E. Livne, L. Dessart, C.D. Ott, & J.W. Murphy, Astrophys. J. **640**, 878 (2006)

[21] A. Burrows, E. Livne, L. Dessart, C.D. Ott, & J.W. Murphy, Astrophys. J. **655**, 416 (2007)

[22] S. Hannestad and G. Raffelt, Astrophys. J. **507**, 339 (1998)

[23] T.A. Thompson, A. Burrows and J.E. Horvath, Phys. Rev. C, **62**, 035802 (2000)

[24] R. Buras, H. -T. Janka, M. Th. Keil, G. Raffelt and M. Rampp, Astrophys. J. **587**, 320 (2003)

[25] M. Th. Keil, G. Raffelt and H. -T. Janka, Astrophys. J. **590**, 971 (2003)

[26] M. Liebendörfer, A. Mezzacappa, F. K. Thielemann, O. E. Messer, W. R. Hix, & S. W. Bruenn, Phys. Rev. D, **63**, 103004 (2001)

[27] F. S. Kitaura, H. -T. Janka, & W. Hillebrandt, Astron. & Astrophys. **450**, 345 (2006)

[28] H. -T. Janka, and E. Mueller, Astron. Astrophys. **306**, 167 (1996)

[29] J. M. Blondin, A. Mezzacappa, and C. DeMarino, Astrophys. J. **584**, 971 (2003)

[30] T. Foglizzo, L. Scheck, and H. -T. Janka, Astrophys. J. **652**, 1436 (2006)

[31] A. Marek, and H. -T. Janka, Astrophys. J. **694**, 664 (2009)

[32] C. D. Ott, A. Burrows, L. Dessart, & E. Livne, Astrophys. J. **685**, 1069 (2008)

[33] B. Müller, H. -T. Janka, and A. Marek, Astrophys. J. **756**, 84 (2012)

[34] J. M. Blondin, & A. Mezzacappa, Nature, **445**, 58 (2007)

[35] T. Takiwaki, K. Kotake, and Y. Suwa, Astrophys. J. **749**, 98 (2012)

[36] J. C. Dolence, A. Burrows, J. W. Murphy, & J. Nordhaus, Astrophys. J. **765**, 110 (2013)

[37] W. Hillebrandt, & R. G. Wolff, in Nucleosynthesis: Challenges and New Developments, ed. W. D. Arnett, & J. W. Truran (Chicago: University of Chicago Press), 131, (1985)

[38] J. M. Lattimer, & F. D. Swesty, Nucl. Phys. A, **535**, 331 (1991)

[39] H. Shen, H. Toki, K. Oyamatsu, and K. Sumiyoshi, Nucl. Phys. A **637**, 435 (1998)

[40] M. Hempel & J. Schaffner-Bielich, Nucl. Phys. A, **837**, 210 (2010)

[41] C. Ishizuka, A. Ohnishi, K. Tsubakihara, K. Sumiyoshi, & S Yamada, J. Phys. G, **35**, 085201 (2008)

[42] H. Shen, H. Toki, K. Oyamatsu, and K. Sumiyoshi, Astrophys. J. Suppl. Ser. **197**, 20 (2011)

[43] M. Oertel, A. F. Fantina, & J. Novak, Phys. Rev. C, **85**, 055806 (2012)

[44] S. Banik, M. Hempel, & D. Bandyopadhyay, Astrophys. J. Suppl. Ser., **214**, 22 (2014)

[45] I. Sagert, T. Fischer, M. Hempel et al. Phys. Rev. Lett., **102**, 081101 (2009)

[46] G. E. Brown and H. A. Bethe, Astrophys. J. **423**, 659 (1994)

[47] R. A. Hulse and J. H. Taylor, Astrophys. J., **195**, L51 (1975).

[48] D.J. Champion, et al., Science, **320**, 1309 (2008).

[49] P.B. Demorest, T. Pennucci, S.M. Ransom, M.S.E. Roberts, J.W.T. Hessels, Nature, **467**, 1081 (2010).

[50] J. Antoniadis, P. C. C. Freire, N. Wex, T. M. Tauris, R. S. Lynch, et al., Science, **340**, 448 (2013).

[51] A. Watts, C.M. Espinoza, R. Xu, N. Andersson, J. Antoniadis, D. Antonopoulou, S. Buchner, S. Datta, P. Demorest, P. Freire et al., Advancing Astrophysics with the Square Kilometre Array (AASKA14) 43 (2015) (arXiv:1501.00042)

[52] R.C. Duncan and C. Thompson, Astrophys. J. **392**, L9 (1992).

[53] R. Turolla, S. Zane and A. L. Watts Rep. Prog. Phys. **78** 116901 (2015)

[54] G.L. Israel et al, Astrophys. J. **628**, L53 (2005).

[55] T.E. Strohmayer and A.L. Watts, Astrophys. J. **653**, 593 (2006).

[56] A.L. Watts and T.E. Strohmayer, Astrophys. J. **637**, L117 (2006).

[57] C. F. von Weizsäcker, Z. Phys. **96**, 431 (1935).

[58] T. H. R. Skyrme, Philos. Mag. **1**, 1043 (1956).

[59] D. Vautherin and D. M. Brink, Phys. Rev. C **5**, 626 (1972).

[60] J. D. Walecka, Ann. Phys. **83**, 491 (1974).

[61] D. Page, S. Reddy, Annu. Rev. Nucl. Part. Sci., **56**, 327 (2006)

[62] M. Dutra et. al, Phys. Rev. C **90**, 055203 (2014)

[63] H. Heiselberg, V. R. Pandharipande, Annu. Rev. Nucl. Part. Sci. **50**, 481 (2000)

[64] A Akmal , V. R. Pandharipande, D. G. Ravenhall, Phys. Rev. C **58**,1804 (1998)

[65] M. Baldo, Nuclear Methods and the Nuclear Equation of State, International Review of Nuclear Physics, Vol. 8 (World Scientific, Singapore, 1999).

[66] G. Taranto, M. Baldo, and G. F. Burgio, Phys. Rev. C **87**, 045803 (2013)

[67] R. Machleidt, Adv. Nucl. Phys. 19, 189 (1989).

[68] B. D. Serot, Rep. Prog. Phys. **55**, 1855 (1992)

[69] B. D. Serot and J. D. Walecka, Ad. Nucl. Phys. **16**, 1 (1986);
J. D. Walecka, Theoretical Nuclear and Subnuclear Physics (Oxford , Oxford University).

[70] J. Schaffner and I.N. Mishustin, Phys. Rev. C **53** 1416 (1996).

[71] S. Banik and D. Bandyopadhyay, Phys. Rev. C **66** 065801 (2002).

[72] S. Typel, Phys. Rev. C **71** 064301 (2005).

[73] S. Typel, G. Röpke, T. Klähn, D. Blaschke and H.H. Wolter, Phys. Rev. C **81** 015803, (2010).

[74] J. M. Lattimer and Y. Lim Astrophys. J., **771**, 51 (2013).

[75] T. Fischer, M. Hempel, I. Sagert, Y. Suwa and J. Schaffner-Bielich, Eur. Phys. J. A **50**, 46 (2014).

[76] C. Fuchs, H. Lenske and H.H. Wolter, Phys. Rev. C **52**, 3043 (1995).

[77] H. Lenske and C. Fuchs, Phys. Lett. B **345**, 355 (1995).

[78] M. Buballa, V. Dexheimer, A. Drago et al., J. Phys. G, **41**, 123001 (2014)

[79] D. Lonardoni, A. Lovato, S. Gandolfi, & F. Pederiva, Phys. Rev. Lett., **114**, 092301 (2015)

[80] J. Schaffner, C.B. Dover, A. Gal, D.J. Millener, C. Greiner and H. Stöcker, Ann. Phys. (N.Y.) **235**, 35 (1994)

[81] J.A. Pons, S. Reddy, P.J. Ellis, M.Prakash, and J.M. Lattimer, Phys. Rev. C **62** 035803 (2000).

[82] S. Banik and D. Bandyopadhyay, Phys. Rev. D **82**, 123010 (2010).

[83] S. Typel and H. H. Wolter, Nucl. Phys. A **656**, 331 (1999).

[84] T. Nikšić, D. Vretenar, P. Finelli, and P. Ring, Phys. Rev. C **66**, 024306 (2002).

[85] G. A. Lalazissis, T. Nikšić, D. Vretenar, and P. Ring, Phys. Rev. C **71**, 024312 (2005).

[86] G. Colucci and A. Sedrakian, Phys. Rev. C **87**, 055806 (2013).

[87] R.E. Chrien and C.B. Dover, Annu. Rev. Nucl. Part. Sci. **39**, 113 (1989)

[88] C.B. Dover and A. Gal, Prog. Part. Nucl. Phys. **12** 171 (1984).

[89] T. Fukuda et al., Phys. Rev. C **58**, 1306 (1998).

[90] P. Khaustov et al., Phys. Rev. C61 (2000) 054603.

[91] S. Weissenborn, D. Chatterjee, and J. Schaffner-Bielich, Nucl. Phys. A **881**, 62 (2012) .

[92] S. Weissenborn, D. Chatterjee, and J. Schaffner-Bielich, Phys. Rev. C **85**, 065802 (2012).

[93] R. Lastowiecki, H. Blaschke, H. Grigorian, and S. Typel, 2012, Acta Phys. Polon. Suppl., **5**, 535 (2012).

[94] L. L. Lopes, & D. P. Menezes, Phys. Rev. C, **89**, 025805 (2013)

[95] M. E. Gusakov, P. Haensel, & E. M. Kantor, Mon. Not. R. Astron. Soc., **439**, 318 (2014)

[96] E. N. E. van Dalen, G. Colucci, & A. Sedrakian, Phys. Lett. B, **734**, 383 (2014)

[97] P. Char, & S. Banik, Phys. Rev. C **90**, 015801 (2014)

[98] K. Nakazato, K. Sumiyoshi, & S. Yamada, , Phys. Rev. D, **77**, 103006 (2008)

[99] K. Nakazato, S. Furusawa, K. Sumiyoshi, A. Ohnishi, S. Yamada, & H. Suzuki, Astrophys. J., **745**, 197 (2012)

[100] K. Sumiyoshi, C. Ishizuka, A. Ohnishi, S. Yamada, and H. Suzuki, Astrophys. J. Lett. **690**, L43 (2009).

[101] S. Banik, Phys. Rev. C **89**, 035807 (2014).

[102] S. Typel, M. Oertel, T. Klähn, 2013, arXiv:1307.5715

[103] E. O’Connor, & C. D. Ott, Class. Quant. Grav., **27**, 114103 (2010)

[104] Y. Sugahara and H. Toki, Nucl. Phys. A **579**, 557 (1994)

[105] D. J. Millener, C. B. Dover, & A. Gal Phys. Rev. C, **38** , 2700 (1988)

[106] J. Mares, E. Friedman, A. Gal, & B. Jennings, Nucl. Phys. A, **594**, 311 (1995)

[107] J. Schaffner, H. Stöcker,& C. Greiner, Phys. Rev. C, **46**, 322 (1992)

[108] P. Char, S. Banik, D. Bandyopadhyay, Astrophys. J., **809**, 116 (2015)

[109] E. Gourgoulhon, Astron. Astrophys. **252**, 651 (1991)

[110] Scott C. Noble 2003 PhD Thesis University of Britsh Columbia (arXiv:gr-qc/0310116)

[111] F. Banyuls, J. A. Font, J. M. Ibáñez, J. M. Martí, and J. A. Miralles, Astrophys. J. **476**, 221 (1997)

[112] J. V. Romero, J. M. Ibanez, J. M. Marti, and J. A. Miralles, Astrophys. J. **462**, 839 (1996)

[113] M. Liebendörfer, Astrophys. J., **633**, 1042 (2005)

[114] S. Rosswog, & M. Liebendörfer, Mon. Not. R. Astron. Soc., **342**, 673 (2003)

[115] M. Ruffert, H. -T Janka, & G. Schäfer, Astron. Astrophys., **311**, 532 (1996)

[116] E. O’Connor, & C. D. Ott, Astrophys. J., **730**, 70 (2011)

[117] H. -T. Janka, Astron. Astrophys., **368**, 527 (2001)

[118] T. Fischer, S. C. Whitehouse, A. Mezzacappa, F.-K. Thielemann, M. & Liebendörfer, Astron. Astrophys., **499**, 1 (2009)

[119] K. Sumiyoshi, S. Yamada, & H. Suzuki, Astrophys. J., **667**, 382 (2007)

[120] S. E. Woosley, & A. Heger, Phys. Rep., **442**, 269 (2007)

[121] B. Peres, M. Oertel, J. Novak, Phys. Rev. D **87**, 043006 (2013).

[122] M. Prakash, J. R. Cooke, & J. M. Lattimer, Phys. Rev. D, **52**, 661 (1995)

[123] S. Banik and D. Bandyopadhyay, Phys. Rev. C **63**, 035802 (2001).

[124] W. Keil, & H. -T Janka, Astrophys. J., **296**, 145 (1995)

[125] T. W. Baumgarte, H. -T. Janka, W. Keil, S. L. Shapiro, & S. A. Teukolsky, Astrophys. J., **468**, 823 (1996)

[126] N.K. Glendenning, Compact stars, (Springer, New York, 1997).

[127] S. Banik and D. Bandyopadhyay, Phys. Rev. C **64**, 055805 (2001).

[128] A.R. Taurines, C.A.Z. Vasconcellos, M. Malheiro, M. Chiapparini, Phys. Rev. C **C63** 065801 (2001).

[129] R. O. Gomes, V. Dexheimer, S. Schramm, and C. A. Z. Vasconcellos, Astrophys. J. **808**, 8 (2015)

[130] D.B. Kaplan and A.E. Nelson, Phys. Lett. B **175**, 57 (1986); A.E. Nelson and D.B. Kaplan, *ibid.* **192**, 193 (1987).

[131] M. Prakash, I. Bombaci, M. Prakash, Paul J. Ellis, J. M. Lattimer and R. Knorren, Phys. Rep. **280**, 1 (1997).

[132] N. Gupta, P. Arumugam, Phys. Rev. C **87** (2013) 4, 045802.

[133] S. Pal, D. Bandyopadhyay and W. Greiner, Nucl. Phys. A **674**, 553 (2000).

[134] N.K. Glendenning and J. Schaffner-Bielich, Phys. Rev. C **60**, 025803 (1999).

[135] G.Q. Li, C.-H. Lee and G.E. Brown, Phys. Rev. Lett. **79**, 5214 (1997); Nucl. Phys. **A625**, 372 (1997).

[136] S. Pal, C.M. Ko, Z. Lin and B. Zhang, Phy. Rev. C **62**, 061903(R) (2000).

[137] L. Tolos, A. Ramos, E. Oset, Phys. Rev. C **74**, 015203 (2006)

[138] V. K. Magas, J. Yamagata-Sekihara, S. Hirenzaki, E. Oset, A. Ramos, Few-Body Syst. **50**, 343 (2011).

[139] G. Baym, C.J. Pethick and P. Sutherland, Astrophys. J. **170**, 299 (1971).

[140] C.M. Keil, F. Hofmann and H. Lenske, Phys. Rev. C **61**, 064309 (2001).

[141] S.A. Olaunsen and V.M. Kaspi, Astrophys. J. Suppl. Ser., **212**, 6 (2014).

[142] K. Hurley et al., Nature **397**, L41 (1999).

[143] C. Barat et al., Astron. Astrophys. **126**, 400 (1983).

[144] A.L. Watts, in Neutron Star Crust, edited by Bertulani C. A., and Piekarewicz J., (Nova Science, NY, 2012); arXiv:1111.0514.

[145] A.L. Watts and T.E. Strohmayer, Adv. Sp. Res. **40**, 1446 (2007).

[146] D. M. Palmer, S. Barthelmy, N. Gehrels et al. Nature, **434**, L1107 (2005)

[147] R.C. Duncan, Astrophys. J. **498**, L45 (1998).

[148] C. Kouveliotou et al., Nature **393**, L235 (1998).

[149] D. Chatterjee, T. Elghozi, J. Novak and M. Oertel, Mon. Not. R. Astron. Soc. **447**, 3785 (2015).

[150] S. Chakrabarty, D. Bandyopadhyay and S. Pal, Phys. Rev. Lett. **78**, 2898 (1997).

[151] T.E. Strohmayer and A.L. Watts, Astrophys. J. **632**, L111 (2005).

[152] D. Huppenkothen et al, Astrophys. J. **787**, 128 (2014).

[153] D. Huppenkothen, L. M. Heil, A.L. Watts and E. Göğös, Astrophys. J. **795**, 114 (2014).

[154] D. Huppenkothen, A.L. Watts and Y. Levin, Astrophys. J. **793**, 129 (2014)

[155] A.L. Piro, Astrophys. J. **634**, L153 (2005).

[156] H. Sotani, K.D. Kokkotas and N. Stergioulas, Mon. Not. R. Astron. Soc. **375**, 261 (2007).

[157] L. Samuelsson and N. Andersson, Mon. Not. R. Astron. Soc. **374**, 256 (2007).

[158] H. Sotani, K.D. Kokkotas and N. Stergioulas, Mon. Not. R. Astron. Soc. **385**, L5 (2008).

[159] H. Sotani, A. Colaiuda and K.D. Kokkotas, Mon. Not. R. Astron. Soc. **385**, 2161 (2008).

[160] A.W. Steiner and A.L. Watts, Phys. Rev. Lett. **103**, 181101 (2009).

[161] Y. Levin, Mon. Not. R. Astron. Soc. **377**, 159 (2007).

[162] A. Colaiuda, H. Beyer and K.D. Kokkotas, Mon. Not. R. Astron. Soc. **396**, 1441 (2009).

[163] P. Cerdá-Durán, N. Stergioulas and J.A. Font., Mon. Not. R. Astron. Soc. **397**, 1607 (2009)

[164] Y. Levin, Mon. Not. R. Astron. Soc. **368**, L35 (2006)

[165] M. van Hoven and Y. Levin, Mon. Not. R. Astron. Soc. **410**, 1036 (2011).

[166] M. van Hoven and Y. Levin, Mon. Not. R. Astron. Soc. **420**, 3035 (2012).

[167] A. Colaiuda and K.D. Kokkotas, Mon. Not. R. Astron. Soc. **414**, 3014 (2011).

[168] M. Gabler, P. Cerdá-Durán, N. Stergioulas, J.A. Font and E. Müller, Mon. Not. R. Astron. Soc. **421**, 2054 (2012).

[169] M. Gabler, P. Cerdá-Durán, J.A. Font, E. Müller and N. Stergioulas, Mon. Not. R. Astron. Soc. **430**, 1811 (2013).

[170] H. Sotani, Mon. Not. R. Astron. Soc. **417**, L70 (2011).

[171] N. Andersson, K Glampedakis and L. Samuelsson, Mon. Not. R. Astron. Soc. **396**, 894 (2009).

[172] A. Passamonti and S. K. Lander, Mon. Not. R. Astron. Soc. **438**, 156 (2013).

[173] M. Gabler, P. Cerdá-Durán, N. Stergioulas, J.A. Font and E. Müller, PRL **111**, 211102 (2013).

[174] M. Sinha and A. Sedrakian, PRC **91**, 035805 (2015).

[175] R. Nandi and D. Bandyopadhyay, J. Phys. Conf. Ser. **312**, 042016 (2011).

[176] R. Nandi, D. Bandyopadhyay, I.N. Mishustin and W. Greiner, Astrophys. J. **736**, 156 (2011).

[177] B.W. Carrol et al., Astrophys. J. **305**, 767 (1986).

[178] P.N. McDermott, H.M. van Horn, C. J. Hansen, Astrophys. J. **325**, 725 (1988).

[179] B.L. Schumaker and K.S. Thorne, Mon. Not. R. Astron. Soc. **203**, 457 (1983).

[180] N. Messios, D.B. Papadopolous, N. Stergioulas, Mon. Not. R. Astron. Soc. **328**, 1161 (2001).

[181] H. Sotani, K. D. Kokkotas, N. Stergioulas, and M. Vavoulidis, arXiv:astro-ph/0611666

[182] M. Bocquet, S. Bonazzola, E. Gourgoulhon and J. Novak, Astro. Astrophys. **301**, 757 (1995)

[183] P.N. McDermott,H.M. van Horn, J.F. Scholl, Astrophys. J. **268**, 837 (1983).

[184] S. Ogata and S. Ichimaru, Phys. Rev. A **42**, 4867 (1990).

[185] T. Strohmayer, H.M. van Horn, S. Ogata, H. Iyetomi and S. Ichimaru, Astrophys. J. **375**, 679 (1991).

[186] P. Haensel, in Lecture Notes in Physics: Physics of Neutron Star Interiors, edited by Blaschke D., Glendenning N.K. and Sedrakian A., **578**, 127 (Springer, Heidelberg, 2001).

[187] D. Lai and S. L. Shapiro, Astrophys. J. **383**, 745 (1991)

[188] P. Bonche, S. Levit and D. Vautherin, Nucl. Phys. **A427**, 278 (1984).

[189] P. Bonche, S. Levit and D. Vautherin, Nucl. Phys. **A436**, 265 (1985).

[190] T. Sil, J.N. De, S.K. Samaddar, X. Vinas, M. Centelles, B.K. Agrawal and S.K. Patra, Phys. Rev. C **66**, 045803 (2002).

[191] R. Nandi, P. Char, D. Chatterjee, and D. Bandyopadhyay Phys. Rev. C **94**, 025801 (2016)

[192] D. G. Ravenhall, C. J. Pethick and J. R. Wilson Phys. Rev. Lett. **50**, 2066 (1983)

[193] M. Hashimoto, H. Seki and M. Yamada, Prog. Theor. Phys. **71** 320 (1984)

[194] R. Nandi and S. Schramm, arXiv:nucl-th/1601.01842.

[195] M. Sinha and D. Bandyopadhyay, Phys. Rev. D **79**, 123001 (2009).

[196] N.K. Glendenning and S.A. Moszkowski, Phys. Rev. Lett. **67**, 2414 (1991).

[197] H. Sotani, Phys. Rev. D **92**, 104024 (2015).